Electrophysiological Modelling and Power-efficient Design of Temporal Interference-based Neural Stimulators

by

Joris Corstiaan de Koning

A thesis submitted to the Department of Microelectronics,
of the Faculty of Electrical Engineering, Mathematics and Computer Science at
Delft University of Technology
in partial fulfillment of the requirements for the degree of

Master of Science in Electrical Engineering

Thesis committee:

Prof.dr.ir. W.A. Serdijn, Supervisor
Dr.ir. C.J.M. Verhoeven
Ir. A.J.M. Montagne

August 2025

Contents

Summary

This thesis investigates the design challenges and underlying mechanisms of spatially selective vagus nerve stimulation using temporal interference stimulation (TIS). While TIS shows promise for non-invasive and spatially selective neuromodulation, a limited understanding of the mechanistic underpinnings of neural stimulation enabled by high-frequency interfering electric fields, and fundamentally larger power expenditure related to the generation of low frequency intermodulation products, limits its applicability to specific cases where the featured spatial selectivity is an absolute necessity.

The objective of this research is to develop an electrophysiological model to accurately represent experimental measurements of nonlinear neuron responses under influence of TIS, and to develop a system architecture and output stage design with power supply regulation for a power-efficient and spatially selective temporal interference-based vagus nerve stimulator.

The proposed model generates an output waveform by means of nonlinear approximation of electric field interference, up to a specific order of a Taylor expansion. The model is shown to accurately predict intermodulation products present in experimental data of TIS for various input frequencies. A way to define the relevance of waveform shape on the stimulation efficiency of temporal interference stimulation is also hypothesized, which shows that the efficiency of both sinusoidal (at even orders of the Taylor expansion) and square waveforms is dependent on input Taylor expansion order, approaching 10 % efficiency when the order of the expansion is high. Limitations of the model include the lack of experimental data to validate the model outputs for other waveforms besides sinusoidal ones, and simplified assumptions made in the determination of Taylor expansion coefficients, which may limit the applicability of a generalized version of the model.

The principles behind temporal interference-based stimulators and the effect of power supply regulation on power-efficiency are discussed, leading to a full system architecture for the power-efficient implementation of TIS-based stimulators. The presented indirect feedback output stage design, with power supply regulation, features over 3σ-accuracy to the required load current, and consistently outperforms conventional cascode current mirror approaches in simulations and extensive testing of its performance as a TIS output stage. The discussion on the presented results feature some important points on the compliance of the posited output stage, most prominent of which is its reliance on large source impedances, which a current-mode stimulator should rather do without.

Future research is encouraged to measure more varied input waveform shapes, and determine proper values for the Taylor expansion coefficients of the posited electrophysiological model. The model should also be further expanded into a spatially distributed version, which takes into account the spatial component of electric field propagation, and the consequential variations in modulation depth of the stimulation waveform. Additionally, the presented output stage requires further validation for different process corners, at higher operational temperatures, and some of the early design assumptions may need to be re-evaluated, particularly the choice of using indirect feedback. These steps will contribute to a viable, spatially selective and power-efficient output stage for temporal interference-based stimulators, to provide patients with better quality of life in the future.

Acknowledgements

Curiosity sparked the beginning of my academic journey, growing into a passion for bioelectronics and ultimately leading me to write about the fascinating topics presented in this thesis. Only through the enthusiastic support and wisdom of my supervisor, Wouter Serdijn, could this thesis take shape—studying bioelectronics under his wing, along with my peers in the Bioelectronics section at the TU Delft, truly made me feel like I am part of a very important cause.

Recognition also goes to the members of my committee, Anton Montagne and Chris Verhoeven, who have always fascinated me with their breadth of knowledge on the topic of structured electronics design, and their priceless efforts at keeping the 'art' alive.

Studying the intricacies of bioelectronics could also not have been possible without all of the friends I have made since the start of my studies in Delft. The experiences I have shared with them led to many core memories that I could never hope to forget. I also especially want to thank my parents, siblings, and the close friends I consider family, for their continued support, and dealing with my particular anthics over all these years. All of the love and warmth I have received from them kept me grounded and moving forward, which I am very grateful for.

Among the many who encouraged me, my grandparents deserve some special acknowledgment, for always reminding me that there is a lot more to life than academic prestige, or being the best at the things I do. Not to be forgotten is my coffee percolator, whose unwavering support (in the form of exorbitant amounts of caffeine) made every deadline just a little bit more manageable.

Joris C. de Koning
Delft, The Netherlands
August 2025

Chapter 1

Introduction

Electrical stimulation therapies for the treatment of medical conditions like cardiac arrhythmia, Parkinson's disease, or epilepsy are already widely adopted, displaying the clear benefits to the electrical control of medical symptoms and its positive effect on a patient's quality of life. The most well-known application of medical electrical stimulation therapies is the artificial cardiac pacemaker; a neuromodulation device used for the treatment of cardiac arrhythmia. A total of 1.14 million pacemakers were implanted in 2016 [1], which only increased over the following years. Vagus nerve stimulation (VNS) has also seen widespread adoption. Since its first international controlled trials for the treatment of epilepsy in 1994 [2, 3], more than a few hundred thousand VNS devices have been implanted worldwide [4]. In its application for drug-resistant epilepsy, the average amount of seizures were reduced by 36 % over a period of 6 months of VNS therapy, growing to an average of 70 % over a period of 3 years [5]. Beyond the control of seizures, stimulating the vagus nerve also finds its applications in the treatment of depressive symptoms, as documented in long-term follow-up studies of patients receiving VNS therapy [6].

Even though these medical conditions are noticeably improved, fully-implanted neuromodulation devices, like the pacemaker and vagus nerve stimulator, are not without their fair-share of caveats. Featured among the negative consequences of these devices are: risks related to tissue infection, invasiveness of fully-implanted stimulators and electrodes, tissue heating concerns, battery replacement surgeries, damage inflicted to nerve tissue in operation, and other complications of electrically mediated therapy. Even so, ongoing monitoring and iterative refinement of existing system designs will, over time, be able to improve on these issues. One of the issues that is often addressed in neural stimulation is the specificity of stimulation, or the spatially selective stimulation of highly specific parts of a nervous structure. Spatially indiscriminate stimulation of a nerve can, for example, in the case of vagus nerve stimulation, bring about severe side-effects relating to patient quality of life, even if the original medical goal for the treatment of primary symptoms is achieved.

Temporal interference stimulation (TIS) is a relatively new neuromodulation method that attempts to address problems relating to invasive treatments and the side-effects incurred by spatially indiscriminate neuromodulation. It boasts high spatial selectivity, which is brought about by introducing two or more electric fields to the nerve tissue, which interfere, and create a stimulation waveform that can reach deeper structures of the nerve, without directly inserting an electrode in the targeted area of stimulation.

This thesis addresses gaps in knowledge of the design and development of a spatially selective vagus nerve stimulator based on temporal interference stimulation, with a focus on power-efficiency considerations. The specific topics that are addressed are:

1. The insufficient understanding of fundamental electrophysiological mechanisms governing temporal interference stimulation in peripheral nerve cells;

2. The power-efficiency of power supply regulation and compliance of output stage circuits for current-mode stimulation of nerve tissue;

3. The design of a power-efficient output stage and neuromodulation system architecture for use in temporal interference stimulation of the vagus nerve.

The remainder of this chapter presents the fundamental principals and background information necessary for the analysis carried out in the following chapters. Topics range from an introduction to human nerve anatomy, to the circuit design of output stage current sources for neural stimulators. Chapter 2 provides an overview of the current knowledge on temporal interference stimulation and formulates clear problems that need to be addressed, covering complications regarding conventional mechanistic modelling of TIS, and existing implementations of

TIS systems. Additionally, a system architecture, aimed at achieving power-efficient TIS-based stimulation, is proposed. The chapter concludes with a clear formulation of the analytical research objectives, which are addressed in the subsequent chapters. Chapter 3 introduces and discusses a model to accurately describe observed nonlinear neuron responses under influence of interfering electric fields, and validates model outputs in comparison to experimental data in literature. Chapter 4 evaluates the performance of the proposed transistor-based circuit design through simulation, and compares performance metrics to conventional output stages. Finally, chapter 5 summarizes the reported findings and scientific contributions of this work, and outlines possible directions for future research.

1.1 Human nerves and the electrophysiological properties of neurons

1.1.1 The anatomy of the human nerve and nerve cells

The human nervous system can be likened to a system with feedback, where sensory signals are taken in and conducted along the peripheral nervous system (PNS), which go back to the controller known as the central nervous system (CNS), as shown in Fig. 1.1. The CNS interprets the received information by a process called integration, and derives a result that determines the activation of nerves that go back along the PNS to various motor organs, like the muscles for voluntary movement of the legs, or involuntary regulatory signals for the body at rest [7].

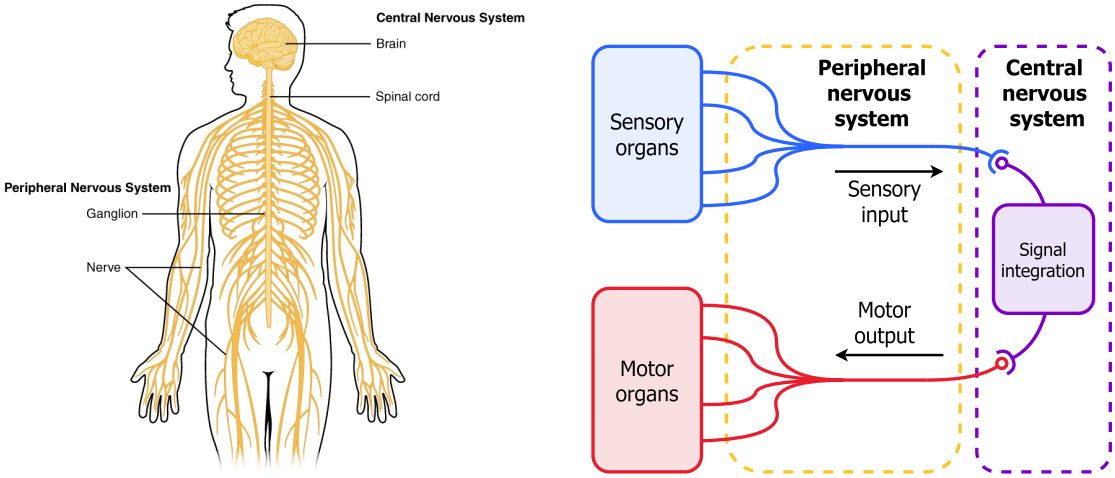

(a) Nervous system structure (from [8]).

(b) The nervous system feedback loop.

Figure 1.1: **(a)** The central nervous system (CNS) consists of the brain and spinal cord. The peripheral nervous system (PNS) consists of all other nerves that reach the further extremities of the human body. **(b)** The PNS and CNS act like a feedback system: sensory organs transmit input signals along the nerves of the PNS, which the CNS integrates and processes. The CNS then sends a motor output signal back to the PNS, completing the loop.

A nerve consists primarily of nerve fascicles and, to a lesser extent, of blood vessels. Nerve fascicles are bundles of nerve cells (also called neurons), that are wrapped in a protective layer, called the perineurium (as shown in Fig. 1.2). Neurons are the main functional unit that make up a nerve, and they are able to send and receive signals when chained together. The neurons that receive a sensory signal and return it to the CNS are called afferent, whereas the neurons that carry a signal from the CNS out to the PNS are called efferent neurons.

The main neuron type of the CNS is the multipolar neuron, which features multiple dendrites branching from the main cell body, called the soma (as shown in Fig. 1.3). The longest dendritic branch is called the axon, which may be alternately enveloped by electrically insulating myelin sheaths. The axon ends in the axon terminals, which release neurotransmitters to the somatic dendrites of other (multipolar) neurons, such that a signal can be carried from one neuron to the other. The multipolar neurons inside the body are mostly interneurons, that feed sensory signals from the PNS to the CNS for integration, and then directly back out to the PNS motor neurons [7].

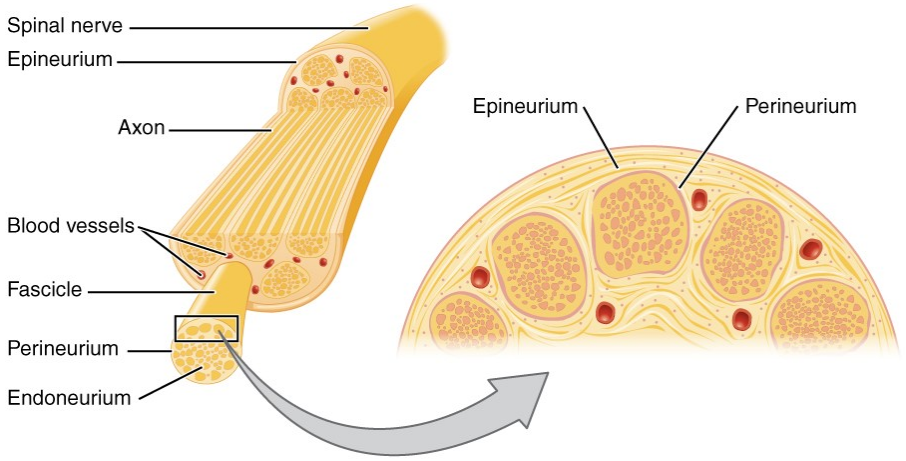

Figure 1.2: The anatomy of a human nerve (from [9]).

Another relevant neuron type is the pseudounipolar neuron (as shown in Fig. 1.3b), which is mainly found in the PNS as the sensory receivers of cranial nerves. Cranial nerves are nerves surrounding the head of the human body. The soma of a pseudounipolar neuron is located further from the receptive region of the axon, closer to the middle of the axon length.

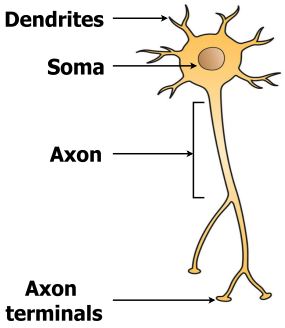

(a) A multipolar neuron (adapted from [10]).

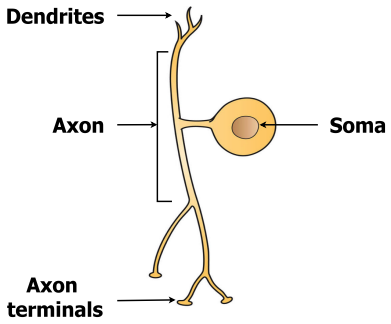

(b) A pseudounipolar neuron (adapted from [10]).

Figure 1.3: (a) Multipolar neurons are the main neuron type of the CNS, which feed signals from sensory neurons to the CNS for signal integration. **(b)** Pseudounipolar neurons are mainly concerned with sensory signal transmission, mostly found in longer extensions of the PNS [7].

Much like a normal cell membrane, the neuron membrane consists of a phospholipid bilayer that forms a mechanical barrier between the inside of the cell and the extracellular fluid, as shown in Fig. 1.4. Scattered across the lipid bilayer are larger protein structures that facilitate communication between the inside and outside of the cell membrane. Particular to the topic of neuron stimulation are proteins that are called gated ion channels, which let specific ions pass the neuron membrane. Typical gated ion channels include:

(a) **Ligand gated ion channels**, which open in response to the binding of a ligand (a specific chemical species) on a receptor [11].

(b) **Mechanically gated ion channels**, which open in response to mechanical deformation of the ion channel [12].

(c) **Temperature gated ion channels**, which open in response to temperature variations around the ion channel [13].

(d) **Voltage gated ion channels**, which open in response to changes in the electric potential across the membrane [14].

(e) **Ungated ion-channels**, which are channels that are always open, aptly called leakage channels.

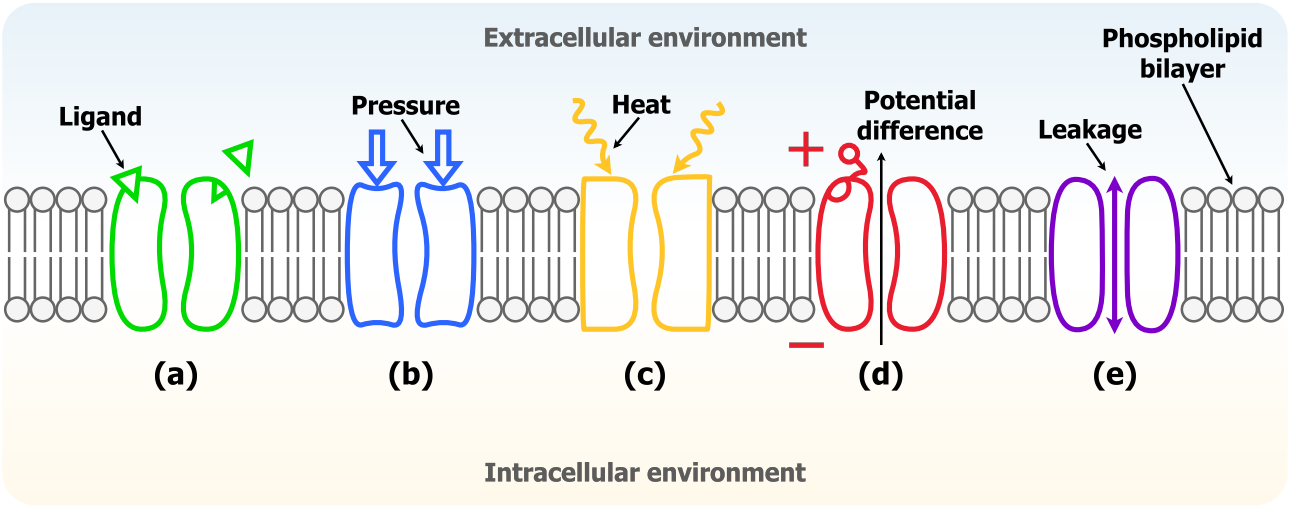

Figure 1.4: Typical gated ion channels featured in the phospholipid bilayer of the neuron membrane. Each ion channel contributes to establishing the neuron membrane potential, with varying amounts of influence. Most relevant to the context of this report are the voltage gated ion channels in **(d)**, which activate based on deviations from the resting membrane potential.

The concentrations and constant flow of certain ions in and around the membrane, with either positive or negative electrical charge, establishes a voltage potential difference across the neuron membrane at rest. It is the disturbance of this resting membrane potential that is the basis of communication between the neurons, caused by changes in ion concentrations or changes in membrane permeability for a certain ion.

1.1.2 Membrane potential and neuron stimulation

The interaction of electrical stimuli with neurons is mediated by the dynamic behaviour of particularly chlorine (Cl^-), sodium (Na^+), and potassium (K^+) ions flowing through gated ion channels in the neuron membrane [12, 15]. In this section, the membrane dynamics behind ionic current flow and neural stimulation are briefly covered.

Resting membrane potential

Neurons either receive, conduct, or transmit signals by means of electrochemical conduction caused by varying concentrations of charge-carrying ions around the neuron membrane, or through chemical conduction between neurons with the use of neurotransmitters [15]. The cell membrane acts like a separation of charge brought about by the ions surrounding the neuron membrane, which causes a potential difference V_m in volts in intracellular ν_i and extracellular ν_o voltage potential that is defined as:

$$V_m = \nu_i - \nu_o. \tag{1.1}$$

At equilibrium, neurons maintain a potential difference across their membrane that is typically around –70 mV to –90 mV relative to the the extracellular environment, which is brought about by the differences in concentrations and permeability of chlorine (Cl^-), sodium (Na^+), and potassium (K^+) ions. The equilibrium is dynamically mediated by the Na^+/K^+-ATPase pump, and leakage current through Cl^- leak channels. The Na^+/K^+-ATPase pump is a special kind of membrane protein that trades Na^+-ions for K^+-ions using energy stored in ATP molecules.

Changes in the membrane potential result in either graded potentials or action potentials. Graded potentials are small, local currents that move along the membrane, but dissipate quickly at further distances because of leakage through ion-channels. Action potentials are the main long-distance signals that travel over the entire length of the axon. Both graded and action potentials can make the membrane potential become more positive or negative with respect to the resting potential, which is respectively called depolarization or hyperpolarization.

Ion flow is governed by three factors, namely: the ratio of ion concentrations inside and outside the neuron cell membrane, the (resting) voltage across the membrane, and the membrane permeability to certain ionic species that is regulated by gated ion channels.

The resting potential V_r and its relation to the ion concentrations and permeabilities of the neuron membrane at equilibrium is given by the Goldman-Hodgkin-Katz (GHK) equation [15]:

$$V_r = \frac{RT}{F} \ln\left(\frac{P_K[K]_o + P_{Na}[Na]_o + P_{Cl}[Cl]_i}{P_K[K]_i + P_{Na}[Na]_i + P_{Cl}[Cl]_o}\right), \tag{1.2}$$

where T is the absolute temperature in Kelvin (usually assumed to be at a body temperature of 37 °C ≈ 370 K), F is the Faraday constant ($F = 9.649 \times 10^4$ C/mol), R is the gas constant ($R = 8.314$ J/mol/K), P_X is the permeability coefficient of the membrane for a particular ionic species X, and $[X]_i$ is the intra- and $[X]_o$ is the extracellular concentration for a particular ionic species X in mol per litre.

The influence of an individual ionic species for establishing the equilibrium potential inside the nerve cell is given by the Nernst potential equation. For example, the individual influence of K^+-ions is given by:

$$V_K = \frac{RT}{\xi F} \ln\left(\frac{[K]_o}{[K]_i}\right), \tag{1.3}$$

where ξ is an integer number of the amount of valence electrons in the outer shell of the specific ionic species. Due to the much larger permeability of K^+ ions ($P_K >> P_{Na}, P_{Cl}$), it is usually assumed to be the main contributor to the equilibrium potential. The electromotive force (EMF) that moves the ions around the membrane is then conventionally formulated as:

$$EMF = V_m - V_K = \nu_i - \nu_o - V_K, \tag{1.4}$$

which is approximately zero at equilibrium.

Membrane depolarization and threshold current for stimulation

When the neuron membrane potential depolarizes, and reaches a certain threshold voltage potential (about –60 mV [15]), an action potential (AP) is created, as illustrated in Fig. 1.5a. An AP is a large abrupt spike of depolarization followed by repolarization, of which the size and shape are independent of stimulus intensity or duration. The AP is an all-or-nothing phenomenon, which means that the AP either happens entirely, or the AP does not happen at all. When the AP does happen, all voltage-gated ion channels in the surrounding area of the initial stimulation are opened, causing a large influx of Na^+-ions through the membrane. After the initial depolarization, the AP enters a phase of repolarization. Repolarization is achieved by the outflow of K^+-ions to the extracellular environment through K^+-ion channels, which open slightly slower than the Na^+-ions. The last phase of the AP is characterised by an overshoot of the repolarization into a relatively hyperpolarized state.

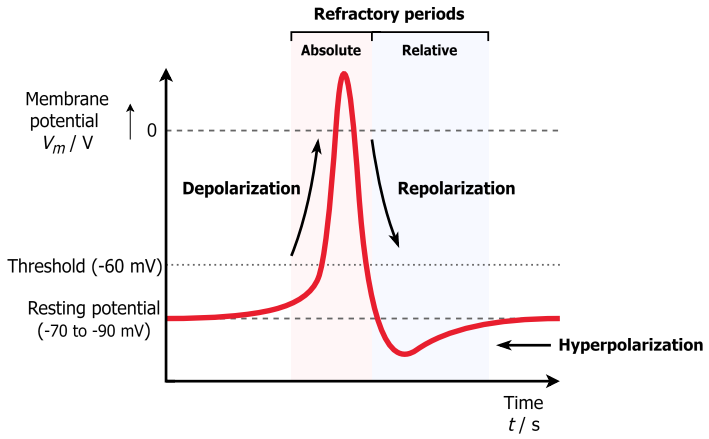

(a) Membrane potential when an action potential is generated.

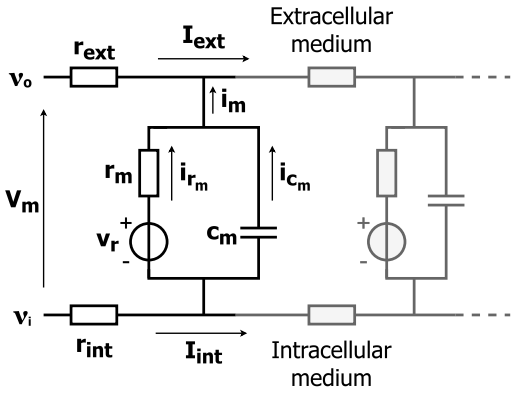

(b) The cable model equivalent circuit.

Figure 1.5: **(a)** The fast depolarization of the membrane potential during an action potential is caused by an influx of Na^+-ions through voltage-gated ion channels in the neuron membrane. The membrane potential quickly repolarizes due to an outward flow of K^+-ions, and overshoots on the return, hyperpolarizing the membrane. **(b)** The equivalent circuit of the cable model is shown. The cable model is a second order differential equation that describes the individual contributions of current flow through, and across, the neuron membrane.

As the Na^+-ion channels are open during the full duration of the depolarization phase (and part of the repolarization phase), the neuron will not be able to respond to other stimuli that are received at this time. This part of the AP is called the absolute refractory period, and is the basis behind the all-or-nothing property of the neuron. In the period of time following the absolute refractory period (when the Na^+-ion channels are closed and the K^+-ion channels are open), it is possible to create another action potential, albeit with a stronger stimulus threshold than before depolarization; the neuron enters a relative refractory period, where it is relatively insensitive to depolarization until it reaches resting membrane potential level.

When an initial graded potential causes an influx of Na^+-ions through the gated ion channels, and an action potential is achieved, it also allows the membrane potential in the direct vicinity of the neuron axon to depolarize. Its influence on the neighbouring area causes a cascading of APs along the axon length, effectively establishing propagation of the original signal. As such, neurons do not 'conduct' current using electrons, like through a wire, but rather through the cascading of local membrane depolarizations caused by chemical species; it is an *ionic* current flow.

An equivalent electrical circuit model for the mechanism behind ionic current flow in the neuron membrane is presented in the cable model of the neuron axon, as shown in Fig. 1.5b. The cable model comprises a second-order differential equation that describes the behaviour of the axial membrane currents I_{int} and I_{ext} in amperes per meter, radial membrane current i_m in amperes per square meter, and deviation of the membrane potential from the resting potential $V_d = V_m - V_r$ in volts, in time and space (along the axon position x in meters), such that:

$$\frac{\partial^2 V_d}{\partial x^2} = (r_{int} + r_{ext}) i_m, \tag{1.5}$$

with

$$\frac{\partial V_d}{\partial x} = \frac{\partial V_m}{\partial x} = \frac{\partial \nu_i}{\partial x} - \frac{\partial \nu_o}{\partial x} = -I_{int} r_{int} + I_{ext} r_{ext}, \tag{1.6}$$

$$\frac{\partial V_d}{\partial t} = \frac{\partial V_m}{\partial t} = \frac{\partial \nu_i}{\partial t} - \frac{\partial \nu_o}{\partial t}, \tag{1.7}$$

and

$$i_m = -\frac{\partial I_{int}}{\partial x} = \frac{\partial I_{ext}}{\partial x}, \tag{1.8}$$

where r_{int} and r_{ext} are in Ohm per meter, r_m is in Ohm meter, and c_m is in Farad per meter. A general solution for the propagation of a stimulus is given by:

$$V_d = V_{d0} e^{-x/\Lambda}, \tag{1.9}$$

where V_{d0} is the initial membrane potential deviation in volts, and the length constant Λ is given by:

$$\Lambda = \sqrt{\frac{r_m}{r_{int} + r_{ext}}}. \tag{1.10}$$

The part of the model that governs local action potential generation is the membrane current i_m, which is the summation of the current through the membrane resistance r_m and the current through the membrane capacitance c_m:

$$i_m = i_{r_m} + i_{c_m}. \tag{1.11}$$

Using the general cable equation of (1.5), it can be described as an ordinary second-order differential equation with time constant $\tau_m = r_m c_m$ as:

$$\Rightarrow \frac{1}{r_{int} + r_{ext}} \frac{\partial^2 V_d}{\partial x^2} = \frac{V_d}{r_m} + c_m \frac{\partial V_d}{\partial x},$$

$$\Rightarrow -\Lambda^2 \frac{\partial^2 V_d}{\partial x^2} + \tau_m \frac{\partial V_d}{\partial x} + V_d = 0. \tag{1.12}$$

The membrane time constant is a measure of the time it takes for the signal to be able to depolarize the neuron. It was experimentally observed that shorter duration stimulation pulses require higher stimulation amplitudes, whereas longer stimulation pulses can elicit action potentials at lower amplitudes [15, 16].

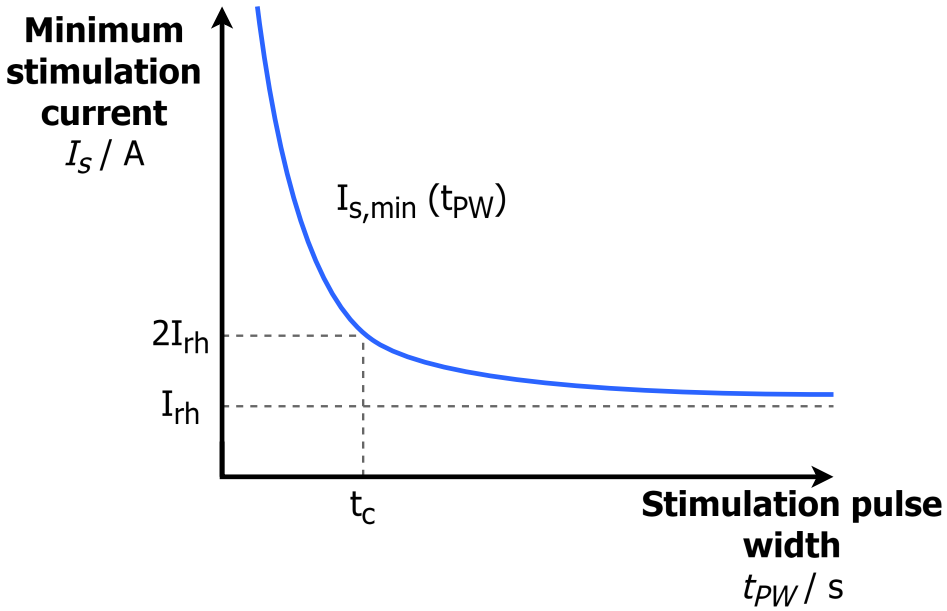

Figure 1.6: Depending on the length of the pulse width t_{PW} used in neurostimulation, different minimum current magnitudes are needed for stimulation. The rheobase current I_{rh} is the current for which no stimulation will happen. The chronaxy t_c is the pulse width duration at which twice the rheobase current is needed for stimulation.

This phenomenon can be related back to the charging of the membrane capacitance for a given stimulus duration, leading to the formulation of the strength-duration relation:

$$I_{s,min}(t_{PW}) = \frac{I_{rh}}{1 - e^{-t_{PW}/\tau_m}}, \tag{1.13}$$

where $I_{s,min}$ is the minimum stimulation current in amperes needed for a specific stimulation pulse width duration t_{PW}, and the rheobase current I_{rh} is the asymptotic threshold current below which neuron stimulation can never occur.

Returning to the case of the cable model, when axial propagation currents I_{int} and I_{ext} are eliminated (through a technique called spatial clamping), the radial membrane current i_m remains. When also the capacitive membrane current i_{c_m} is eliminated by voltage clamping, only the radial membrane resistance i_{r_m} current contributes to the total membrane current. This current consists of the individual contributions of ionic currents, which each have a defined magnitude and direction through the membrane. These membrane current constituents can be individually measured as potassium, sodium and leakage currents, by pharmacologically subtracting (blocking) the ionic currents that are not measured. These currents have (nonlinear) differences in electrochemical gradients, brought about by the gating mechanisms of the ion channels.

The Hodgkin-Huxley conductance model

The mechanism behind the gating of the various ions, and the consequential differences in electrochemical gradients, are still unknown. One of the posited models for this phenomenon is presented in the Hodgkin-Huxley conductance model [17](also described in [15, 18]), that represents the nerve membrane current i_m as individual components of ionic current and capacitive current, as:

$$i_m = i_{r_m} + i_{c_m} = i_{Na} + i_K + i_L + c_m \frac{\partial V_d}{\partial x}, \tag{1.14}$$

where i_{Na} and i_K are respectively the sodium and potassium currents in amperes per square meter, and i_L is the ionic current of Cl^--ions, which is seen as a constant leakage current. The model posits that the electrochemical gradients can be represented by three ionic conductances, as shown in Fig. 1.7.

The conductance and Nernst potential of a specific ionic species X are shown as g_X, and V_X respectively. The ionic conductances are defined as:

$$g_K = \frac{I_K}{V_m - V_K}, \tag{1.15}$$

$$g_{Na} = \frac{I_{Na}}{V_m - V_{Na}}, \tag{1.16}$$

and

$$g_L = \frac{I_L}{V_m - V_L} = \text{ constant}, \tag{1.17}$$

where I_X is in amperes per square meter, g_X is in Siemens per square meter, and V_X is in volts.

The model further hypothesizes the existence of 'gating particles' that control the gating of the sodium and potassium ion channels, which feature a certain probability to flip the state of the ion channel between a 'blocking' or 'non-blocking' state (essentially 'open' or 'closed' states, respectively). The conductance of the sodium and potassium channels is defined as a maximal conductance value times the probability of the gates to open, which is written as:

$$g_K = g_{K,max} a^4, \tag{1.18}$$

and

$$g_{Na} = g_{Na,max} b^3 c, \tag{1.19}$$

where a, b, c are dimensionless gating particle variables, that are assumed to be independent particles that contribute to the open or closed states of the ion channel gates. For K^+-ion channels, four identical a-particles must be in a non-blocking state to open the ion channel. Similarly, for the Na^+-ion channels, three b-particles and one c-particle needs to be in a non-blocking state for the ion channel to open.

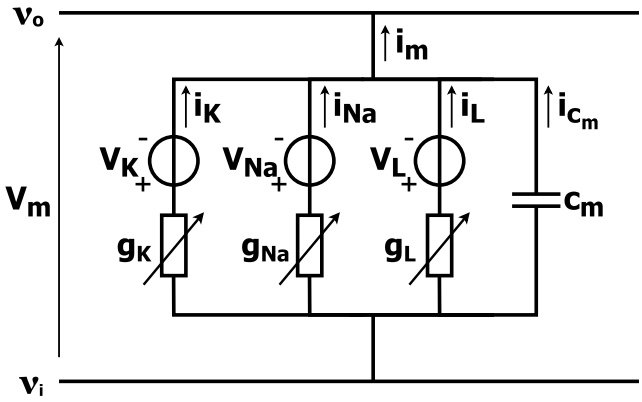

Figure 1.7: The Hodgkin-Huxley conductance model assumes each ionic membrane current can be assigned an individual conductance and Nernst potential. The magnitude of conductance is dynamically defined by posited *gating particles*.

The model thus posits that when the probability of the gating particles entering a non-blocking state increases, the conductance of a certain ion increases. The amount and speed at which the probability changes differs per ion, which is captured in the individual transfer rate coefficients of a certain gating particle. These transfer rates are in a negative feedback loop during depolarization, which brings the membrane potential back to equilibrium.

In summary, when electrical stimulation causes a voltage difference that enables the voltage gated Na^+-ion channels to open, membrane depolarization is started. When the membrane potential reaches a certain value after depolarization, the probability of the gating particles particular to Na^+-ion channels (b- and c-particles) going into a blocking state rises, which will eventually cause the ion-gate to block the influx of Na^+-ions into the membrane. The electrical stimulation also causes the voltage gated K^+-ion channels to open, but they open much slower than Na^+ channels due to differences in transfer rate coefficients of the gating particle that is particular to K^+-ion channels (a-particles). Their mass flow is, in contrast to Na^+ ions, to the outside of the neuron membrane. This means the overly positive intracellular charge is actively being returned to equilibrium by injecting charge to the extracellular environment. This negative feedback causes the characteristic repolarization, after which the probability for the gating particles of K^+-ion channels to go into a blocking state increases as the membrane reaches equilibrium.

1.2 Neuromodulation

The neuron membrane potential can be affected by various types of stimulation due to the different types of ion channels in the neuron membrane that are particular to a certain stimulus. Stimulation methods may include mechanical or temperature-based stimuli, such as those used in ultrasound stimulation [19, 20]; chemical stimuli delivered through pharmacological agents [21, 22]; or, in some experimental cases, light-based stimuli as seen in optogenetics [23, 24]. However, most commercial neuromodulation devices employ electrical stimulation to generate action potentials in the neuron, which is also the focus of this report. As such, the characteristics of electrical neuron stimulation, and the electrochemical interaction of nerve tissue and electrical neuromodulation devices is covered in this section.

1.2.1 Targeted electrical stimulation

Electrical neuromodulation is the process by which the gated ion channels in neurons are regulated by the delivery of targeted electrical stimuli to specific parts of the central or peripheral nervous systems, such that the resting membrane potential is disturbed and action potentials are created. This concept is used in medically implanted neural stimulation devices for, for example, the treatment of Parkinson's disease through deep brain stimulation (DBS), or for the treatment of paralysis through spinal cord stimulation.

The interaction of the electrical stimulator device with the tissue is mediated by electrodes, which are the interface between the biological tissue and the stimulator electronics. The stimulation of nerve tissue is therefore a transduction of electrical energy (electrical current) into chemical energy (ionic current). The electric fields generated by the electrode ends can cause a local graded potential by injecting charge into the tissue [15]. The graded potential eventually causes an action potential if the stimulus is either a high magnitude, short duration pulse, or when the pulse is maintained at a lower magnitude for an extended period of time (as per the strength-duration relation shown in Fig. 1.6).

Electrode-tissue interface impedance

The interfacing of the electrodes to the tissue can be modelled as an equivalent electrical circuit, for which the current through the tissue is determined by the electrode-tissue interface (ETI) impedance [25]. The ETI mainly consists of two mechanisms for charge transfer, the first of which is found at the interface between the material of the electrode and the biological tissue, where an electrical double layer is formed [26, 27]. This layer comprises an inner Helmholtz layer, which is formed due to the relative charge on the electrode, and a diffuse layer of ions in the tissue medium. The electrical double layer is the main charge storage mechanism of the ETI, which converts charge carried by electrons into charge carried by ions in the tissue. The second charge transfer mechanism is through a Faradaic impedance, which involves electrochemical reactions at the electrode surface. Electrons from the current flowing through the electrode are transferred across the interface, which leads to oxidation and reduction of ionic species, as illustrated in Fig. 1.11. The reactions are considered a charge transfer resistance, and is therefore called the Faradaic resistance of the ETI.

Linear models of the ETI are simplified representations of the ETI interactions, often practically used for simulation, which model the nerve tissue response to stimulation. The most basic representation of the ETI that is frequently employed in initial electronic design, features a parallel faradaic resistance and double-layer capacitance in series with a tissue resistance, as shown in Fig. 1.8a. Where R_{tis} stands for the series tissue resistance in the nerve, and a series parallel combination of the double-layer capacitance C_{dl} and Faradaic impedance. The Faradaic impedance is most often modelled as a Faradaic resistance R_F at this level.

More sophisticated linear models, like the Randles circuit, see the Faradaic impedance as a series combination of charge transfer resistance R_{ct} and Warburg impedance Z_W [26]. For which the Warburg impedance describes diffusional resistance, or, the opposition to the flow of ionic species created in the Faradaic electrochemical reactions.

In measurement of general electrodes in solution, it is also often observed that the capacitance of the double-layer capacitor disperses, meaning the idealized capacitor in the model does not represent the physical processes accurately [26]. Instead, in the Debye model, the capacitor is replaced by a constant phase element (CPE), of which the impedance is defined as:

$$Z_{CPE} = \frac{1}{(j\omega)^{\varphi} Q_{dl}}, \tag{1.20}$$

where $\varphi \leq 1$ is a dimensionless constant phase element exponent, ω is the radial frequency in radians per second, j is the imaginary unit, and Q_{dl} is the double-layer capacitance, but with a redefined relative unit in $F/(m^2 s)$.

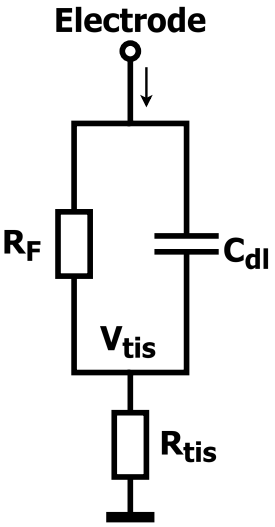

(a) Basic linear model.

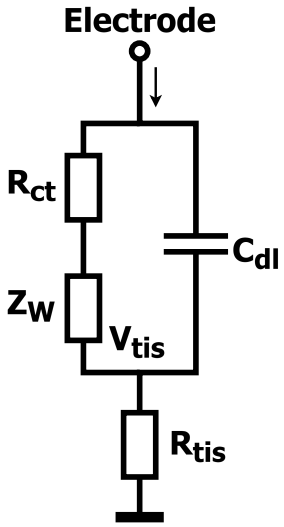

(b) Randles equivalent circuit model.

Figure 1.8: (a) The basic linear model uses a Faradaic resistance R_F and double-layer capacitance C_{dl} to model the ETI as a leaky capacitor. An even simpler model completely removes the Faradaic resistance altogether. **(b)** The Randles equivalent circuit model takes into account diffusional resistance with the added Warburg impedance Z_W. In the Debye model, the ideal capacitor C_{dl} is replaced for a constant phase element impedance Z_{CPE}, which accounts for capacitance dispersion.

The above models are characteristically defined by discrete lumped-elements, which define quantities like voltage and current at idealized points in a circuit in time. In contrast, distributed models acknowledge that the related physical quantities are distributed spatially throughout the system, where voltages and currents are described in both time and space, necessitating the use of partial differential equations. However, due to the scale of nerves (which are roughly a few millimetres in diameter [28, 29]) and the use of stimulation frequencies that have wavelengths far exceeding the size of the nerve (usually below 10 kHz, which corresponds to a wavelength of about 22 km in water with refractive index of 1.33), the tissue is often considered quasi-static, meaning the lumped-element model is adequate for stimulation that does not depend on spatial interactions of induced charge within the tissue.

While the electrochemical processes at the electrode-tissue interface and the intrinsic dynamics of neurons are fundamentally nonlinear, linear models can often suffice for initial simulations of the response of neurons to electrical stimulation. The choice of model therefore heavily depends on the intended outcome of the question at hand.

Low-frequency stimulation preference of neurons

Aside from the electrode-tissue interface, the electrical properties of the nerve itself significantly influence the efficacy of stimulation overall. Both the frequency-dependent conductivity and the inhomogeneous nature of human nerve cells affects the electric field distribution in the nerve [30].

A low stimulation frequency is chosen in view of this fact, as the threshold currents for electrical stimulation of neurons are generally lowest for stimulation frequencies below 200 Hz [31, 32]. The sensitivity of neurons decreases at stimulation frequencies greater than 1 kHz [33], and transitions into full conduction block beyond 10 kHz [34]. Conduction block or inhibition is the phenomenon where high-frequency alternating current leads to a steady-state of membrane depolarization, which either completely blocks the transfer of signals or makes that the neuron is less likely to generate action potentials.

At large, it can therefore be posited that the neuron membrane acts like a low-pass filter (LPF), for which the time constant $\tau_m = r_m c_m$ defines its frequency response; higher-frequency components are attenuated more, requiring higher stimulation amplitudes to achieve threshold values. This phenomenon therefore sets an upper bound to the usable (physiologically relevant) stimulation frequencies. The underlying mechanism for this sensitivity to lower frequencies is yet unknown. The slower mass flows of K^+-ion channels during repolarization, which cause the delay in the refractory period [17], and an increase in threshold membrane potential required for generating a subsequent action potential, are posited to bring about its inability to respond to fast voltage changes [34].

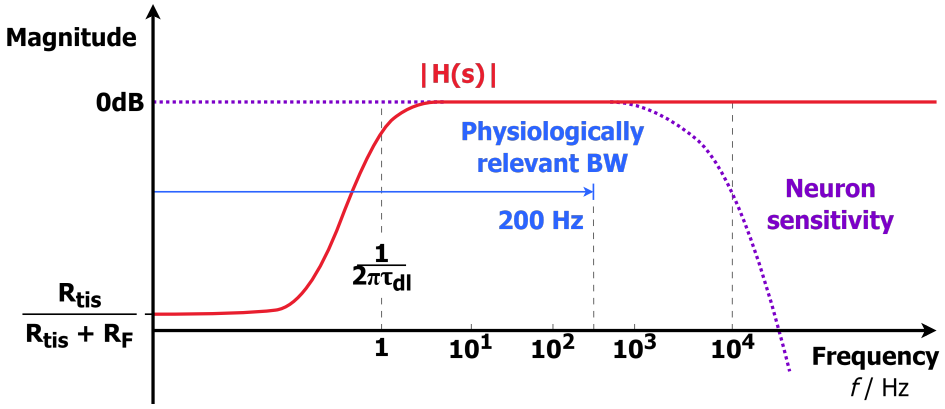

Figure 1.9: The transfer function of the electrode voltage to the tissue voltage approaches unity when the stimulation frequency lies beyond the pole added by the double-layer impedance. Neurons are most sensitive in the physiologically relevant bandwidth, between (0 to 200)Hz. At frequencies higher than 1 kHz, sensitivity to stimuli decreases, transitioning into full conduction block beyond 10 kHz.

In other words, when the stimulation waveform frequency is slow enough for the ions to follow, action potentials can reliably be generated for a finite amount of time — a phenomenon that resembles the behaviour of an LPF.

In the following analysis, unless explicitly mentioned otherwise, the simple model of Fig. 1.8a is chosen to describe the neuron membrane charge dynamics. The value of R_{tis} is in this case picked to be a reasonable value for the chosen stimulation method. The transfer function of the ETI voltage V_{ETI}, to the tissue voltage V_{tis}, can then be seen as:

$$H(s) = \frac{V_{tis}}{V_\ell} = \frac{R_{tis}}{R_{tis} + R_F || \frac{1}{sC_{dl}}} = \frac{R_{tis} + sR_{tis}R_FC_{dl}}{R_{tis} + R_F + sR_{tis}R_FC_{dl}}, \tag{1.21}$$

where s is the complex frequency variable of the Laplace transform. In the case of neural stimulation, the parameter values for R_F and C_{dl} introduces a time constant τ_{dl} that depends strongly on the electrode material and geometry, but in general they tend to be very large in magnitude (for example, R_F is often greater than 100 kΩ and C_{dl} is often greater than 1 µF in DBS [35]). This causes a dominant pole at $\omega_{dl} = \frac{1}{R_FC_{dl}}$, created by the large double layer capacitance and faradaic resistance values. To minimize the amplitude of stimulation pulses, neurostimulators typically operate in a bandwidth ranging from ω_{dl} up to a physiologically relevant frequency limit set by the neuron's intrinsic sensitivity to low-frequency stimulation.

1.2.2 Neural stimulator systems

Electrical neuromodulation hinges on the precise interaction of electrical neuromodulation circuits with the biological and electrochemical properties of the neuron. As such, any electrical neuromodulation device has to consider some important factors relating to the safety, efficiency, and long-term operability of the device. These considerations further relate to the system components, which typically consist of an output stage connected to the electrodes and electrode leads, a power source, logic and control circuitry for pulse generation, and a voltage regulator to manage supply voltage differences between power source and circuitry, as shown in Fig. 1.10a. The neuromodulation device can be located either fully outside the body, partially inside the body, or fully implanted inside the body.

An example of fully external electrical neuromodulation devices are transcutaneous electrical nerve stimulation (TENS) devices. TENS devices generate an electric field between electrodes that pass through the skin, hence, it is *transcutaneous*. TENS units are often used for pain relief by stimulating nerves around an affected area on the body, which inhibit pain signals from reaching the brain [36, 37]. TENS units are often portable, and non-invasive, meaning they do not reside anywhere inside the body, and are often used to relieve pain experienced by arthritis, back pain, or general muscle soreness. Due to the way the electrical stimulation is spatially non-discriminate, the stimuli are not specific to certain nerves whatsoever, generally affecting large areas of the body.

In the context of neuromodulation, the degree of specificity, or spatial selectivity, refers to how precisely a device can target the desired area of stimulation. A neuromodulation device that has high specificity can selectively stimulate only the intended nervous structure, avoiding unnecessary stimulation of surrounding areas. TENS units therefore feature a very low specificity, due to its spatially-indiscriminate stimulation of the nerve tissue surrounding the affected target area.

An example of a neuromodulation device that is partially implanted inside the body, with a higher specificity than TENS units, are percutaneous tibial nerve stimulators (PTNS), which are used for treating an overactive bladder [38]. The electrode is inserted into the the ankle, and left near the tibial nerve. The pulse generator and most of the electrode lead is located outside the body, which reduces risks related to implantation, like infection or rejection of foreign objects inside the body.

Most well-known neuromodulation devices, like cardiac pacemakers, are fully-implanted systems that can feature multiple ways to implement the location and distribution of system components inside the body. In the case of cardiac pacemakers, the electrodes are implanted more deeply in the body, to reach the heart, as shown in Fig. 1.10b. The body of the pulse generator is often large in size due to the inclusion of a battery and on-chip control circuitry, causing it to be placed directly underneath the skin on the chest [39]. The inclusion of long leads and a battery reduces the long term safety of the device, which will be covered in the upcoming section on biological safety. In other experimental cases, the battery is (largely) removed in favour of wireless power transfer [40]. Wireless power transfer could reduce the size of the neuromodulation device, ensuring highly localized and safe stimulation by putting the pulse generator circuit close to the area of interest. The system may then also include telemetry to communicate with the device and transfer power wirelessly through the tissue.

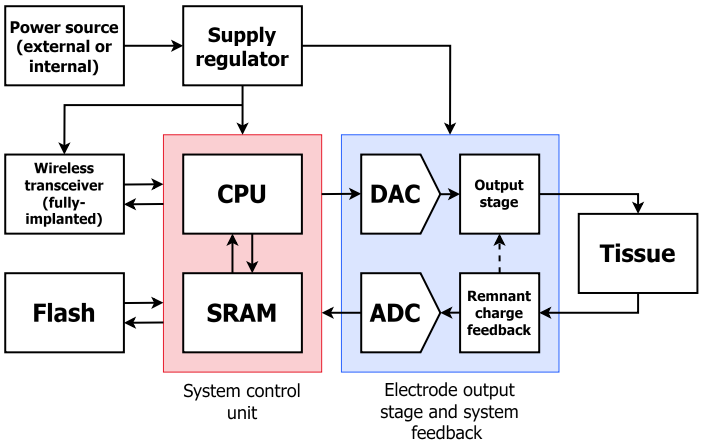

(a) Neural stimulator block diagram.

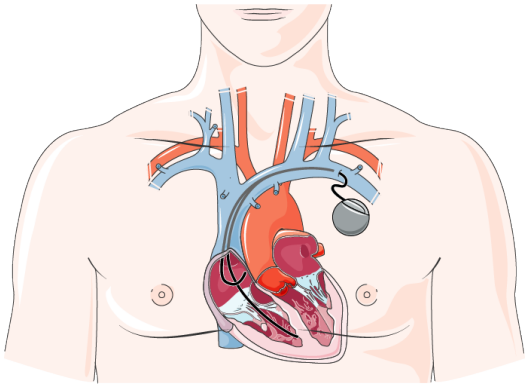

(b) A fully-implanted pacemaker (from [41]).

Figure 1.10: **(a)** Implanted neural stimulator systems use feedback to stay within safe operating limits when driving the output stage. The system control unit may store program execution diagnostics and device history on memory, which can be transmitted to external devices for medical assessment. **(b)** Fully-implanted devices like cardiac pacemakers have long electrode leads to reach the intended area of stimulation. Long electrodes are required when the system features a large battery, which may affect system longevity.

Due to considerations regarding the excessive injection of charge into the body, many implanted neural stimulator systems include feedback from the output stage back to a central processing unit that interprets the received signal and adjusts stimulation by quantifying the difference of the voltage potential on the electrode in respect to tissue ground. For example, in the case of cardiac pacemakers, the output stage sends a current pulse through the tissue, after which the voltage on the electrode is measured and processed. Based on the measurement, the current amplitude at the output stage is adjusted to stay within safe operation limits.

Safe operation limits and general biological safety of neural stimulation

When the voltage on an electrode exceeds a certain safe magnitude due to electrical stimulation, irreversible faradaic electrochemical reactions produce harmful species like hydrogen and oxygen due to electrolysis within the tissue [27], as illustrated in Fig. 1.11. The charge that is introduced to the tissue by electric field stimulation will require the use of charge balancing techniques to prevent the creation of these harmful ionic species.

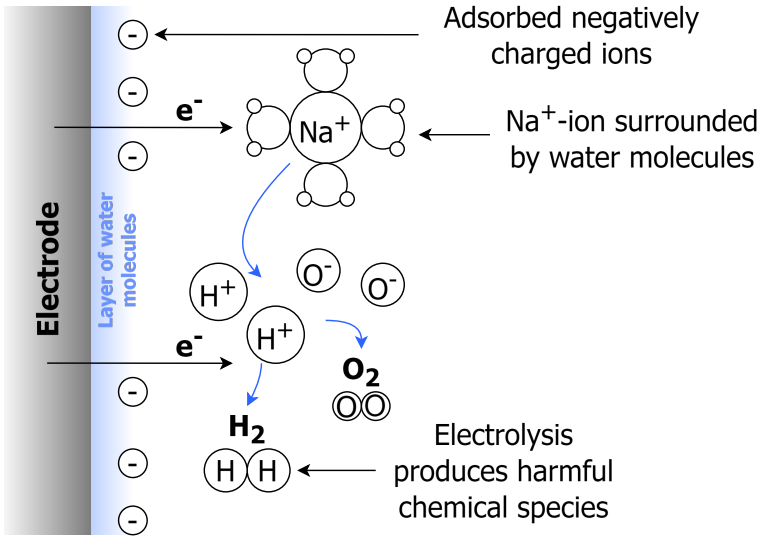

Figure 1.11: Faradaic charge injection causes irreversible chemical reactions due to electrolysis of ions surrounded by water molecules (hydrated cations). Electrolysis may produce harmful species like hydrogen and oxygen when DC stimulation currents exceed certain safety bounds.

Monophasic stimulation only uses cathodic stimuli to stimulate the neuron, as shown in Fig. 1.12a. To stay within safe charge limits, monophasic stimulation relies on the intrinsic charge dissipation of neural tissue, which in turn relies on the membrane time constant τ_m. This is a fairly slow process, which limits the frequency at which action potentials can be generated safely. Monophasic stimulation is therefore often left unused, except for cases in early animal testing [42].

On the other hand, when charge-balanced biphasic current pulses are used for stimulation, the introduced charge is balanced by defining a cathodic phase followed by an anodic phase of equal pulse width and magnitude to leave as little charge on the electrode after both of these phases have finished. The biphasic pulse starts out with a cathodic phase to depolarize the potential in the neuron relative to the extracellular medium, and ends in a relatively positive (anodic) stimulus to cancel the introduced charge by the cathodic phase, as shown in Fig. 1.12b.

Due to the inherent nonlinearity of human (nerve) tissue, and differences in the charge storage of the neuron membrane, the ideal charge-balanced biphasic current pulses do not leave a net zero charge on the electrode after the cathodic and anodic phases have finished. As such, neurostimulator devices often feature control of the magnitude and pulse width of both the cathodic and anodic phase, to optimally control the leftover charge on the electrode, which often further complicates the system feedback and logic circuitry.

Power and area constraints

Complexity of a fully implanted neuromodulation circuit particularly affects the consumed power and on-chip area of the device. These factors are critical constraints in the design of neuromodulation circuits in general, but are a particularly limiting factor for implantable devices. They affect device longevity, patient comfort, stimulation safety, and biological integration of the device into the body.

For example, in devices like pacemakers, the use of a battery as a power source is common. In these devices, the battery takes up a large amount of the device size and weight [43]. This causes the battery and pulse generator housing to be placed far away from the area of interest, at a place where there is enough space for the device to fit. This necessitates the use of long electrode leads, which may cause mechanically induced infection risks, due to the long moment arm that is created by the length of the wire that needs to reach the targeted stimulation area [44, 45]. Older models of cardiac pacemakers also still feature batteries that are not rechargeable, which means a replacement surgery has to take place every few years, further decreasing patient safety and comfort [46]. Newly suggested neuromodulation circuits therefore prefer a wireless power transmission over the bulky, internal power source design of batteries. The external power source would be attached on the body (rather than in the body), transferring its power through a variety of possible modes of power transport through the skin, to the neuromodulation implant inside the body [47]. These power transmission modes can include power transferred by electro-magnetic waves, light, or ultrasound, to name a few.

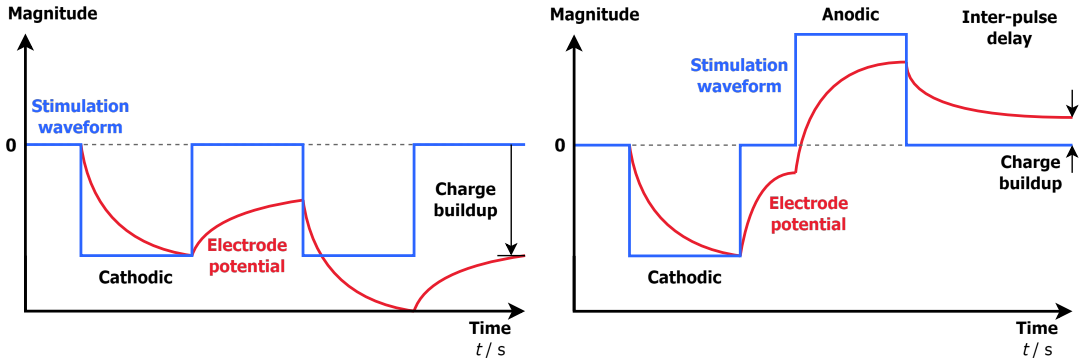

(a) Monophasic stimulation builds up charge.

(b) Charge-balanced biphasic stimulation.

Figure 1.12: (a) Monophasic waveforms tend to quickly build up charge on the electrode, which may steer electrode potential into an unsafe range as stimulation continues. **(b)** Charge-balanced biphasic stimulation waveforms use an additional anodic phase to balance the introduced charge. Ideally, the charge introduced in the cathodic phase is entirely cancelled out by the anodic phase, but due to (nonlinear) charge storage mechanisms in the membrane, this does not happen. Charge-imbalanced biphasic stimulation features a cathodic and anodic phase of differing length and magnitude, so as to make the remnant voltage across the electrodes as small as possible.

In the case of batteries for pacemakers, but also in the case of having an external power source, the only power considered useful is the power absorbed by the nerve tissue for stimulation. A total power efficiency can then be defined as:

$$\eta_{\text{stim}} = \frac{P_{\text{tis}}}{P_{\text{sup}}}, \tag{1.22}$$

where P_{tis} is the power that specifically is absorbed by the neural tissue, and P_{sup} is the maximum power the supply can deliver to the load. This efficiency determines the amount of power lost to additional circuitry, but also the power lost to heat generation from the use of electrical energy in the circuit. Continuously operating a high-power implant poses a risk of chronic tissue inflammation and damage, which limits the amount and length of stimulation pulses used in neuromodulation [48].

1.2.3 Charge balancing

Passive charge balancing techniques

Passive charge balancing is a viable method to get rid of the excess charge on electrodes, albeit uncontrolled [49]. An implementation may feature the addition of a blocking capacitor in the output current path, with a switch and resistor added in parallel, to discharge the tissue after a stimulation pulse.

Another approach is the shorting of electrodes by means of a dissipation circuit in parallel to the electrode output. This method requires a certain amount of time to pass for charges to fully equalize, determined by the time constant of the electrode-tissue interface [50]. Consequently, it is likely that an active form of charge balancing is required for stimulators that are more (semi-)continuous in nature, to handle excess charge buildup over longer stimulation periods.

Active charge balancing techniques

Active charge balancing techniques often involve measuring the residual voltage across the electrodes by sampling the electrode voltage with respect to tissue ground when there is no current flow, and then compensating for the offset by injecting correcting currents to eliminate the potential difference [50]. Often-used techniques include:

- **Extending the anodic phase of stimulation:** The anodic phase of stimulation is extended until the remnant offset voltage across the electrodes is within a certain predefined safe-zone [51]. This approach can be readily adopted by standard biphasic stimulators, as it only requires some small digital circuit modifications.

- **Pulse insertion:** After the main cathodic and anodic pulses, a few short-duration pulses with an opposite polarity to the remnant offset voltage are inserted until the potential difference returns to safe values [51]. Based on the severity of the remnant voltage offset, the amount of inserted pulses is dynamically changed to match the situation.
- **Offset regulation:** The continuous (feedback-enabled) adjustment of current magnitude, such that offset is constantly accounted for. This usually involves complex digital circuitry to take periodic measurements of the remnant offset voltage and adjust the pulse generation magnitudes dynamically. Recent implementations of offset regulation demonstrate that residual offsets could be kept below $\pm 12\,\mathrm{mV}$ for a broad range of input frequencies [52], which is far below the usual $\pm 50\,\mathrm{mV}$ safety window [53].

1.3 Stimulator output stages and power supply regulation

Of particular interest to the contents of this report is the neural stimulator output stage. An output stage for neural stimulation can be achieved in various ways, which will be covered in this section, along with a discussion on how energy- and power-efficient neurostimulation can be achieved through deliberate design of a current-mode stimulator, choice of input stimulation waveform and power supply regulation.

1.3.1 Modes of stimulation

Neural stimulators can choose to stimulate the nerve tissue using three different so-called 'modes' of the output quantity: voltage-, current- or charge-mode stimulation. In voltage-mode stimulation (VMS), the output quantity is a load voltage (shown in Fig. 1.13). This causes the resulting current, and thus the injected charge, to be entirely dependent on the electrode-tissue impedance. As the electrode-tissue impedance varies significantly, the charge delivered to the tissue in turn also changes uncontrollably. This can cause excessive charge accumulation, resulting in unsafe offset voltages on the electrodes that could damage nerve tissue.

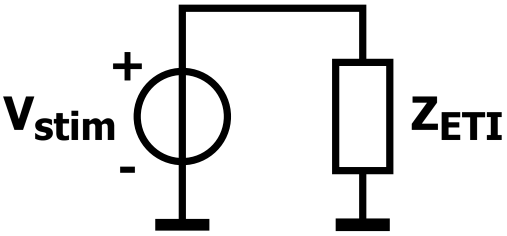

Figure 1.13: Voltage-mode stimulation (VMS) uses an output voltage as its mode of stimulation. A demerit is that the stimulation current will be entirely dependent on load impedance, causing the introduced charge to be rather uncontrolled.

In contrast, the often-used current-mode stimulation (CMS) (shown in Fig. 1.14) is much more controlled, as such a stimulator drives a fixed current through the tissue which is directly related to the amount of charge added to the tissue, regardless of the impedance. When the pulse length is accurately known, the added charge can be calculated by integration. This method therefore hinges on the complex design of accurate transadmittance or current amplifiers to provide precise control over the injected charge that is critical for safe stimulation.

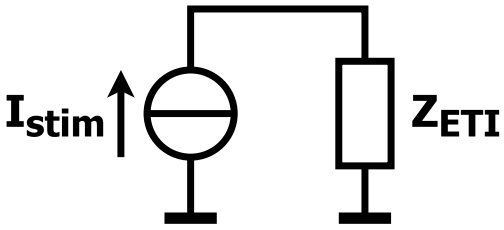

Figure 1.14: Current-mode stimulation (CMS) uses an output stimulation current as its mode of stimulation. CMS-based systems are by far the most common.

The last alternative is charge-mode stimulation (as shown in Fig. 1.15), which typically involves charging a capacitor to a known charge value, and consequently letting the capacitor discharge into the tissue [54]. This method is by far the most controlled method of stimulation, but it will often have to deal with switching losses related to imperfect switching during charge and discharge cycles. Current ripple does not matter much for the intended safety of the stimulation output, as the injected charge is entirely controlled. However, charging and discharging of the capacitor does need to happen at much higher frequencies than the targeted stimulation waveform frequency. In practice, CMS is the most often used method for stimulation of nerve tissue. In view of this fact, the following analysis will only cover the design of CMS output stages.

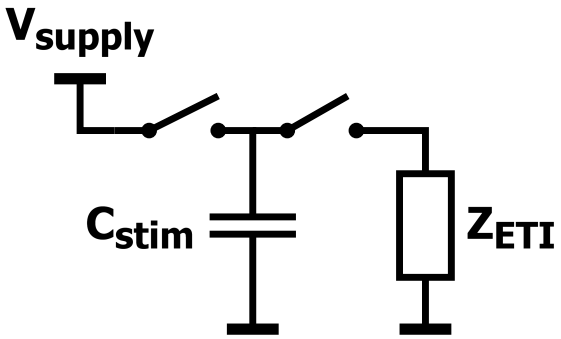

Figure 1.15: Charge-mode stimulation (ChMS) intermittently stores a charge on a capacitor, and uses the stored charge to stimulate the tissue. This method of stimulation is still relatively new.

1.3.2 Relevance of stimulation waveform shape and power supply regulation

Energy efficiency of the type of waveform used in stimulation has been a popular topic among biomedical engineers, with different waveform patterns being tested for the energy efficiency of nerve cell stimulation. A waveform that more easily generates action potentials in the neuron, for similar amplitude and frequency, is considered more biologically energy efficient. Many waveforms have been tested previously, such as ramp, triangular, rising, decaying exponential, and truncated Gaussian-like waveforms [55–58]. However, most of the reported waveform energy efficiency calculations do not account for energy efficiency in the electrical domain; for the energy consumed in the generation of such a waveform.

Additionally, the voltage supply of a current mode stimulator output stage must be able to comply with the large voltage drop that is created across the ETI for the given stimulation waveform. As such, a (non-ideal) current source that is connected to the supply (as shown in Fig. 1.16a) will introduce a voltage drop from the supply voltage V_{sup} to the electrode load voltage V_ℓ that depends on the set output current for that channel. In larger neuromodulation systems, with multiple output channels, each channel will see varying magnitudes of the ETI, thus requiring the maximum constant supply voltage of the output channels to be designed for the worst-case output channel. This means the voltage drop over current sources in channels which see smaller magnitudes of the ETI may use more power than strictly required for the current output of that channel, as the power consumed by the introduced overhead is either lost or dissipated. Such losses are detrimental to power efficiency in a stimulator system, regardless of size. Thus, a regulated supply that controls the maximum supply voltage for each channel is required.

The regulated supply should be scaled such that the voltage drop on a specific channel's current source is as small as possible for the stimulation current to still provide what is needed for that particular channel. The voltage drop across the current source is then only determined by a small overhead voltage that is required for the operation of non-ideal current sources.

The benefits of scaling the supply voltage for power efficiency in the electrical domain compared to the gains of using an efficient pulse shape from a biological perspective have been compared previously [59]. The main conclusions drawn from previous work are that rectangular pulse shapes are most biologically and electrically efficient if a constant voltage supply is used. When the voltage supply is entirely adiabetic, meaning no power is lost to the voltage drop on the current source, all other pulse shapes that were tested (Gaussian, half-sine, triangular, ramp-up and ramp-down pulses) could outperform square waves in efficiency, with Gaussian waves being most efficient. However, implementing a channel specific, adiabetic power supply is difficult to achieve in reality, requiring more circuitry, area and power consumption than is required with a constant voltage supply.

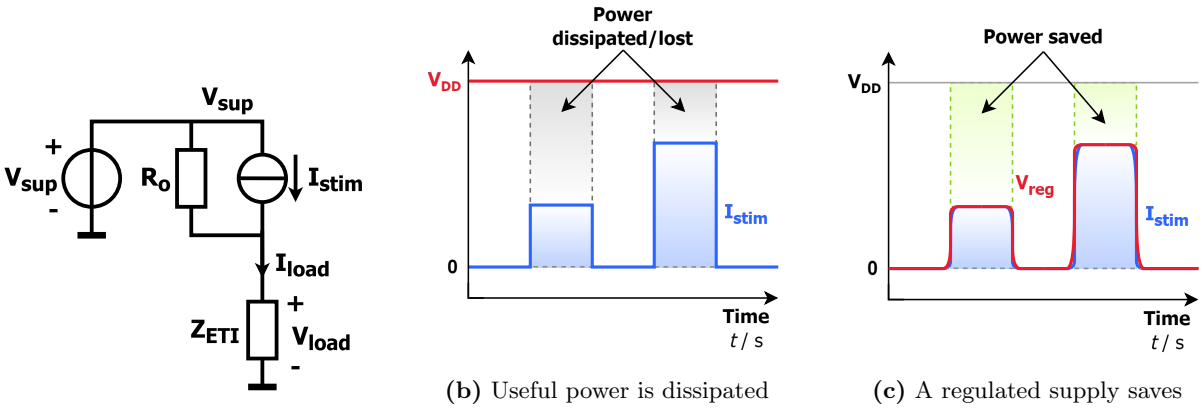

(a) A current-mode stimulator output stage.

(b) Useful power is dissipated by using a constant supply voltage.

(c) A regulated supply saves power by dynamically setting a supply voltage.

Figure 1.16: **(a)** A CMS output stage consists of a non-ideal current source with output resistance R_{out}. The load voltage is a consequence of the ETI impedance, which varies greatly. **(b)** When a constant supply voltage is used, power could be lost due to the incurred overhead when output stages are designed for the worst-case output channel. **(c)** A regulated power supply adjusts its value to the demand created by the load current, only dissipating the power that is needed for functional operation of an output channel.

Thus, the idea of stepped voltage scaling is introduced, which requires the implementation of multiple supply rails to approach the efficiencies an adiabetic supply could achieve; the more supply rails are added, the more energy is saved. However, from the results it is concluded that the (arduous) implementation of six supply rails for Gaussian pulses, only saves 4.4 % of total power dissipated compared to rectangular pulses. Additionally it is mentioned that, on the biological side, rectangular pulses show the lowest charge threshold for any given threshold current, indicating better biological energy performance compared to any other pulse shape. Considering the changes in time constant of Z_ℓ, all pulse shapes would perform worse than the rectangular pulses, and the effect is more clear for smaller time constants of the ETI.

Complications regarding dynamic power supply implementations for current mode stimulation

In literature, dynamically regulated power supplies for current mode stimulators are presented as in Fig. 1.17 [60–63]. A dynamic voltage regulator adjusts the amount of voltage on the supply by charging an output capacitor to the required value, or in some cases of buck/boost conversion, by charging an inductor to provide the voltage output.

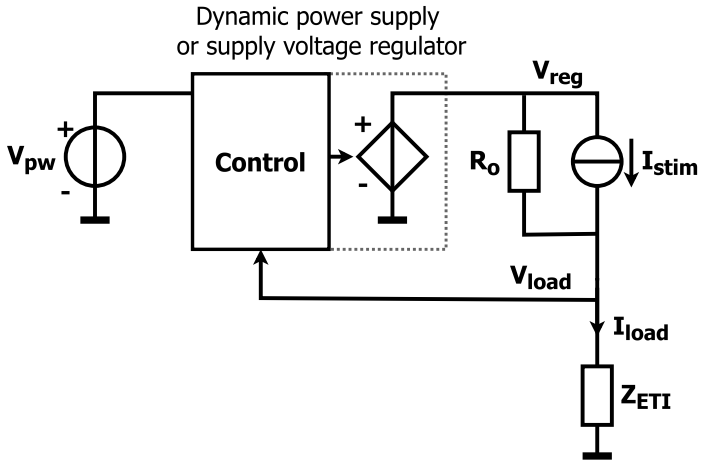

Figure 1.17: Dynamic power supplies, or supply voltage regulators, use feedback to set the appropriate supply magnitude. Feedback and control differ between implementations, but generally always draw from some external supply V_{pw}. In the analysis of power efficiency, the power transfer from V_{pw} to V_{dyn} is rarely considered.

The circuits that are implemented to control the voltage supply on the output stage are implemented in a way that ensures the regulated output stage power efficiency η_{dyn}, which is then defined as:

$$\eta_{\mathrm{dyn}} = \frac{\mathrm{P}_\ell}{\mathrm{P}_{\mathrm{dyn}}}, \tag{1.23}$$

where the the maximum available power $\mathrm{P}_{\mathrm{dyn}}$ is matched to the power through the load P_ℓ, such that $\mathrm{P}_{\mathrm{dyn}} = \mathrm{P}_\ell + \epsilon_{\mathrm{dyn}}$, with ϵ_{dyn} the difference between the provided surplus of dynamic supply power minus the strictly required load power. The output stage is therefore power-efficient when ϵ_{dyn} is small.

The presented circuits of [60–63] however ignore that the original power source that 'tops-off' output capacitors, or charges the inductor in buck/boost converters, is another unregulated voltage supply V_{pw}; the maximum available power of the regulated supply $\mathrm{P}_{\mathrm{reg}}$ is limited by the maximum available power P_{pw} of the original unregulated power supply. The power efficiency of the original unregulated power supply to the dynamic voltage supply is therefore:

$$\eta_{\mathrm{pw}} = \frac{\mathrm{P}_{\mathrm{dyn}}}{\mathrm{P}_{\mathrm{pw}}}, \tag{1.24}$$

and the total power efficiency η_{tot}, of the original power source to the load, can then be found by a cascading of the two efficiencies:

$$\eta_{\mathrm{tot}} = \eta_{\mathrm{pw}} \cdot \eta_{\mathrm{dyn}} = \frac{\mathrm{P}_{\mathrm{dyn}}}{\mathrm{P}_{\mathrm{pw}}} \frac{\mathrm{P}_\ell}{\mathrm{P}_{\mathrm{dyn}}} = \frac{\mathrm{P}_\ell}{\mathrm{P}_{\mathrm{pw}}}. \tag{1.25}$$

In other words, the maximum available power that the dynamic power supply can draw from P_{pw} is exactly equal to P_{pw}. Thus, these circuits are not more power-efficient than a system that is directly connected to V_{pw}, and only present part of the solution.

Regulation of the original power source

The problem of dynamic supply regulation can be solved by regulating the original power supply, instead of deriving a supply voltage from another unregulated supply. This can be achieved by deriving the regulated supply voltage from a feedback quantity from the output stage circuit. The load voltage V_ℓ is directly related to the load power P_ℓ, and is thus fed back to the dynamic supply regulator, which should account for a small overhead voltage $\mathrm{V}_{\mathrm{overhead}}$ needed for biasing of non-ideal current sources. The regulated supply voltage is therefore:

$$\mathrm{V}_{\mathrm{reg}} = \mathrm{V}_\ell + \mathrm{V}_{\mathrm{overhead}}. \tag{1.26}$$

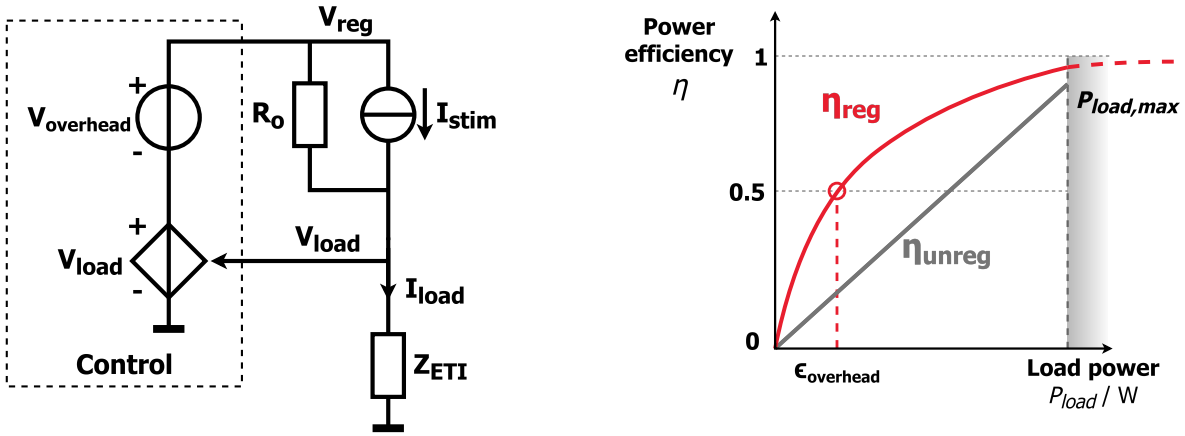

(a) Suggested regulated power supply.

(b) Efficiency scaling with load power.

Figure 1.18: **(a)** The suggested feedback for power supply regulation provides a copy of the circuit load voltage to control, which then adds a set overhead voltage to ensure the circuit stays functional. **(b)** Power efficiency scales with load power. If a constant unregulated supply is used, power efficiency shows a linear relationship. When the power supply is regulated, power efficiency is increased, depending on the added overhead.

The total power efficiency is then decided by only the newly set regulated supply voltage, meaning it is only dependent on the introduced overhead power error $\epsilon_{\text{overhead}}$ and the consumed power by the load:

$$\eta_{\text{tot}} = \frac{P_\ell}{P_{\text{reg}}} = \frac{P_\ell}{P_\ell + \epsilon_{\text{overhead}}} = \frac{1}{1 + \frac{\epsilon_{\text{overhead}}}{P_\ell}}, \text{ with } P_\ell > 0. \tag{1.27}$$

The total power efficiency therefore follows an asymptotic trend as shown in Fig. 1.18b. The power efficiency of an output stage with unregulated power supply is also shown. When the power consumed by the load matches the power consumed by the overhead of the current source, power efficiency for the regulated supply is at 50%. This implies that, the smaller we make the overhead, the more power efficient the output stage gets for a wider range of load impedances Z_ℓ.

The suggested feedback of the load voltage V_ℓ to determine the supply voltage V_{reg} means that the designed CMS output stage (which in itself will also be implemented with feedback) will have an effect on the output stage as a whole. The overall system response in this case will be covered in Sec. 2.3.2.

1.3.3 Compliance and power efficiency of current sources for neural stimulators

Output stages that would adhere to the set specification of current-mode stimulation are ideal transadmittance or current amplifiers, that use feedback to respectively amplify either a source voltage V_s or source current I_s to set the load current I_ℓ. The design of such amplifiers is extensively covered in [64], and its relation to a current-mode stimulator will briefly be summarised in this section.

In the following, the functional model of the amplifier for output stage variants will be represented by a transmission-1 matrix (T-1 matrix) of a two-port amplifier, as shown in Fig. 1.19a. The two-port input and output relation is given by the T-1 matrix equation, which is:

$$\begin{bmatrix} V_i \\ I_i \end{bmatrix} = \begin{bmatrix} A & B \\ C & D \end{bmatrix} \begin{bmatrix} V_o \\ I_o \end{bmatrix}. \tag{1.28}$$

The A-, B-, C-, and D- parameters are the reciprocal values of various gain factors, given either the measured output voltage V_o or output current I_o of the two-port is zero:

$$A = \frac{1}{A_v} = \left.\frac{V_i}{V_o}\right|_{I_o=0}, \tag{1.29}$$

$$B = \frac{1}{A_y} = \left.\frac{V_i}{I_o}\right|_{V_o=0}, \tag{1.30}$$

$$C = \frac{1}{A_z} = \left.\frac{I_i}{V_o}\right|_{I_o=0}, \tag{1.31}$$

$$D = \frac{1}{A_i} = \left.\frac{I_i}{I_o}\right|_{V_o=0}, \tag{1.32}$$

where A_v is the voltage gain factor, A_y is the transadmittance gain factor, A_z is the transimpedance gain factor, and A_i is the current gain factor. The source voltage or current input source, and related source impedance Z_s, is connected to the input port of the two-port amplifier, of which the output port is connected to the load impedance Z_ℓ. When the gain factors are defined as in the T-1 matrix equation, the source-to-load transfer for transadmittance and current amplifiers can respectively be represented as:

$$A_y = \frac{I_\ell}{V_s} = \frac{1}{AZ_\ell + B + CZ_\ell Z_s + DZ_s}, \tag{1.33}$$

and

$$A_i = \frac{I_\ell}{I_s} = \frac{1}{A\frac{Z_\ell}{Z_s} + B\frac{1}{Z_s} + CZ_\ell + D}. \tag{1.34}$$

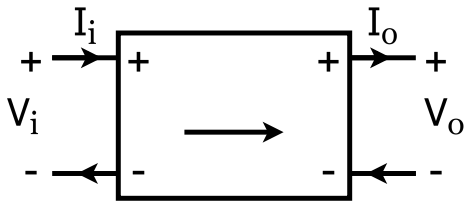

(a) Two-port model.

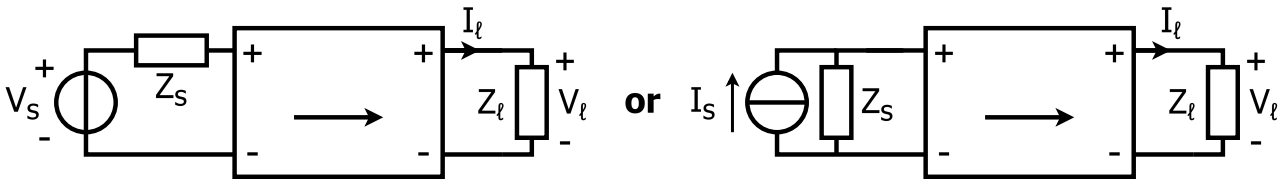

(b) Source-to-load transfers available to CMS.

Figure 1.19: (a) A two-port amplifier model consisting of an input and output port. **(b)** Either a transadmittance amplifier or current amplifier will need to be used for the output stage employing CMS.

The input and output impedance of the amplifier can similarly be defined by T-1 matrix parameters, by measuring the effect on the load impedance of a known voltage and current at the input of the amplifier for the input impedance, or by measuring the effect on the source impedance of a known voltage and current at the output of the amplifier for the output impedance (when the input is left open). The input and output impedance of the amplifier can then respectively be expressed as:

$$\mathrm{Z_i} = \frac{\mathrm{V_i}}{\mathrm{I_i}} = \frac{\mathrm{AZ_\ell + B}}{\mathrm{CZ_\ell + D}}, \tag{1.35}$$

and

$$\mathrm{Z_o} = \frac{\mathrm{V_o}}{\mathrm{I_o}} = \frac{\mathrm{DZ_s + B}}{\mathrm{CZ_s + A}}. \tag{1.36}$$

Amplifiers whose input and output impedance do not depend on respectively the load and source impedance are called unilateral. The condition for unilateral behaviour is:

$$\mathrm{AD = BC}. \tag{1.37}$$

Direct feedback transadmittance and current amplifiers

A transadmittance amplifier is an amplifier where the source voltage $\mathrm{V_s}$ is accurately amplified by a known transadmittance gain $\mathrm{A_y}$, such that the resulting load current $\mathrm{I_\ell}$ is given by:

$$\mathrm{I_\ell = A_y V_s}. \tag{1.38}$$

On the other hand, a current amplifier is an amplifier where the source current $\mathrm{I_s}$ is accurately amplified by a known current gain $\mathrm{A_i}$, such that the resulting load current $\mathrm{I_\ell}$ is given by:

$$\mathrm{I_\ell = A_i I_s}. \tag{1.39}$$

In terms of a T-1 matrix, we would only be interested in setting a value for respectively either the B-parameter or the D-parameter, as having a nonzero value for a parameter that is not part of the intended transfer means we introduce a source or load dependency, which leads to non-unilateral behaviour.

These transfers can be achieved by negative feedback with a nullor and feedback network specific to that transfer type. For direct feedback transadmittance amplifiers, direct series voltage comparison at the input port of the amplifier is required. In the case of direct feedback current amplifiers, direct parallel current comparison at the input port of the amplifier is required. Both amplifier types share the need for direct series current sensing at the output port of the amplifier, as the output quantity is the load current.

Considering that either the B-, or D-parameter needs to be fixed, the current needs to be directly sensed through the load. This requires a current sensing element in series with the signal path coming from the load (as shown in Fig. 1.20), which has consequences for the output when grounding is considered.

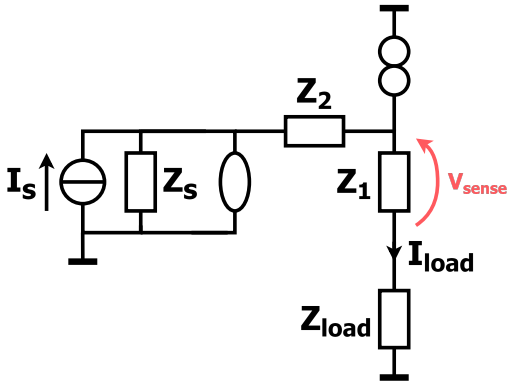

Figure 1.20: A sensing element, like a resistor, will need to be added in the signal path of a negative feedback amplifier with a current output quantity. It is preferred to have the controller output not in series with a sensing element in the signal path, to reduce power losses incurred by large voltage drops on the output source.

In the following, it will be assumed that the load impedance at the electrode Z_ℓ is always grounded, meaning either the controller output port needs to be floating, or the feedback network input port needs to be floating.

An example of a direct current sensing implementation is the addition of a passive current sensing element like a resistor. The voltage drop on the resistor is directly related to the current flowing through it, which can be used for either direct series voltage or parallel current comparison, at the input of the amplifier.

The addition of such a sensing element in the output current branch introduces an overhead, which is detrimental to power-efficiency (as was discussed in Sec. 1.3.2), though the overhead can arguably be made very small. The added noise introduced by the current sensing element affects the output quantity, but it is not of much concern when the output quantity is big relative to the noise. The most concerning issue is instead related to the value of the voltage drop across the sensing element, as differential sensing becomes difficult when the overhead drops to noise levels. This implies the power-efficiency of the circuit, and complexity of differential sensing circuitry at noise-level (and the related increased size of the circuitry) are in direct conflict based on the introduced overhead.

In the world of current-mode neural stimulators, an indirect feedback current amplifier approach is therefore preferred, even if it means the resulting amplifier is less accurate. Another preferred technique, unrelated to the feedback, is the use of current-steering digital-to-analog converters (I-DACs) as the input source. This limits the choice of output stage to current amplifiers, which use indirect feedback to define the load current.

Indirect feedback current amplifiers

Indirect feedback current amplifiers require indirect sensing of the load quantity. The related indirect copy of the output quantity is compared in parallel to the input quantity, without introducing a sensing element directly in the signal path.

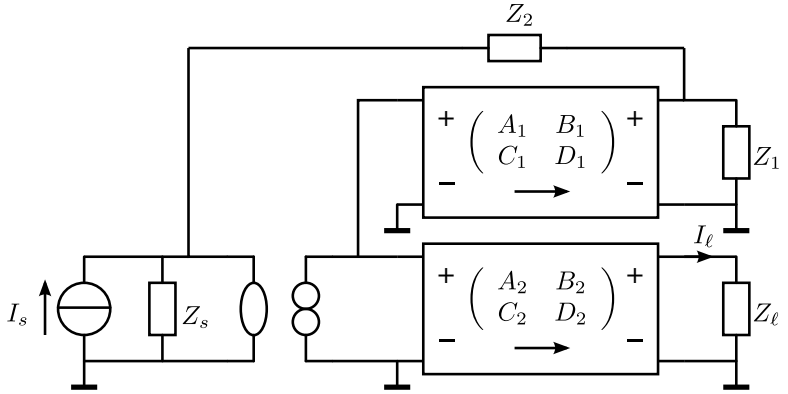

Figure 1.21: Indirect feedback amplification using indirect current sensing involves two controllers that each need to have similar T-1 matrix parameters to not introduce a load dependence (from [64]).

A model of an inverting current amplifier using indirect current sensing feedback is shown in Fig. 1.21. The amplifier features two two-ports, of which the T-1 matrix parameters are required to be exactly similar. The reason they need to be similar is shown by the source-to-load transfer, which is:

$$\frac{I_\ell}{I_s} = \frac{Z_1 + Z_2}{Z_1}\left(\frac{A_1\frac{Z_1 Z_2}{Z_1+Z_2} + B_1}{A_2 Z_\ell + B_2}\right). \tag{1.40}$$

When the T-1 matrix parameters of both two-ports are the same, and $Z_\ell = Z_1||Z_2$, the desired current gain $\frac{Z_1+Z_2}{Z_1}$ can be achieved. In reality, this is rarely the case, which means there will most likely be a load dependence when the voltage gain factors of the two-ports are not designed to be as big as possible (meaning the A-parameters of the two-ports will therefore be as small as possible). In the case that the design of the two-ports does feature large voltage gains, the C-parameter of the source-to-load transfer and related load dependence will be small, albeit nonzero.

Current mirror amplifiers

A conventional current mirror output stage is a form of indirect current sensing feedback that attempts to nullify the A-parameters and C-parameters of the two-ports in Fig. 1.21. The presence of the passive feedback network consisting of Z_1 and Z_2 is however not immediately obvious. The gain factor is obscured behind the parallel connection of an integer number of identical two-ports. The multiplicity α (or, the integer amount of parallel common-source MOSFET devices in a conventional current mirror) is the direct representation of the ideal current gain A_i:

$$A_i = \alpha. \tag{1.41}$$

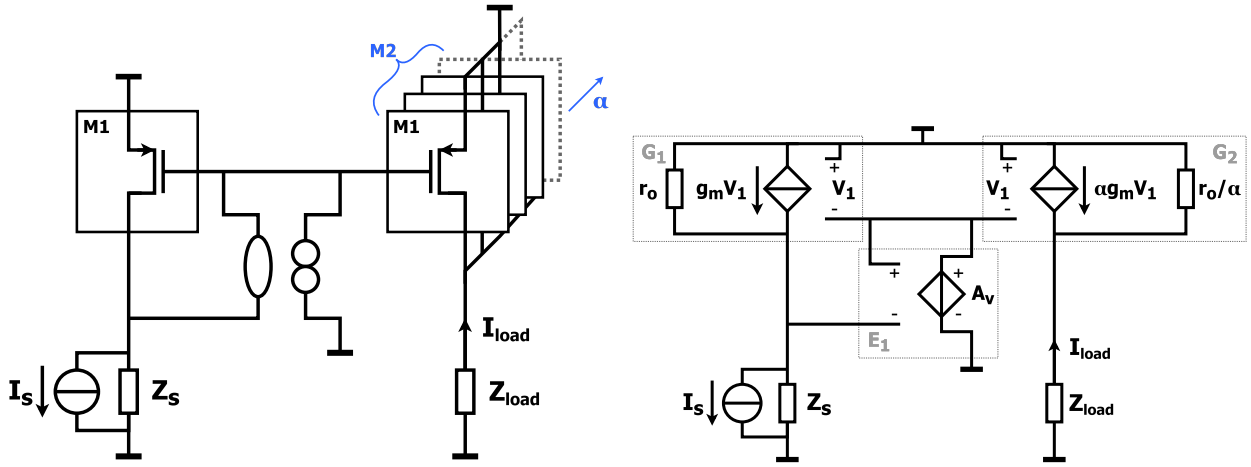

(a) Current mirror with nullor.

(b) Current mirror implemented with a basic small-signal transistor model.

Figure 1.22: **(a)** A current mirror features a large amount of identical stages in parallel. If all parallel stages are connected to the same load, the ideal gain of the output stage is the current mirror's multiplicity α. **(b)** A simple small-signal model of the CS transistors is used for initial analysis of the current mirror circuit, which features only a transconductance g_m and output resistance r_o, and does not include intrinsic MOSFET transistor capacitances like the gate-source c_{gs}, gate-drain c_{gd}, or drain-bulk c_{db} capacitances, or parameters that account for second-order effects.

For the sake of simple analysis, the (ideally biased) three-terminal common-source (CS) MOSFET devices in a current mirror are modelled as voltage-controlled current sources (VCCS), as in Fig. 1.22b. The positive input and positive output terminals of two-ports G1 and G2 are tied to the supply to model the three terminals of a CS stage in a PMOS current mirror setup. G1 is assigned a certain transconductance g_m and output resistance r_o. Given the multiplicity α of the current mirror output, G2 is modelled as a single three-terminal CS stage with an equivalent $G_m = \alpha g_m$ and $R_o = r_o/\alpha$. The nullor is replaced by a voltage-controlled voltage source (VCVS) E1 with large voltage gain A_v.

The resulting T-1 matrix parameter representation of the amplifier gain (and asymptotic gain, when A_v is big) for the source-to-load current transfer is then found to be:

$$\begin{bmatrix} A & B \\ C & D \end{bmatrix} = \begin{bmatrix} -\frac{1}{g_m r_o}(1+\frac{1}{A_v}) & -\frac{1}{\alpha g_m}(1+\frac{1}{A_v}) \\ -\frac{1}{r_o}(1+\frac{1}{g_m r_o}(1+\frac{1}{A_v})) & -\frac{1}{\alpha}\left(1+\frac{1}{g_m r_o(1+\frac{1}{A_v})}\right) \end{bmatrix} \approx \begin{bmatrix} 0 & -\frac{1}{\alpha g_m} \\ 0 & -\frac{1}{\alpha} \end{bmatrix}, \tag{1.42}$$

where E1 is taken as the loopgain reference. The loopgain of the current mirror is found to be:

$$L = -\frac{A_v(Z_s(g_m r_o + 1) + r_o)}{Z_s + r_o}. \tag{1.43}$$

In reality, E1 is often removed in favour of a single wire connection. This results in:

$$\begin{bmatrix} A & B \\ C & D \end{bmatrix} = \begin{bmatrix} -\frac{1}{g_m r_o} & -\frac{1}{\alpha g_m} \\ -\frac{1}{r_o}(1+\frac{1}{g_m r_o}) & -\frac{1}{\alpha}(1+\frac{1}{g_m r_o}) \end{bmatrix} \approx \begin{bmatrix} 0 & -\frac{1}{\alpha g_m} \\ 0 & -\frac{1}{\alpha} \end{bmatrix}. \tag{1.44}$$

The approximate values of (1.44) when r_o is big coincide with the asymptotic gain values of (1.42), meaning the current mirror will not perform any better with the added control of E1. When r_o is consistently big for given drain current variations, the transfer can approach unilateral behaviour. The total gain of the transfer is then mostly affected by the source impedance, and only approaches the ideal gain A_i if we also assume Z_s to be big:

$$\left|\frac{I_\ell}{I_s}\right| = \frac{\alpha g_m Z_s}{1 + g_m Z_s} \approx A_i, \text{ with } Z_s >> 1. \tag{1.45}$$

The input and output impedance, in case r_o is big, are then found as:

$$|Z_i| = \frac{AZ_\ell + B}{CZ_\ell + D} \approx \frac{1}{g_m}, \tag{1.46}$$

$$|Z_o| = \frac{DZ_s + B}{CZ_s + A} \approx \infty. \tag{1.47}$$

In literature there is therefore a significant focus on increasing equivalent output resistance R_o, or at least the output resistance r_o of an individual MOSFET device, as that is the only parameter that reduces the effects of the A- and C-parameters, and improves the D-parameter in the T-1 matrix parameter representation of the gain in (1.44). An increased output resistance is achieved by architectures like the cascoded current mirror, as shown in Fig. 1.23a. The cascode current mirror is also modelled like the normal current mirror, as shown in Fig. 1.23b. This is an ideal version of the cascode current mirror, where the 'bulk' connections of the MOSFET devices modelled by G1 and G2 are allowed to be connected to their source, eliminating any second-order effects (which also were not present in the modelling of the normal current mirror).

The resulting T-1 matrix parameter representation of the gain for the source-to-load transfer is given by:

$$\begin{bmatrix} A & B \\ C & D \end{bmatrix} = \begin{bmatrix} -\frac{2}{g_m r_o(g_m r_o+3)} & -\frac{2(g_m r_o+2)}{\alpha g_m(g_m r_o+3)} \\ -\frac{g_m r_o+1}{g_m r_o^2(g_m r_o+3)} & -\frac{g_m r_o(g_m r_o+3)+2}{\alpha g_m r_o(g_m r_o+3)} \end{bmatrix} \approx \begin{bmatrix} 0 & -\frac{2}{\alpha g_m} \\ 0 & -\frac{1}{\alpha} \end{bmatrix}, \tag{1.48}$$

which looks in approximation similar to (1.44), with the B-parameter about two times larger. At the same time, the A- and C-parameters are $(g_m r_o + 1)$ times smaller. The resulting parameter values of (1.44) and (1.48) show that there is a dependence on a relatively uncontrolled parameter r_o, that we would rather do without. In other words, the better solution would be to use indirect feedback that attempts to nullify the A-, B- and C- parameters, while keeping the D-parameter, without having to unnecessarily increase output resistance.

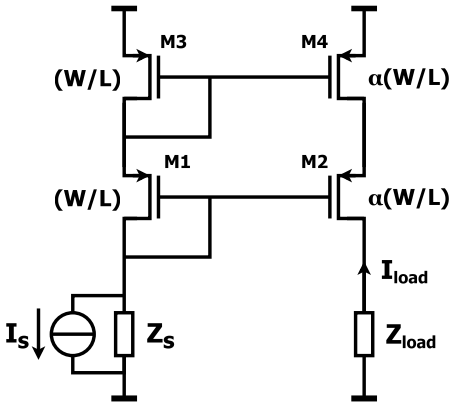

(a) Cascode current mirror.

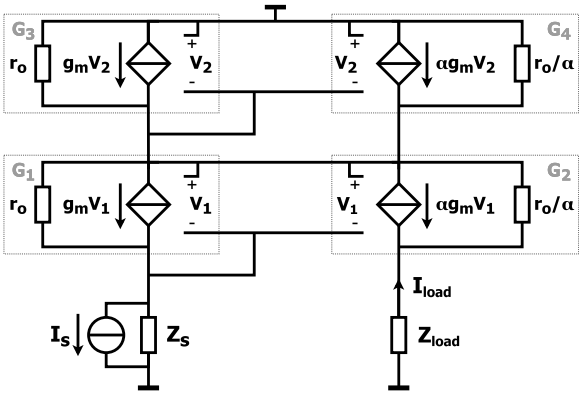

(b) Cascode current mirror implemented with a basic small-signal transistor model.

Figure 1.23: **(a)** The cascode current mirror uses a cascode transistor to increase output resistance. **(b)** The implementation of the cascode current mirror provides larger output resistance at the cost of an increase in the B-parameter in the T-1 matrix parameter representation of the gain, which has both positive and negative effects on gain accuracy.

Active current mirror amplifiers with little source dependence

In the previously shown implementations of the current mirror there will always be some source dependence, due to a dependence on output resistance and transconductance values of MOSFET devices that are difficult to control when considering large output current swing in operation. They will therefore not be able to always ensure the B-parameter is sufficiently reduced. The inverse of such amplifiers is shown in Fig. 1.24. The controller E1 now attempts to reduce the source dependence by means of feedback through the current mirror, in return for a load dependence, indicated by the value of the C-parameter.

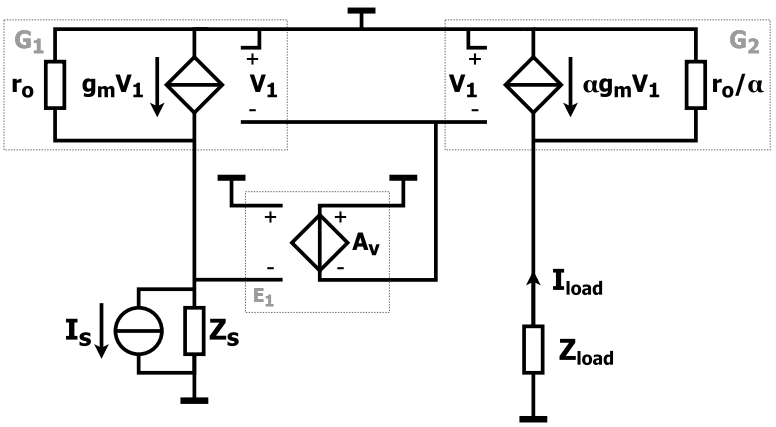

Figure 1.24: Controller E1 reduces source dependence when A_v is sufficiently high, which makes the B-parameter, from the T-1 matrix parameter representation of the gain, approach zero.

The resulting T-1 matrix parameter representation of the gain is given by:

$$\begin{bmatrix} A & B \\ C & D \end{bmatrix} = \begin{bmatrix} -\frac{1}{A_v g_m r_o} & -\frac{1}{\alpha A_v g_m} \\ -\frac{A_v g_m r_o + 1}{A_v g_m r_o^2} & \frac{1 - A_v g_m r_o}{\alpha A_v g_m r_o} \end{bmatrix} \approx \begin{bmatrix} 0 & 0 \\ -\frac{1}{r_o} & -\frac{1}{\alpha} \end{bmatrix}, \tag{1.49}$$

where E1 is taken as loopgain reference. The input- and output-impedance are then found to be:

$$|Z_i| = \frac{AZ_\ell + B}{CZ_\ell + D} \approx 0, \tag{1.50}$$

$$|Z_o| = \frac{DZ_s + B}{CZ_s + A} \approx \frac{r_o}{\alpha}. \tag{1.51}$$

Like the indirect current sensing feedback shown in Fig. 1.21, the two-ports still require appropriate matching of the individual parallelized transistor stages. If matching is assured, the total gain of the transfer is then affected by the load impedance and output resistance of the individual output transistors, and approaches the ideal gain A_i if we also assume r_o to be big:

$$\left|\frac{I_\ell}{I_s}\right| = \frac{\alpha r_o}{\alpha Z_\ell + r_o} \approx A_i, \text{ with } r_o >> \alpha Z_\ell. \tag{1.52}$$

Controlling the power spent on overhead of output current sources

The control of Fig. 1.21 is ideal when considering the implementation of a current source for indirect feedback amplifiers, but it only behaves in an ideal manner if $Z_\ell = Z_1||Z_2$. If the current mirror output resistances of the circuit in Fig. 1.24 are then required to be similarly matched to Z_ℓ for accuracy of the source-to-load transfer, it can be seen that:

$$Z_\ell \propto \alpha, \tag{1.53}$$

which implies that the multiplicity of the current mirror itself needs to be adjusted to the load for sufficient accuracy.

When considering the fact that the ETI can change significantly, the multiplicity of the current mirror will need to be adjusted on-the-fly to the sensed load impedance to ensure accuracy of the amplified input current, which is difficult to implement. Strictly speaking, the multiplicity can be kept constant by dynamically changing the input source current instead. This approach is commonly used in neural stimulator literature, where the output stage is often supported by additional circuitry such as compliance monitors and compensation current circuits, to keep the accuracy within certain acceptable bounds.

The supply regulation as discussed in Sec. 1.3.2 presents another possibility for the solution to this problem. The discussed feedback for supply regulation requires setting the supply voltage to a value that is ideally nearly identical to the load voltage, where $V_{overhead}$ would approach zero to ensure high power efficiency. This implies that the employed feedback has an intentional load dependence, as the range of the load impedance magnitude is assumed to be known to a certain degree. The supply regulation feedback sets a voltage based on the load voltage, which is modelled as in Fig. 1.25, and includes as little overhead voltage as possible.

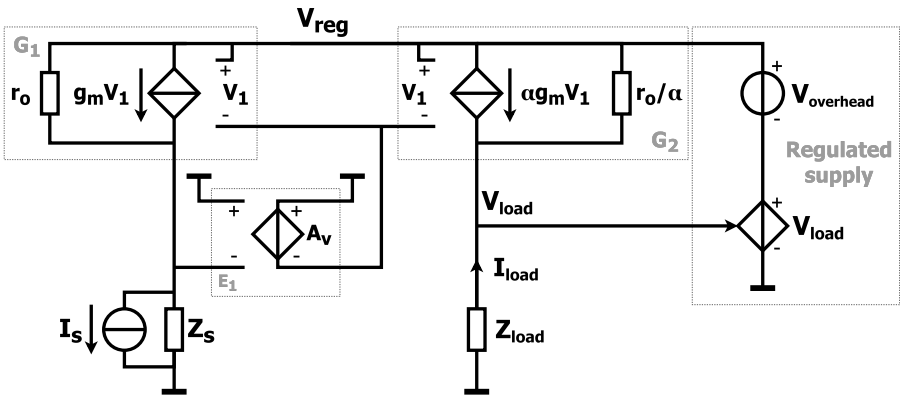

Figure 1.25: The supply regulation control adds a load dependence due to sensing the voltage on the load, which affects the system response as a whole.

The resulting T-1 matrix parameter representation of the gain is given by:

$$\begin{bmatrix} A & B \\ C & D \end{bmatrix} = \begin{bmatrix} 1 - \frac{1}{A_v g_m r_o} & -\frac{1}{\alpha A_v g_m} \\ \frac{A_v g_m r_o + 1}{A_v g_m r_o^2 (A_{reg} - 1)} & \frac{-A_v g_m r_o - 1}{\alpha A_v g_m r_o} \end{bmatrix} \approx \begin{bmatrix} 1 & 0 \\ 0 & -\frac{1}{\alpha} \end{bmatrix}, \text{ with } A_{reg} > 1. \tag{1.54}$$

The use of the discussed voltage supply regulation incurs a penalty: the circuit now directly senses the load current by measuring the load voltage, in an attempt to equalize the source voltage V_s and the load voltage V_ℓ, which fixes the A-parameter to be close to unity. The source-to-load transfer is relatively unchanged if A_{reg} is larger than one (if A_{reg} is not larger than one, the load voltage could be higher than the set supply voltage, which would mean there is a negative voltage drop on the current source as seen from the load).

The asymptotic gain is affected by both the source and load impedance, which gains more accuracy as Z_s gets larger:

$$\left|\frac{I_\ell}{I_s}\right| = \frac{\alpha Z_s}{|\alpha Z_\ell - Z_s|} \approx A_i, \text{ with } Z_s >> Z_\ell. \tag{1.55}$$

The asymptotic gain paints a poor picture of the system with supply regulation; it is, similar to the conventional current mirror, dependent on large values of Z_s, except for the fact that Z_s now needs to be much bigger than Z_ℓ. In Sec. 2.3.2 the limits and benefits of this design will be further discussed, and the ideal minimum value of Z_s will be determined based on a known magnitude range of Z_ℓ. Regardless, in the ideal case, the input and output impedance are then found to be:

$$|Z_i| = \frac{AZ_\ell + B}{CZ_\ell + D} \approx \alpha Z_\ell, \tag{1.56}$$

$$|Z_o| = \frac{DZ_s + B}{CZ_s + A} \approx \frac{Z_s}{\alpha}, \tag{1.57}$$

which is akin to transformer-like amplifier operation. Due to the penalty incurred by fixing the A-parameter, the circuit therefore does not approach unilateral behaviour, as $AD \neq BC$.

Positive feedback current mirror amplifiers

Another version of an active current mirror is shown in Fig. 1.26a. It employs positive feedback to equalize the drain voltages of M1 and M2, essentially achieving the same effect as in (1.54).

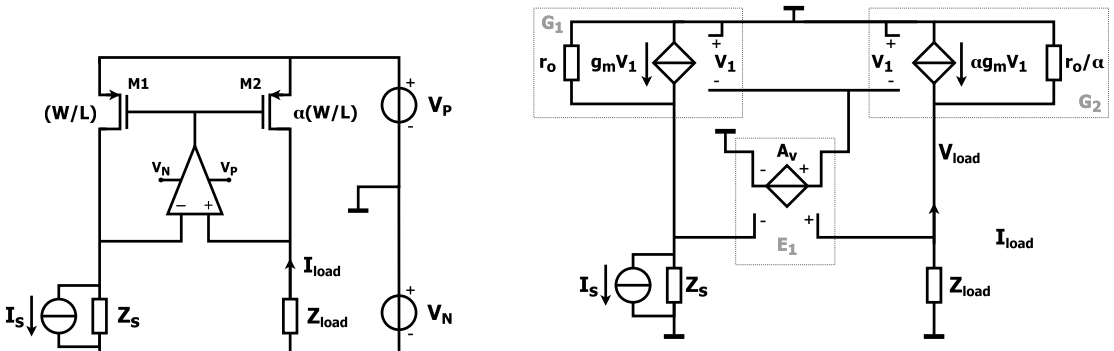

(a) A current mirror employing positive feedback.

(b) Positive feedback current mirror implemented with basic small-signal transistor models.

Figure 1.26: (a) This active current mirror circuit employs positive feedback to equalize the drain voltages of M1 and M2. **(b)** The positive feedback circuit will only be stable if the negative feedback loop is dominant over the positive one, as corrective feedback needs to account for runaway behaviour associated with positive feedback.

Positive or negative feedback is an arbitrary distinction when using nullors in the feedback design, but due to the conventional use of opamps for positive feedback current mirrors (as in Fig. 1.26a), where the input port connections matter for the dominance of the negative feedback loop, the technique will be denoted as positive feedback in the following.

The use of this circuit incurs the exact same penalty as the regulated supply version of the active current mirror in Fig. 1.25, due to directly sensing the load voltage at the output of G2. The T-1 matrix parameters of the gain can be derived as:

$$\begin{bmatrix} A & B \\ C & D \end{bmatrix} = \begin{bmatrix} 1 + \frac{1}{A_v g_m r_o} & \frac{1}{\alpha A_v g_m} \\ \frac{1}{A_v g_m r_o^2} & \frac{1 - A_v g_m r_o}{\alpha A_v g_m r_o} \end{bmatrix} \approx \begin{bmatrix} 1 & 0 \\ 0 & -\frac{1}{\alpha} \end{bmatrix}, \tag{1.58}$$

with E1 as the loopgain reference. Aside from the fact that this version of the circuit also does not approach unilateral behaviour, special care has to be taken into ensuring the positive feedback loop does not dominate over the negative feedback loop. Considering the circuit's operation with the ETI as the load impedance, the compliance range is significantly more limited than this initial analysis might suggest, due to instability brought about by initial conditions.

1.4 Spatially selective vagus nerve stimulation

Aside from considerations regarding the output stage of a neural stimulator, a particular focus of this report is the spatial selectivity of vagus nerve stimulation, which will be briefly covered in the following.

1.4.1 Conventional vagus nerve stimulation

Vagus nerve stimulation (VNS) is an established neuromodulation method for the treatment of epilepsy, heart arrhythmia, asthma and COPD [65, 66]. Some of the currently fully-implanted VNS devices stimulate the vagus nerve by generating an electric field between contact points of helical (cuff) electrodes wrapped around the nerve, as illustrated in Fig. 1.27. Neurons in the vagus nerve are typically stimulated at stimulation frequencies of (10 to 50)Hz, as threshold currents for AP generation are lowest in this bandwidth [67].

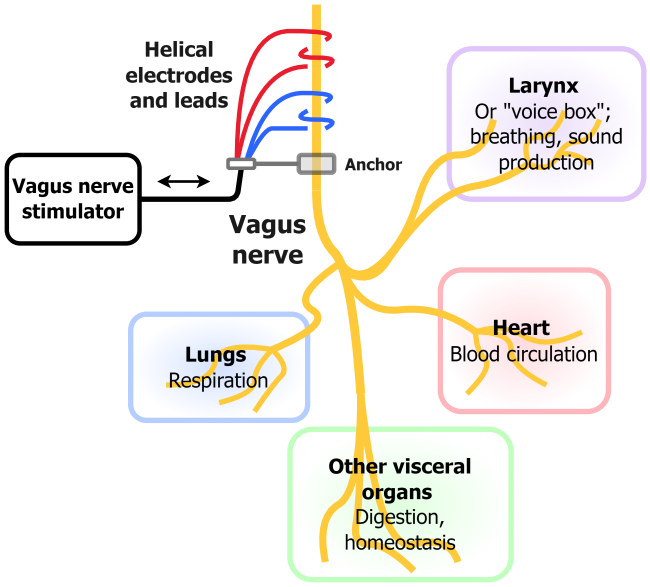

Figure 1.27: The vagus nerve is conventionally stimulated using helical electrodes, which are anchored on the vagus nerve. The vagus nerve reaches various visceral organs, which maintain homeostasis in the body. Many of the efferent nerve fascicles reach the larynx, which controls breathing and vocal sound production.

This method of stimulation has significant benefits for the treatment of vital organ dysfunctions, such as those affecting the heart and lungs [66, 68]. Treated patients have however reported many negative side effects to this technique, such as: hoarseness, loss of voice, throat and chest pain, dyspnea, paraesthesia, indigestion, and vomiting [69, 70], which are partially tied to the erroneous activity of laryngeal branches of the vagus nerve, which innervate nearly all of the muscles of the larynx.

Complications regarding conventional VNS

The side-effects related to conventional VNS are largely caused by the indiscriminate stimulation of off-target nerve fascicles, which affects organs in the parasympathetic nervous system. The parasympathetic nervous system is the part of the nervous system that maintains the normal state and activity of visceral organs, like the heart, lungs, liver, and intestines, to name a few.

The nerve fascicles in the vagus nerve consist mostly of afferent, but also efferent nerve fascicles, of which the latter mostly control muscles in the larynx [68]. By selectively stimulating individual fascicles of the vagus nerve, the side-effects of conventional VNS can be reduced [71], and organ-specific responses can be elicited [72]. Later work on the selective stimulation of vagus nerve fascicles further posits the somatotopic arrangement of vagal nerve cells [73, 74], meaning each of the (afferent) vagus nerve fascicles is relevant to a specific organ in the body. This implies that spatially selective stimulator devices could provide only the targeted organ with the intended neuromodulation treatment, given they had a way to apply the electric field at specific points in the cross section of the vagus nerve. Spatial selectivity is often implemented as specific electrode arrangements that increase in number and density around the nerve, which increases the selectivity, or 'spatial resolution', of stimulation at the periphery of the nerve, in the direct vicinity of the epineurium.

However, due to the posited somatotopic arrangement of nerve fascicles, and the reduced side-effects of spatially selective neurostimulation, it would be more preferred to instead provide stimulation that can enter deeper structures within the nerve. This presents a problem of conflicting requirements for the system design of spatially selective vagus nerve stimulators; for the benefit of patient safety, electrodes should not be directly inserted into the specific nerve fascicle, which consequently reduces spatial selectivity.

1.4.2 Temporal interference stimulation

One of the approaches to achieve spatial selectivity without directly inserting electrodes inside the nerve, is temporal interference stimulation (TIS) [75]. The stimulation method uses two or more sinusoidal electric fields at frequencies in the kilohertz-range in such a way, that each field has a slightly different frequency. The posited idea claims that the induced electric fields travel through nerve tissue and interfere. This interference is an amplitude modulation that creates a spatially localised stimulation waveform at the focal point of the interference, as shown in Fig. 1.28. This amplitude modulated waveform is said to be capable of eliciting action potentials in nerve cells due to the creation of intermodulation products at the difference frequency of the given input waveforms. The stimulation has previously been shown to indeed be spatially selective [76], however, regardless of its ability to provide deep, targeted stimulation, the electrophysiological mechanisms behind this interaction, and the resulting stimulation of neurons under influence of the intermodulation products is still insufficiently understood.

In the prevailing mechanistic model of TIS, the intrinsic LPF-like behaviour of neurons is considered an essential part of the stimulation method. The model relies on the superposition of two electric fields with nearly identical frequencies to produce an amplitude modulated waveform. This amplitude modulation is then envelope traced by the LPF-like properties of the neuron to produce a waveform with slowly varying intensity that can stimulate the neuron, at the focal point of interference. However, this simplifies several critical aspects relating to the inherent nonlinearity of neurons, the frequency spectrum of the input stimulation waveforms, and the posited envelope detector-like behaviour.

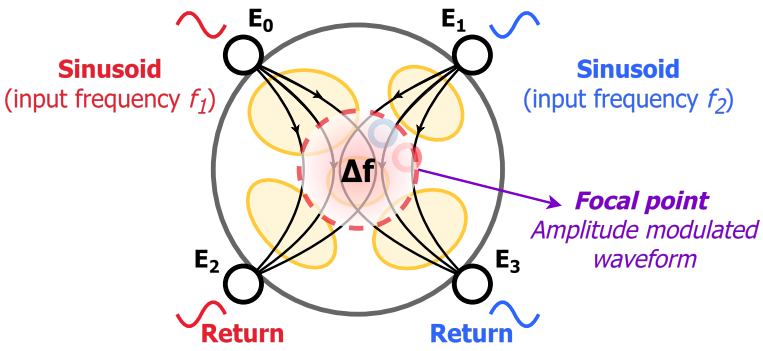

Figure 1.28: A cross section of the vagus nerve and surrounding electrodes $E_{0–3}$ is shown. The superposition of electric fields with waveform frequencies f_1 and f_2 create an amplitude modulated waveform at the focal point of interference, modulated at the difference frequency $\Delta f = f_1 - f_2$.

Additionally, because TIS requires the modulation of multiple high-frequency carriers, the power of the intermodulation product that provides the low frequency stimulation is smaller than the power of the input waveforms at higher frequencies. Not to mention the paradoxical use of such high frequencies, which conventionally cause neural inhibition. If inhibition is present, stimulation current requires higher magnitudes to generate an AP in a given amount time, thus requiring more power to stimulate the neuron.

Consequently, a fundamental trade-off of the technique is a higher power consumption in exchange for improved spatial selectivity. As a result, power-efficiency becomes a central focus in the design of a TIS-based stimulator. Power-efficiency is critical to the safety and longevity of fully-implanted neurostimulators in general, but it is even more significant in the case of TIS. Thus, if there is no clear benefit to spatial selectivity — as in cases where the side-effects of conventional VNS are not as severe, or when the patient comfort is otherwise acceptable — then it is not in the patient's best interest to choose for temporal interference-based neurostimulators. Therefore, in the following discussion, it is assumed that the spatial selectivity provided by TIS is medically justified and necessary.

Chapter 2

Temporal interference stimulation: underlying electrophysiological processes and stimulator system design

This chapter will partly cover the electrophysiological modelling underpinning temporal interference stimulation, with a focus on presenting issues relating to the conventional modelling and measured observations of neuron responses under influence of interfering electric fields. Afterward, general principles of temporal interference-based stimulator designs are outlined, and existing system solutions in literature are stripped to the bare minimum of viable operation for TIS conditions. Afterwards, a proposed system architecture and output stage design for a power-efficient temporal interference-based vagus nerve stimulator system is presented. The chapter ends by stating the research aim, framing the analytical work that follows.

2.1 Conventional mechanistic model of neural stimulation using TIS

2.1.1 Conventional superposition model

The assumed mechanistic model behind TIS is an amplitude modulation of two electric fields at different frequencies f_1 and f_2, separated by a small difference in frequency Δf. Conventionally, $f_1 = 2.01\,\mathrm{kHz}$ and $f_2 = 2\,\mathrm{kHz}$, which creates a pulsating intensity at a beat frequency $\Delta f = f_1 - f_2 = 10\,\mathrm{Hz}$. To show the origin of the beat frequency, the electric field inputs are described as lossless, continuous harmonic, one-dimensional wave functions:

$$y(x,t) = A\cos\left(\frac{2\pi t}{T} - \frac{2\pi x}{\lambda} + \phi_{ref}\right) = A\cos(\omega t - px + \phi_{ref}), \tag{2.1}$$

where the time period T in seconds is the reciprocal of the frequency f in Hertz, x is the position along the direction of propagation in meters, A is the amplitude in volt per meter, λ is the wave length in meters, ϕ_{ref} is the reference phase in radians and p is the phase constant (or wave number) of the wave per meter.

Note that, in any physical case, be it two- or three-dimensional, when the electric fields are further removed from the focal point, the modulation depth varies based on the wavelength λ and propagation velocity ω/p in the intracellular medium of the nerve. Given a lower modulation depth, nerve cell sensitivity is decreased, as kilohertz-range frequencies are used as the constituents for the amplitude modulation. Additionally, when the stimulation waveform is further removed from the input source, attenuation caused by the lossy intracellular medium decreases stimulation amplitude.

Regardless, in the following, only the static focal point of interference will be considered, which is set at the point $x = 0$ along the direction of propagation. The function $y(x,t)$ becomes independent of x when evaluated at $x = 0$:

$$y(0,t) := \widetilde{y}(t). \tag{2.2}$$

For the superposition of the waveforms, the sum and difference frequencies are defined as:

$$\Sigma f = f_1 + f_2, \tag{2.3}$$

$$\Delta f = f_1 - f_2, \tag{2.4}$$

and the corresponding angular frequencies are defined as:

$$\Sigma\omega = \omega_1 + \omega_2 = 2\pi\Sigma f, \tag{2.5}$$

$$\Delta\omega = \omega_1 - \omega_2 = 2\pi\Delta f, \tag{2.6}$$

where rewriting equations (2.5) and (2.6) yields the following equivalent definitions of ω_1 and ω_2:

$$\omega_1 = \frac{1}{2}(\Sigma\omega + \Delta\omega), \tag{2.7}$$

$$\omega_2 = \frac{1}{2}(\Sigma\omega - \Delta\omega). \tag{2.8}$$

If both input waveforms can be assumed to have the same reference phase $\phi_{ref} = 0$, the superposition of the two input waveforms can be expressed as the output waveform $\widetilde{\Phi}(t)$:

$$\widetilde{\Phi}(t) = \widetilde{y}_1(t) + \widetilde{y}_2(t) = A_1 \cos(\omega_1 t) + A_2 \cos(\omega_2 t). \tag{2.9}$$

Filling (2.7) and (2.8) into (2.9) yields:

$$\Rightarrow \widetilde{\Phi}(t) \ = A_1 \cos\left(\frac{1}{2}(\Sigma\omega + \Delta\omega)t\right) + A_2 \cos\left(\frac{1}{2}(\Sigma\omega - \Delta\omega)t\right). \tag{2.10}$$

Then, using trigonometric identities, we can further derive (2.10) to be equivalent to:

$$\Rightarrow \widetilde{\Phi}(t) \ = (A_1 + A_2)\cos\left(\frac{1}{2}\Sigma\omega t\right)\cos\left(\frac{1}{2}\Delta\omega t\right) + (A_1 - A_2)\sin\left(\frac{1}{2}\Sigma\omega t\right)\sin\left(\frac{1}{2}\Delta\omega t\right). \tag{2.11}$$

Assuming the stimulation amplitudes are equal, such that $A_1 = A_2 = A$, we finally arrive at the following definition of the amplitude modulated output waveform at the focal point:

$$\widetilde{\Phi}(t) \ = 2A \cos\left(\frac{1}{2}\Sigma\omega t\right)\cos\left(\frac{1}{2}\Delta\omega t\right), \tag{2.12}$$

which shows the multiplicative relationship between the two signals, where the high frequency carrier signal at $\frac{1}{2}\Sigma\omega$ (or, the average input frequency) is under influence of the modulation signal, or half the beat frequency, at $\frac{1}{2}\Delta\omega$.

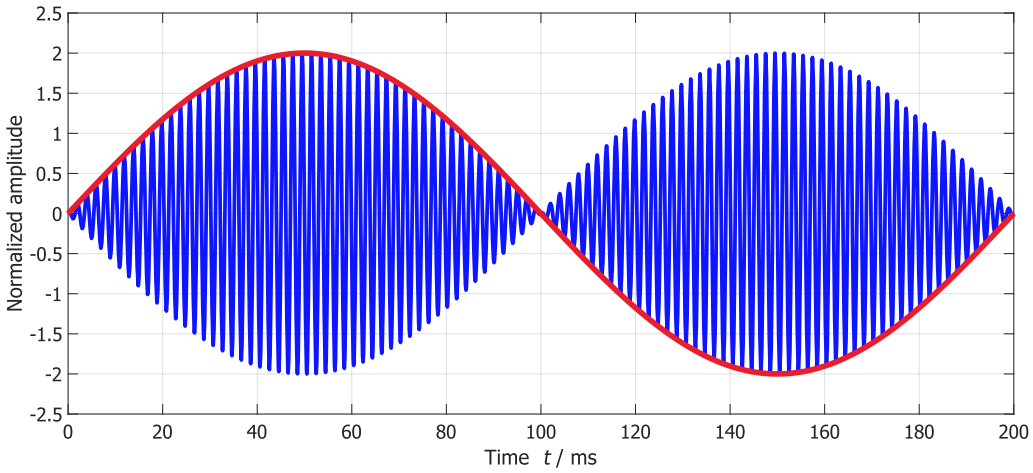

Figure 2.1: The superposition of two waveforms with equal amplitude A, and nearly identical frequencies f_1 and f_2 create an amplitude modulated waveform when superimposed. The intensity of this waveform changes at the rate of the beat frequency Δf, with the oscillation of both waveforms at the average of its constituent input frequencies, or half the sum frequency, $\frac{1}{2}\Sigma f$.

The intrinsic LPF-like behaviour of the nerve cell is posited to trace the envelope of the amplitude modulation at a frequency of 10 Hz [75], as shown in Fig. 2.1. This generates a stimulation waveform at the focal point of interference that is able to more easily generate action potentials due to the nerve cell's increased sensitivity to lower stimulation frequencies.

2.1.2 The conventional superposition model does not match observations of neuron responses under influence of TIS

The spectral components of a superimposed stimulation waveform are simply the input frequencies as they are; no beat frequency or average frequency is present in the magnitude spectrum of the focal point in the previous model, if it were to be measured. This contradicts the statements made earlier on the benefits of TIS; at the focal point of stimulation, a varying intensity at the beat frequency Δf might be present, but the nerve cell perceives the stimulation waveform as singular frequencies f_1 and f_2.

This would make stimulation no better than conventional kilohertz-range stimulation methods, or entirely cause conduction block as a consequence of the use of such high stimulation frequencies. These supposed effects were recently (partially) confirmed, where modulated TIS and unmodulated sine carrier frequencies in the range of kilohertz showed similar strength-frequency dependence [77]. However, the overshadowed part of the presented conclusions of [77] is the opportunity to move the focal point of amplitude modulation by means of current steering.

Similarly, in [78], it was found that the supposed envelope extraction of TIS is not the underlying mechanism that makes the stimulation method work, or is even present in the first place. According to the authors, the method of stimulation can allow for the creation of spatially distinct regions where varying degrees of modulated, unmodulated, or conduction blocking waveforms are present.

In early work on the electrophysiological properties of neurons it was found that the ionic conductances of a nerve cell also provide autorhythmic electrical oscillatory properties to it [79]. This showed that underlying stimulation input/output relationships could, in the case of mammalian neurons in the central nervous system, be interpreted as nonlinear. The nonlinear oscillatory activity of neurons has further been observed in the electroreceptors of paddlefish in [80], where two oscillators are used to stimulate a hair cell-afferent sensory receptor. The presented results of [80] indicate that products of frequency mixing operations within the neuron exist on the measured frequency range; multiples of the input frequencies, sum and difference frequencies, and other spectral mixing components are present, which decrease or increase in magnitude as the amplitude of input waveforms is changed. Slightly before this work, in [81], a model of the frequency mixing phenomenon is presented and confirmed, but it largely rejects frequency mixing products outside of the difference and sum frequencies, for lack of a better understanding of the nonlinear stimulation mechanisms of the neuron.

In [82], an attempt was made at proving the frequency mixing phenomenon by deductively reasoning that three-way phase relationships are measurable when nonlinear frequency mixing phenomena occur spontaneously. The three-way phase relationships consist of a unique sum of the magnitudes of three frequency components, where an input frequency and its second harmonic are not both present in the triplet. The distinction between artificially induced or spontaneously emerging frequency mixing products had not been made yet in literature thus far, prompting the authors to conduct the study. They also cautiously expected the mixing phenomenon to emerge at individual neuron level.

This expectation was later confirmed, as TIS was tested for the presence of such frequency mixing components in the frequency spectrum of *ex-vivo* and *in-vivo* neural cell measurements in rodents, and through EEG measurements of the human brain [83]. Additionally, it was shown through pharmacological blocking of ion channels that frequency mixing phenomena could be selectively suppressed, indicating that the origin of the measured spectral components are the voltage-gated ion channels in the neuron membrane.

2.2 Temporal interference stimulator output stages

2.2.1 Existing system implementations for TIS

In the original work that posited the TIS-method, a stimulator circuit employing sinusoidal TIS is shown [75]. The presented implementation only needed to show the function of using interfering fields to create stimulation, not its feasibility for integrated circuits. Therefore, the implementation is simplified to the use of ideal sources, transfers and control. In the presented isolated channel output stage of [75], a current source J1 at electrode 1A generates the stimulation pulse as a sourcing current, which returns to electrode 1B that sinks the exact same current through the paired second current source J2, as illustrated in Fig. 2.2. The order is then flipped in the negative phase of the stimulation waveform, where source J1 sinks and source J2 sources the current.

From an electrical standpoint, this model only works when sources J1 and J2 are *exactly* the same (if we imagine some complex load impedance between the two electrodes $Z_\ell = Z_{ETI}$). If they are not the same, the node voltages at electrode 1A and electrode 1B are undefined. This is especially relevant when we consider the IC implementation of these current sources, as matching them exactly will not be feasibly implementable.

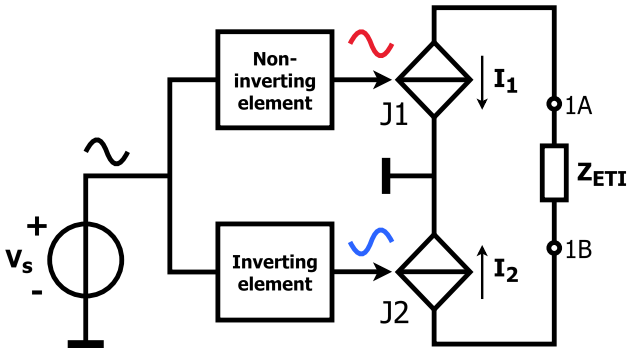

Figure 2.2: A single channel of the system employed in sinusoidal TI (adapted from [75]).

The use of the second "return" source is discussed to be for cross-talk prevention, however the issues regarding the mismatch of one such pair of current sources are not mentioned. Additionally, as this method uses two (biphasic) current sources per channel, the amount of sources will take up more area as the amount of channels increases. Increasing the amount of channels is desirable for increasing resolution, but having more biphasic sources is not ideal for area usage. Therefore, sharing current sources is crucial to reduce area costs.

A recent attempt at the integrated circuit implementation of a TIS system is provided in [84], which is illustrated in Fig. 2.3. The system uses sixteen electrodes and shares eight current sources (two per every four electrodes). This work raises some important points: small, and thus high impedance electrodes (∼kΩ) will require high voltage (HV) compliance of the output transistors connected to the ends of the electrodes, as the stimulation currents for TIS could reach up to 10 mA in pigs [66]. For example, the design uses HV-technology transistors at the output switches and a level shifter per switch to account for this.

Furthermore, the paper mentions the use of active charge balancing due to the semi-continuous nature of the stimulation method. The design therefore includes a voltage monitoring circuit that measures the residual voltage between the electrodes and a compensation circuit per electrode to periodically insert or remove some current from the main stimulation current.

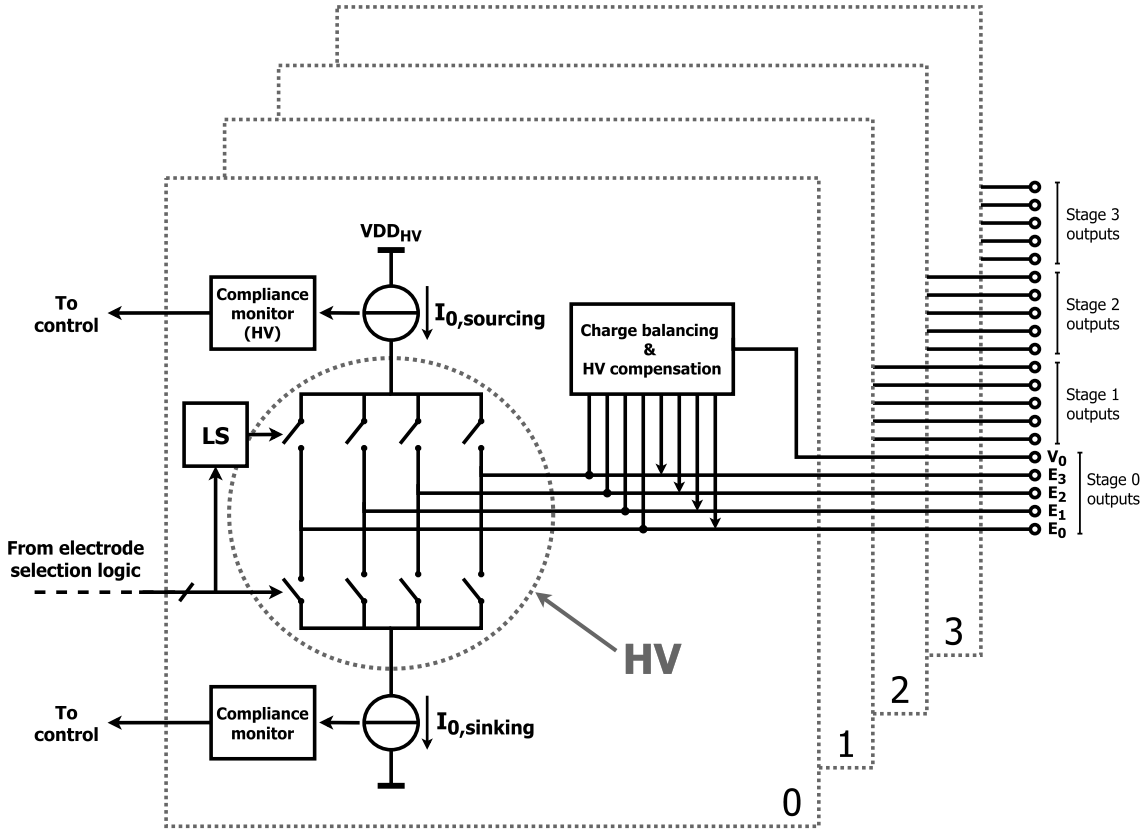

Figure 2.3: System architecture of the output stage of a sinusoidal TI ASIC (adapted from [84]).

Besides that, the system uses a pair of sinking and sourcing current sources as before, but the method of reversing the current direction through the electrodes is now through the use of an H-bridge. This does not mean that the resulting circuit is more correct than the system from Fig. 2.2; if and only if the pair of sources are exactly matched, will the voltages on the connected electrodes be definable. For this (and other) reason(s), compliance monitors are added on each of the eight sources to ensure the same current runs through both ends of the electrodes. The presented system uses two relatively large 9 bit I-DACs to generate sufficiently high resolution sine waves, and to control the amplitude of the current sources.

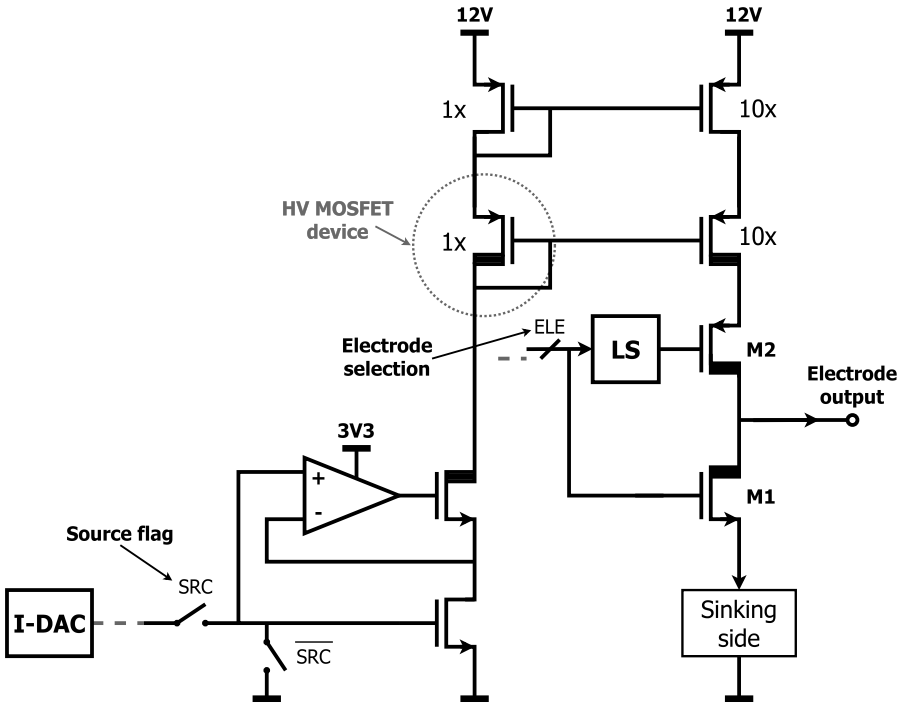

Figure 2.4: The output current source from [84] features a cascoded current mirror as an output stage.

The output stage current sources are implemented as cascode current mirrors. The transistors at the electrode ends are HV devices, as potential differences between electrode ends can vary significantly, due to the large output currents that may be required. In the discussion on the source-to-load transfer of cascoded current mirrors in Sec. 1.3.3, it was assumed that r_o and Z_s are relatively big. A detriment to the dependence of the size of r_o is that the accuracy of the amplifier then depends on the output current of the current mirror transistors. The r_o of such a transistor is inversely proportional to their drain current, which means the amplifier as a whole loses accuracy as the magnitude of the drain current increases. The B-parameter in cascode current mirrors is additionally highly dependent on a relatively high multiplicity α, as otherwise the magnitude of the transconductance g_m of a CS stage would incur a large dependence on the source impedance.

Higher performance in this circuit therefore needs to be achieved by adding surrounding circuitry, like the aforementioned compliance monitors, compensation currents, and ETI sensing circuits. The added circuits are argumented to mainly be there for on-the-fly active charge balancing, due to the semi-continuous nature of TIS and the way remnant offset voltage across the electrodes cannot be measured while the output is 'moving'. In reality, the offset voltage of this design is only exacerbated by the accuracy issues that depend on large output resistance r_o and a multiplicity α that is not dynamically adjusted to the need, as discussed in Sec. 1.3.3.

2.2.2 The essence of TIS and its relation to the output stage

In its simplest viable form (and without charge balancing circuitry), TIS will only require two input current sources, and two pairs of electrodes, of which one electrode can be shared. These sources can provide any arbitrary current and can in theory always be connected to ground or a supply, regardless whether they are sinking or sourcing current, as illustrated in Fig. 2.5. The sources can provide any arbitrary current waveform and magnitude through the nerve tissue, and the interfering electric fields meet the nerve cell at the focal point of the interference, enabling an intermodulation product with frequency $\Delta f = f_1 - f_2$ at this point in the nerve.

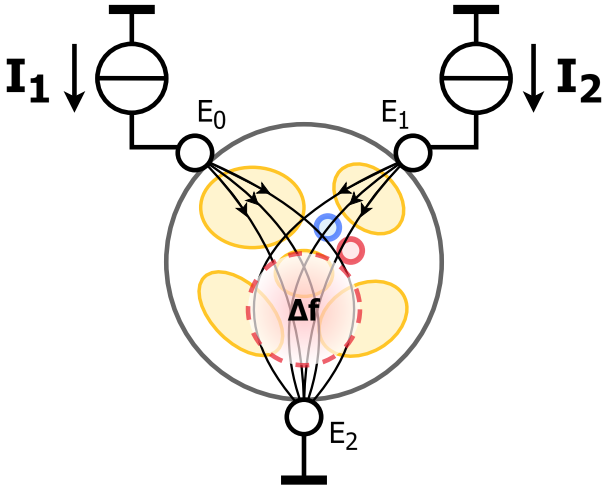

Figure 2.5: The simplest technically viable form of TIS with current-mode stimulation features only three electrodes $E_{0–2}$, and two input current sources.

An H-bridge architecture may be used to reverse the flow of current through the tissue, effectively enabling only sourcing currents from the current sources I_1 and I_2. The choice of whether these currents are sourcing or sinking is arbitrary; the H-bridge architecture flips the current direction even in the case only sinking current sources would be used. The switches of the H-bridge will be controlled by θ_1 and θ_2, respectively setting frequencies f_1 and f_2, as shown in Fig. 2.6.

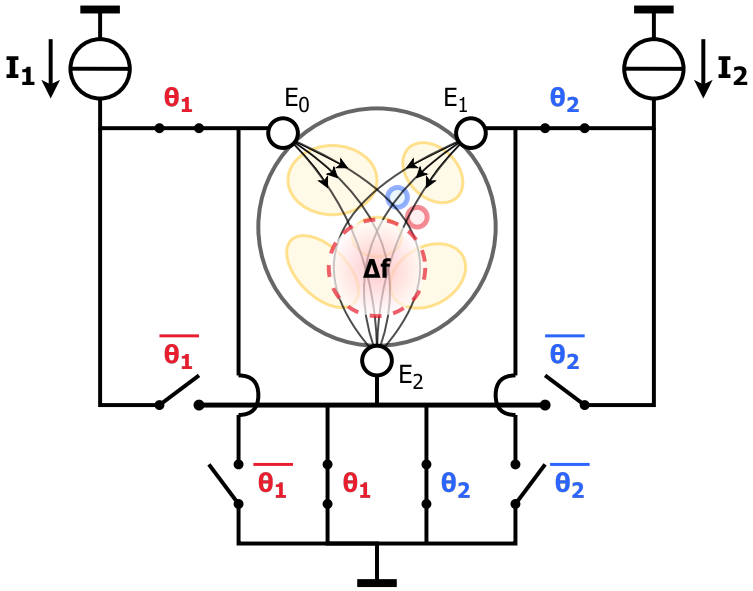

Figure 2.6: A system which employs an H-bridge architecture with a minimum of three electrodes and input sourcing currents I_1 and I_2.

The complications of using a H-bridge architecture and its effects on neural stimulation

It is assumed that, due to the scale of the vagus nerve and kilohertz-range input source frequencies, the generated electric fields change slowly enough for the circuit to be considered quasi-static. Analysis can then be simplified to lumped element models of the tissue impedance, which forms an equivalent circuit with nerve tissue impedances between each electrode. The circuit of Fig. 2.6 can then be seen as three points of a circuit with different tissue impedances Z_{tis1} and Z_{tis2} between electrode E_0 and E_1, and E_0 and E_2, respectively, as illustrated in Fig. 2.7. By inspection, it can be noticed that in some cases where $\theta_1 = 0$ and $\theta_2 = 1$, or vice versa, we lose the negative current direction of I_1 to the ground node by connecting the source straight to it.

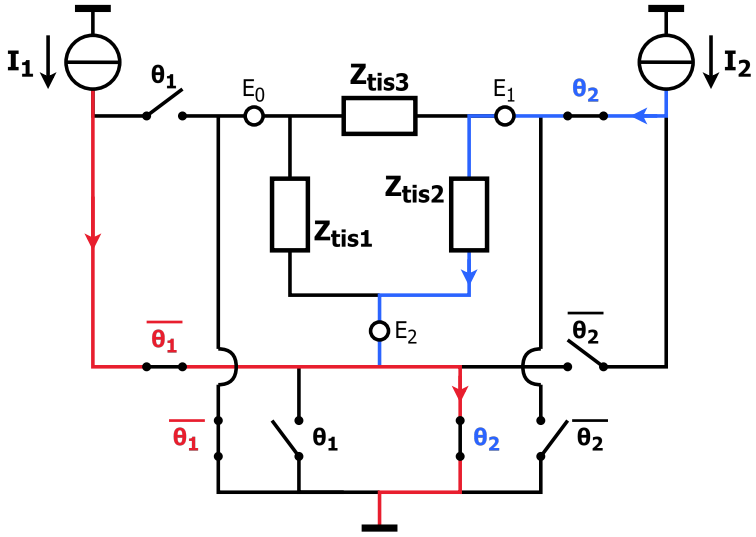

Figure 2.7: Complications regarding the current flow in a three electrode system with $\theta_1 = 0$, $\theta_2 = 1$, and the tissue impedance between E_0 and E_1 much bigger than other impedances. Without ground separation, part of the current from I_1 will not flow through the tissue in this case.

By separating the ground of the two sources, it is ensured the negative phase of the waveform enters the tissue instead of directly flowing to ground. Thus, at least two pairs of electrodes should be used, of which no electrodes can be shared, as in Fig. 2.8. By identically decreasing Z_{tis1}, Z_{tis2}, Z_{tis5}, and Z_{tis6} (respectively putting electrodes $E_{0,1}$, and $E_{2,3}$ closer together in physical space), we maximize crosstalk. Maximizing crosstalk in the context of TIS is good for power-efficient stimulation, as we can be fairly sure the intended amplitude modulation will at least happen at the focal point in the tissue. However, we lose all spatial selectivity in the process, as all other nerve cells in the signal path from the sourcing side to the sinking side will receive similar stimulation waveforms (in other words, the focal 'point' is stretched out over a wider area). Vice versa, by identically increasing Z_{tis1}, Z_{tis2}, Z_{tis5}, and Z_{tis6} (respectively putting electrodes $E_{0,1}$, and $E_{2,3}$ further apart in physical space) we minimize crosstalk and maximize spatial selectivity, at the cost of power-efficiency, as more electrical energy is required to achieve the same amount of stimulation at the focal point compared to when electrodes $E_{0,1}$ and $E_{2,3}$ were closer together.

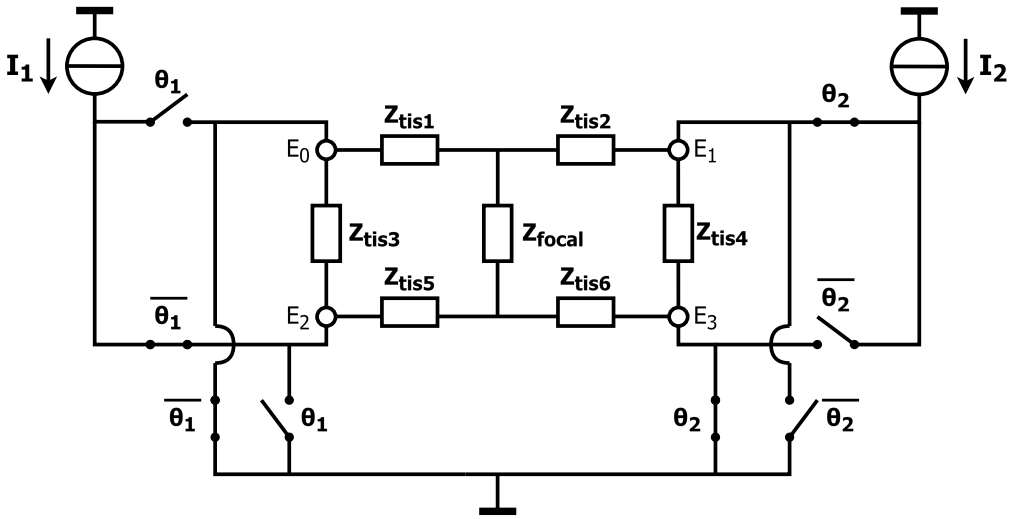

Figure 2.8: A system which employs an H-bridge with a minimum of four electrodes and sourcing currents I_1 and I_2. The crosstalk experienced by the focal point of stimulation changes depending on the physical placement and amount of electrodes around the nerve.

It is thus the different impedances between electrodes which will cause either more, or less, power to be absorbed at the tissue focal point, which either worsens spatial selectivity, or power-efficiency, respectively. That is, if we do not use a larger amount of electrodes to provide more selective, power-efficient stimulation.

On resolution and the size of control circuitry

Adding more than just the strictly required four electrodes that are connected to the two H-bridges adds a finer control of the amount of locations that are accessible by the focal point of interference; we add more spatial selectivity, and are less dependent on tissue impedance changes from longer distances, by adding more electrodes. However, as we increase the amount of electrodes, the size of the control circuitry for choosing every combination of four electrodes out of the total amount of electrodes increases, and the total area of this selection logic on-chip (and related parasitic capacitance) increases exponentially with it. Therefore, there are diminishing returns with regard to spatial selectivity and area costs, which are not yet defined in the field of TIS.

2.3 A power-efficient vagus nerve stimulator design for TIS

2.3.1 Full system architecture

Based on all presented considerations of the previous sections, a system architecture for an implantable temporal interference-based vagus nerve stimulator with wireless power transfer is shown in Fig. 2.9.

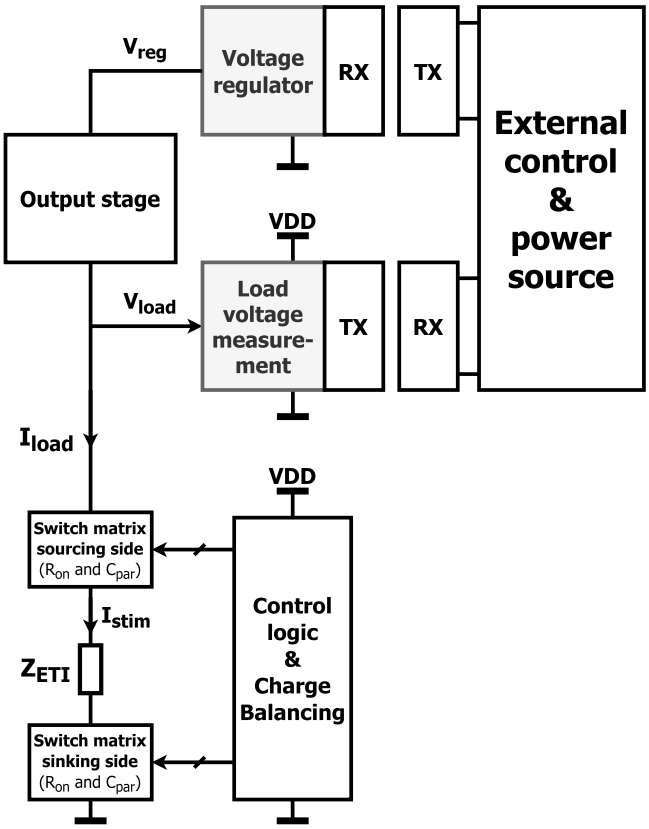

Figure 2.9: The total system architecture.

The function of each block is briefly described below:

- **Load voltage measurement and low-voltage transmission:** The load voltage V_ℓ is measured, and shifted down by an amount suited for low-voltage (LV) circuitry and logic. The resulting load voltage measurement is a ratiometric quantity of the maximum supply voltage that can be provided by the regulated supply voltage. If $V_{reg,max}$ and the set overhead is known, the load voltage can be shifted down with a known ratio to the low-voltage regime, which can then be digitized in an ADC and transmitted to the external control circuit for processing.
- **Voltage regulator and external power source:** The discussed supply regulation method of Sec. 1.3.2 is largely implemented by the load voltage measurement circuitry, external control circuitry, and external adjustable power source. Some overhead voltage is added on top of the measured and digitized ratiometric load voltage quantity. This voltage is then used to update the amplitude setting of an AC power source

at the output of the adjustable power supply. The power from the adjustable power source is transmitted through the tissue, where a receiver and voltage rectifier provide the newly updated regulated voltage supply to the circuit. The mode of transport for the transmitted and received power can in reality be any form of electro-magnetic, ultrasound, light or capacitive power transfer, which in the following will be assumed to be lossless and ideal (which will be further discussed in Sec. 2.3.3). A second, separate voltage regulator can provide the needed voltage for low-voltage circuitry of the measurement circuit and switch matrix logic.

- **Switch matrices and related control circuitry:** The switch matrices consist of a network of sourcing- and sinking-side switches, that are made to provide any arbitrary number or partitioning of electrodes with control signals that are required to reverse current direction through the tissue, as enabled by the H-bridge architecture. The control logic, which defines the direction of the output current from the output stage through the tissue, is dependent on the source current frequency to decide on the frequency to control the switches in the switch matrix.
- **Charge balancing by offset regulation and related control circuitry:** Active, semi-continuous charge balancing by means of offset regulation has an effect on the enabled current direction and amplitude of the source current to effectively eliminate any remnant charge during semi-continuous stimulation cycles.

2.3.2 Output stage design

The initial active current mirror design from Fig. 1.24, as discussed in Sec. 1.3.3, is chosen as the output stage architecture for the stimulator, as it provides a unique solution for indirect feedback current-mode stimulator output stage design in combination with a regulated supply, as shown in Fig. 1.25. The transistor-based design of the stimulator circuit with supply regulation will be discussed in the following, with a focus on arriving at a circuit design proposal that can be implemented for simulation, which is further discussed in Ch. 4.

Supply regulation and subsequent overall system specifications

The regulated supply makes the whole system feedback load dependent. The regulated supply voltage was found to be:

$$V_{reg} = V_{\ell} + V_{overhead}. \tag{2.13}$$

The maximum regulated supply voltage is defined by the maximum load voltage the system is designed for, in addition to the minimum overhead voltage required for the operation and compliance of current sources in the output stage. Due to this fact, the switch matrix will have a noticeable effect on the compliance range of the output stage.

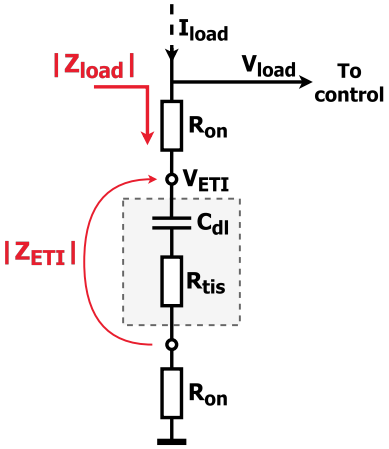

Figure 2.10: The total equivalent load resistance can be estimated by magnitude measurements of the electrode impedance magnitude in a relevant frequency bandwidth for VNS.

In most cases, a switch matrix can be modelled as an equivalent R_{on} and (parasitic) input and output capacitances $C_{in,out}$. For the gain of the circuit, the R_{on} is of the highest importance, as it is in series with the load (as shown in Fig. 2.10), assuming the parasitic capacitances are relatively small. In previous work, it was found through measurement with kHz-range input waveforms that the magnitude of the end-to-end electrode-tissue interface impedance $|Z_{ETI}|$ for temporal interference stimulation on the vagus nerve of pigs was determined to be about 1 kΩ at maximum, for which up to 10 mA of stimulation current was required to stimulate the focal point of interference [66]. The total equivalent load impedance magnitude at relevant VNS input frequencies for TIS can then be estimated to be:

$$|Z_{\ell}| = 2R_{on} + |Z_{ETI}|. \tag{2.14}$$

The maximum supply voltage of the proposed regulated supply will have to be limited due to operational compliance of HV transistors, and thus the total output current swing will also be tied to that limited maximum voltage. Taking $V_{\ell,max} = 12V$ as an example, with a maximum load current of $I_{\ell,max} = 10\,mA$, these specifications require:

$$2R_{on} \leq \frac{V_{\ell,max}}{I_{\ell,max}} - |Z_{ETI}| = \frac{12\,V}{10\,mA} - 1\,k\Omega \Rightarrow R_{on} \leq 100\Omega. \tag{2.15}$$

This means the maximum load impedance magnitude in the relevant bandwidth of stimulation will be:

$$|Z_{\ell,\max}| = 2R_{\text{on,max}} + |Z_{\text{ETI,max}}| = 200\Omega + 1\text{k}\Omega = 1.2\text{k}\Omega. \tag{2.16}$$

The part of the load voltage that ends up at the ETI, denoted as V_{ETI}, is determined by the voltage divider that is formed by the magnitude of the on-resistance R_{on} and the ETI $|Z_{\text{ETI}}|$ in the physically relevant bandwidth of input stimulation frequencies:

$$V_{\text{ETI}} = \frac{|Z_{\text{ETI}}|}{2R_{\text{on}} + |Z_{\text{ETI}}|} V_{\ell}. \tag{2.17}$$

Thus, when we arbitrarily decide that a minimal worst-case overhead of $V_{\text{overhead,min}} = 1\,\text{V}$ is needed, and the maximum load voltage is allowed to be $V_{\ell,\max} = 12\,\text{V}$, then the maximum regulated supply voltage will need a maximum magnitude value of:

$$V_{\text{reg,max}} = V_{\ell,\max} + V_{\text{overhead,min}} = 13\,\text{V}. \tag{2.18}$$

All current that flows through the source and load branch now flows out of the regulated supply, denoted as I_{tot}. The power absorbed by the ETI and the total power spent by the regulated supply output stage system can then be derived to be:

$$P_{\text{ETI}} = V_{\text{ETI}} I_{\ell}, \tag{2.19}$$

and

$$P_{\text{tot}} = V_{\text{reg}} I_{\text{tot}}. \tag{2.20}$$

The effect of current gain value on output stage area and power consumption in indirect current amplifiers

Scaling the value of the multiplicity α has a defined effect on the current gain of the source-to-load transfer, and thus on the maximum amplitude of the source current I_{s}, but also on the area and output capacitance of the output stage. If we define the transistors inside the current mirror output stage to have a set (W/L) ratio, and increase the multiplicity of the transistors on the output branch arbitrarily, the active area increases just as much; the area scales proportionally to α:

$$A_{\text{t}} \propto \alpha. \tag{2.21}$$

The relation in (2.21) is in contrast to the power spent on the magnitude of the source current, as the maximum amplitude of the source current can get smaller with increasing α; the power spent on the source current branch scales proportionally to $1/\alpha$:

$$P_{\text{s}} \propto \frac{1}{\alpha}. \tag{2.22}$$

If we define power spent on the source branch as a part of the total power spent by the regulated power supply, as in:

$$P_{\text{tot}} = P_{\text{reg}} = P_{\text{s}} + P_{\ell} = P_{\ell}\left(1 + \frac{1}{\alpha}\right), \tag{2.23}$$

it quickly becomes apparent that the power savings that are gained by increasing α will at some point become negligible compared to the useful power spent on stimulation. As an example, if we define $\alpha = 100$, the proportionality factor of (2.22) becomes the fraction of the total power spent on the source current branch:

$$P_{\text{s}} \propto \frac{1}{\alpha} = \frac{1}{100} = 1\%. \tag{2.24}$$

Given the active area of the output stage transistors now scales by:

$$A_{\text{t}} \propto \alpha = 100. \tag{2.25}$$

Doubling α then leads to:

$$P_{\text{s}} \propto \frac{1}{2\alpha} = \frac{1}{200} = 0.5\%, \tag{2.26}$$

and

$$A_{\text{t}} \propto 2\alpha = 200, \tag{2.27}$$

which means only 0.5% of the total power spent is saved for a doubling of the circuit area. Similarly, if α were to be halved (to $\frac{1}{2}\alpha = 50$), the circuit would spend twice as much power on the source current branch, for half the area. In the following, it is therefore decided that $\alpha = 100$, as the relative fraction of the power that is saved by implementing a much higher α is not deemed to be worth its cost in area. This has a profound effect on the dynamic characteristics of the output stage (like slew rate and total bandwidth), which will be further discussed in Ch. 4.

Source and load parameters

In reality, the load at the output of the current amplifier consists of the charge storage and nonlinear characteristics of the ETI and the series impedance introduced by the switch matrix. Additionally, the use of a H-bridge architecture and, in some cases, fast rising and falling edges of the source current, means the gain of the circuit at higher frequencies will be relevant when switching between the different electrodes of the circuit. DC offset caused by remnant charge on one of the electrode ends at the end of one stimulation phase could influence the output behaviour in the following stimulation phase, meaning the behaviour and accuracy of the output stage needs to be validated for situations where remnant charge is stored on the ETI, and when the input waveforms feature high frequency components.

In the following sections, the ETI will be modelled by only the double-layer capacitance C_{dl} and tissue resistance R_{tis}. The faradaic impedance Z_F is not modelled, as the circuit is assumed to be operating in the region where the tissue resistance dominates, as discussed in Sec. 1.2.1. The parasitic capacitance of the switch matrix is considered negligible, which leaves only the on-resistance R_{on} of a single transistor switch in series with the ETI.

It was found earlier that the output stage with supply regulation faces a penalty in that its source impedance will need to have a certain value much larger than the load impedance to approach the ideal gain of the transfer, as the asymptotic gain of the source-to-load transfer is given by:

$$\frac{I_\ell}{I_s} = \frac{\alpha Z_s}{\alpha Z_\ell - Z_s}. \tag{2.28}$$

The absolute asymptotic gain over the whole range of relevant load impedance magnitudes can then be defined in terms of a gain accuracy δ and minimum source impedance magnitude $|Z_{s,min}|$ as:

$$\left|\frac{I_\ell}{I_s}\right| = \alpha\delta, \tag{2.29}$$

where

$$\delta = \frac{|Z_{s,min}|}{\alpha|Z_{\ell,max}| + |Z_{s,min}|}. \tag{2.30}$$

The maximum load impedance magnitude in the relevant bandwidth of stimulation was previously estimated to be $|Z_{\ell,max}| \approx 1.2\,k\Omega$. Assume, for the purposes of discussion, that a 3σ-accuracy of the load current is required, due to concerns regarding charge accumulation. A 3σ-accuracy is equivalent to a load current accuracy of 99.7%. In the case of VNS stimulation using TIS methods, this means the load current is not off by more than $30\,\mu A$ over the whole load impedance range. The minimum magnitude of the source impedance will need to be:

$$|Z_{s,min}| = \alpha|Z_{l,max}|\left(\frac{\delta}{1-\delta}\right) = 100 \cdot 1.2\,k\Omega\left(\frac{0.997}{1-0.997}\right) \approx 40\,M\Omega, \tag{2.31}$$

which is fairly large. Such source impedances can be achieved by, for example, cascoding the output source current of the I-DAC, or by some other technique to improve its output resistance. Interestingly, the narrative in literature for conventional current mirrors has been to increase the equivalent output resistance R_o of current sources at the load to gain accuracy, whereas it was shown that, in the case of the discussed output stage architecture, an increased output resistance at the source is required (when the voltage gain of the regulated supply is adequately large).

Typical values of the double-layer capacitance C_{dl} in TIS may be higher than $1\,\mu F$ depending on size, material and electrode quality. In the following, a double-layer capacitance of $50\,\mu F$ is assumed, of which the effect will be discussed in Sec. 4.2.2. Additionally, the effect of high multiplicity on intrinsic transistor capacitances can be fairly large. Most importantly, the output stage transistors scale the drain-gate capacitance c_{dg} and gate-source capacitance c_{gs} by $\alpha = 100$, largest of which will be αc_{gs}. However, the introduced poles and zeroes by the parallel connection of multiple intrinsic transistor capacitances does not matter much for the output stage; aside from an affected slew rate, the introduced poles and zeroes are far removed from the kHz-range switching frequencies employed in TIS. The slew rate is relevant when considering the use of rectangular waveforms, as the most dominant pole introduced by the intrinsic capacitances will limit very fast transients beyond a few MHz (as the size of αc_{gs} and αc_{dg} lies in the range of a few pF to a few hundred pF). The transfer characteristics are mostly decided by the dominant pole introduced by the very large double-layer capacitance C_{dl} and the value of the tissue resistance R_{tis}.

From a stimulation standpoint, the LPF-like characteristics of the neuron significantly reduce the effectiveness of stimulation beyond a stimulation frequency of about 10 kHz. If the double-layer capacitance is large enough, the very dominant pole of the double-layer capacitance has a corner frequency at a low enough frequency that the bandwidth of stimulation is not unnecessarily reduced. Any frequency components beyond a frequency of 10 kHz that are present in fast switching transients will be passed through the double-layer capacitance to the tissue, but they will largely be ignored by the preference of the neuron for low stimulation frequencies, manifesting in reduced threshold currents for stimulation frequencies <50 Hz in vagus nerve stimulation.

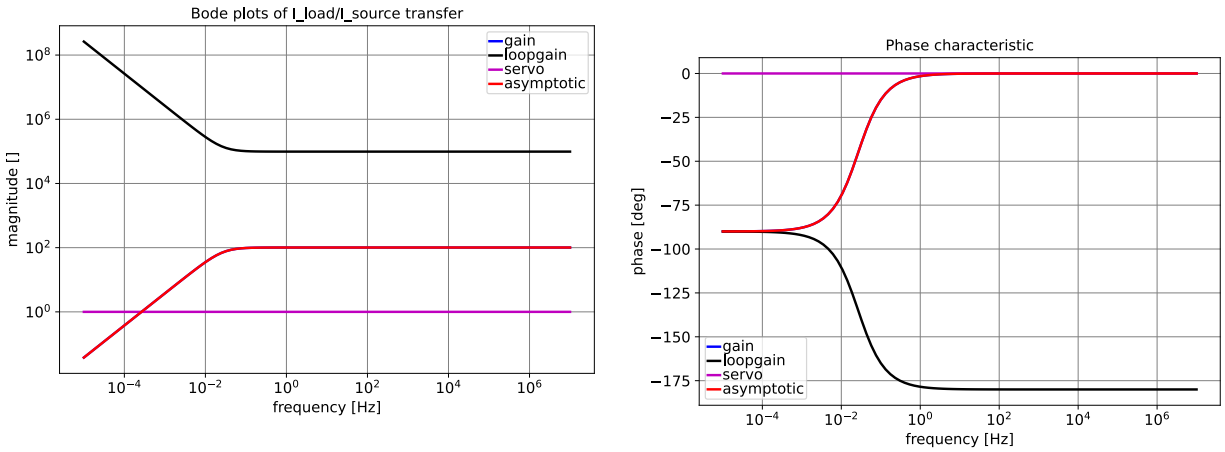

(a) Magnitude plot.

(b) Phase plot.

Figure 2.11: **(a)** The gain stays constant after the initial pole introduced by C_{dl}. When C_{dl} is sufficiently big, its influence on the physiologically relevant bandwidth gets less. Intrinsic transistor capacitances of the output transistors will affect the bandwidth if the multiplicity is too big, which will be shown in Ch. 4. **(b)** Due to having no frequency compensation, the pole introduced by the tissue impedance makes the system inherently unstable. This is alleviated by the fact that the supply cannot be unlimited, resulting in clipping. In this case, it is a desired effect, as the load current is then largely determined by the regulated supply (and some small overhead).

To show the effect of the dominance of the double-layer capacitance, the circuit of Fig. 1.25 is simulated to show the Bode plots of the gain, loopgain, servo function and asymptotic gain, as in Fig. 2.11. Parameter values for a MOSFET device are estimated for illustrative purposes, and are set such that at the highest current magnitude, $g_m = 3\,\text{mS}$ and $r_o = 300\,\text{k}\Omega$, with $\alpha = 100$, $C_{dl} = 50\,\mu\text{F}$, $R_{on} = 200\,\Omega$, and $R_{tis} = 1\,\text{k}\Omega$.

Controller design

The type of controller that is needed to replace the function of the voltage gain of E1 can be implemented in many ways. The chosen implementation is shown in Fig. 2.12, by a transistor of which the gate is connected to the regulated supply (common-gate stage). A rise of source voltage, due to a rise in the source current, will cause a decreased output voltage on the output of the controller. The output PMOS transistors M1 and M2 of the current mirror will respond by maximizing the current for the given supply, as determined by the ratio of the current mirror multiplicity. The supply is set by the regulated supply voltage, which ultimately is defined by the load voltage. The output current will be amplified regardless of the load impedance, but the resulting load voltage and supply voltage are very much load dependent. The functioning parts of the whole system are therefore split into a 'blindly' amplifying output stage and a voltage regulation circuit that controls the voltage drop on the output transistor M2.

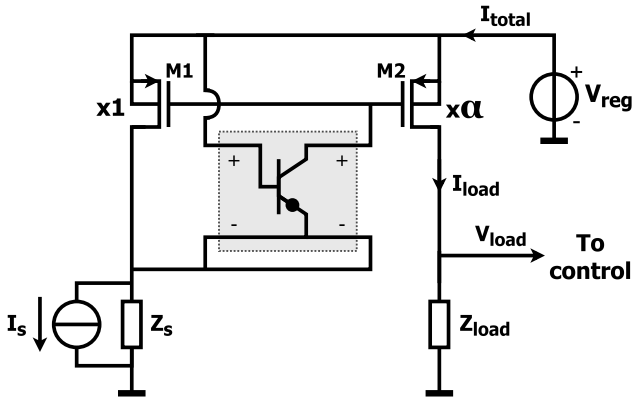

Figure 2.12: The circuit with regulated supply voltage V_{reg} and proposed controller, which features an ideally biased transistor device.

Biasing

The proposed biasing scheme is shown in Fig. 2.13a, alongside typical biasing sources of a CS stage in Fig. 2.13b. The gate voltage and current biasing sources V_{GS} and I_G of the typical CS stage are implemented in large part by M1, with the current through it defined by the minimum overhead created by the regulated supply voltage. The drain current biasing source I_D is added by a nonlinear resistor with a current source character, which can later be implemented as a current mirror with a small biasing current. The drain voltage biasing source V_{DS} is not explicitly added, as the biasing current source I_D and supply regulation make that the controller output voltage V_{con} always lies somewhere between the regulated supply voltage V_{reg} and source voltage V_s. The degree to which V_{con} can change within this range is determined by the set overhead, which should be chosen sufficiently high enough for accuracy of the maximum load current.

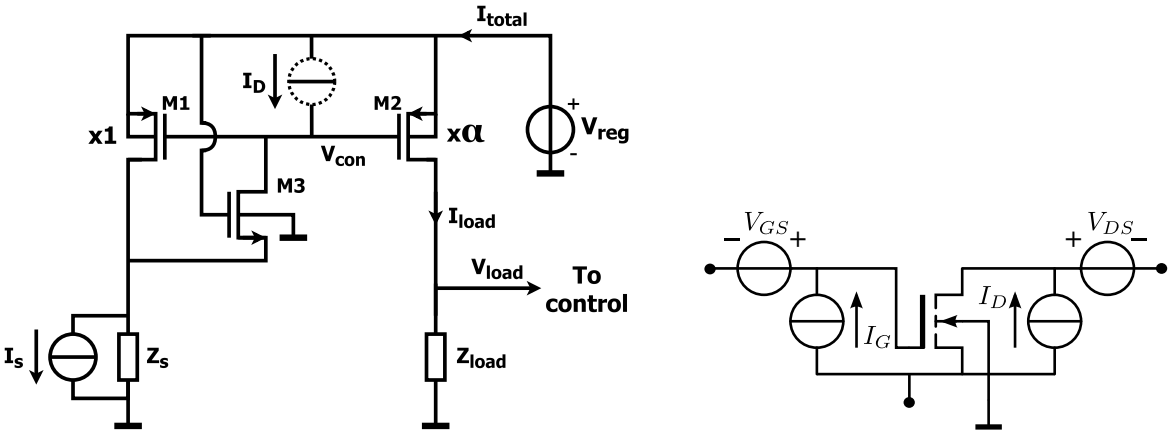

(a) Proposed biasing of the system.

(b) A biased CS stage (from [64]).

Figure 2.13: **(a)** The biasing involves only a single nonlinear resistor with a current source character at the drain of M3, due in part to the way the regulated supply is implemented. **(b)** A biased CS source consists of four sources to make sure the CS stage resides in a quiescent operating point.

The biasing current through the drain of M3 adds an offset caused by the relatively large source impedance, which will affect the load current. The biasing current can be accounted for in the reference current source, or by changing the source impedance to account for the voltage offset that is created. In any case, the biasing current will need to be fairly small, to not be as big in magnitude as the already rather small magnitude of the input source current. The biasing scheme can also be made such that the biasing current runs parallel to the input source current, with a large resistor at the drain of M3 to define the V_{DS}. However, this is not implemented, as noise on the supply was already not filtered out severely well, which would then be exacerbated by the relatively large resistance, eventually affecting the load current.

The effect of noise on the gate voltage of M2, and the related accuracy of the output current, are arguably not as important when stimulation magnitudes are fairly high. Scientific perspectives on this issue differ, as the literature often prefers precise control over the injected charge by focusing on the design of accurate output current sources. However, with the addition of charge balancing circuits, the requirements of accuracy may be severely lowered.

Proposed output stage circuit design

The total proposed circuit design for the output stage, with supply regulation, multiplicity, source and load parameters, controller, and biasing as discussed before, are shown in Fig. 2.14. The biasing source I_D is implemented as a current mirror, and the regulated supply, and its related control, are assumed to be ideal.

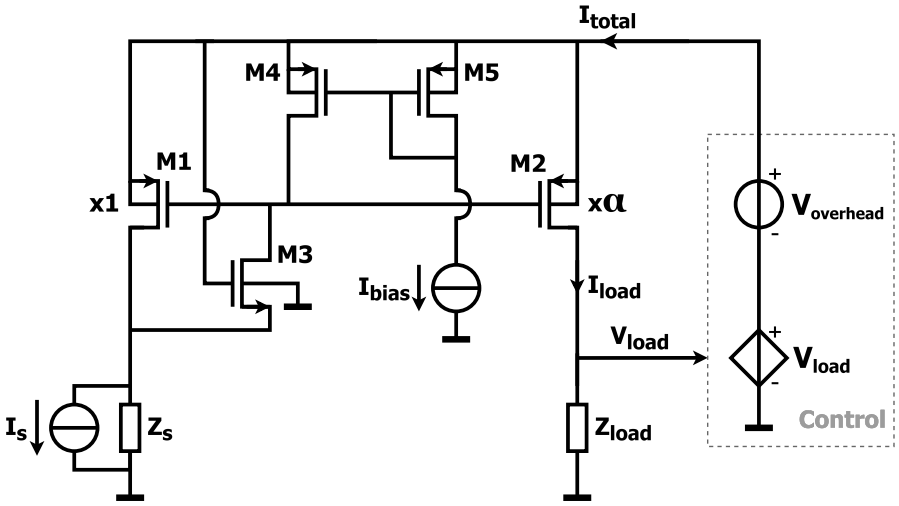

Figure 2.14: The proposed circuit design.

2.3.3 Digital circuitry

The digital circuitry shown in the full architecture of Fig. 2.9 is not the focus of this report, and will therefore be assumed ideal, as many successful approaches to the implementation of these blocks already exist. Implementation of these blocks requires some conscious design decisions when considering its interaction with the output stage and regulated supply, which will briefly be touched upon in the following.

Voltage regulator, external power source and power receiver

In theory, the output voltage of the rectifier needs to have a value that only adds the overhead required for the biasing of current sources in the output stage. The power savings enabled by the regulated power supply happen outside the output stage circuit, in the output of the external power source. If the external power signal were to be received as an AC voltage, the (ideal) amplitude of the received AC power would be equal to the required regulated supply voltage, assuming all transmission and subsequent voltage rectification is ideal. In reality, power is lost to dissipation through the skin and leakage in rectification, meaning the amplitude of the AC voltage from the external power source will need to be (much) higher. Power efficiency of wireless power transfer is still largely debated in research [85], but ultrasound power transfer seems promising [86, 87].

Switch matrix design

It was briefly discussed that an increase of output electrodes increases spatial selectivity, at the cost of area and switch matrix complexity. The presented design can be hooked up to an arbitrarily varying amount and partitioning of output electrodes. A design that uses eight electrodes and two output channels in a H-bridge architecture was made as an example, as shown in Fig. 2.15. The choice of a H-bridge architecture requires that the load current is always either a sourcing or sinking current. The switch matrix control logic controls the direction of the current through the tissue, so that the output stage does not have to also provide the opposite current direction through the tissue.

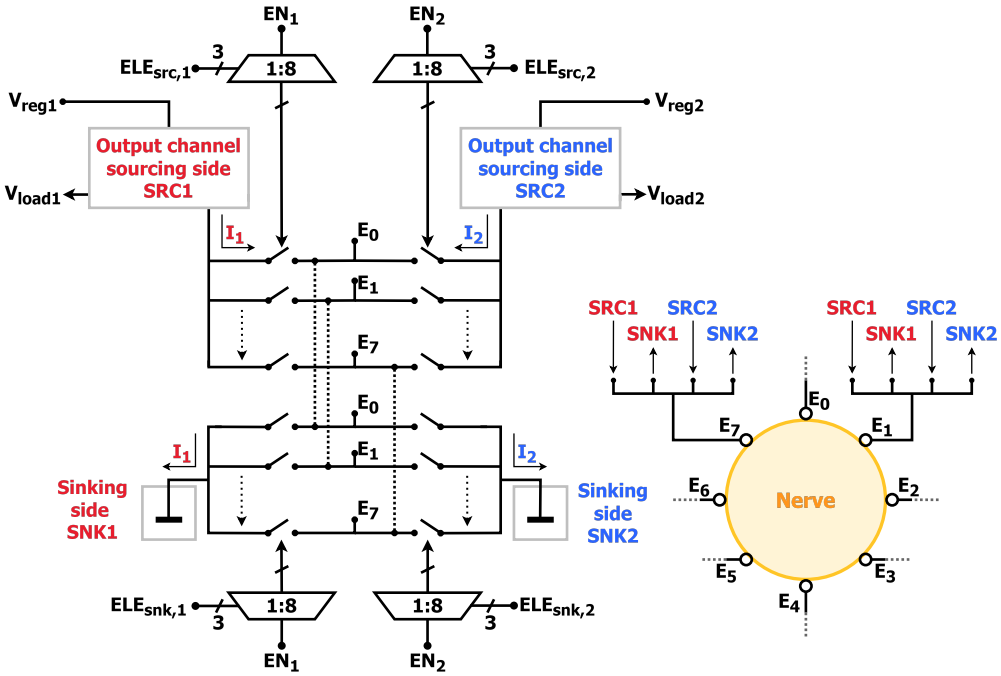

Figure 2.15: An example of a switch matrix design for the simultaneous implementation of eight electrodes. Adding more than eight electrodes adds more complexity to the selection logic, which could grow exponentially.

The two output channels each have two separate voltage regulated supplies. Each of the eight electrodes is connected to four switches, which effectively form the H-bridge across the ETI once activated. Every switch is normally off, unless selected by the user, or the flow of current is enabled by EN_1 or EN_2. The user provides four unique 3 bit codes $ELE_{src,1}$, $ELE_{snk,1}$, $ELE_{src,2}$, and $ELE_{snk,2}$ as select bits to respectively four 1:8 demultiplexers, which can select an electrode and corresponding switch to turn on. The selected electrode code is then swapped with whatever electrode was previously either on the sinking or sourcing side by changing the electrode selection code, with a frequency defined by θ_1 or θ_2 (as illustrated in Fig. 2.8). The source current input signal defines the specific frequency and amplitude that is also used for properly operating the switch selection logic.

This design makes sure only two switches will ever be in the signal path of each output channel, to reduce overhead created by the R_{on} of the electrode switch matrix on the sourcing and sinking side. Adding more than eight electrodes adds more parasitic capacitances, resulting in loss of bandwidth and leakage through parallel (unselected) transistors. Each output channel will require a regulated supply, which could lead to a trade-off when considering system complexity. As such, partitioning the system in groups of electrodes, and connecting these to the amount of output signals required, are factors that should be taken into account when designing for limited area.

Semi-continuous charge balancing

The discussed technique of TIS requires a certain on-time, of at least $t_{on} = \frac{1}{\Delta f}$, to provide a full stimulation waveform at a sufficiently slow frequency Δf. The time it takes for this to finish may be too late in terms of remnant charge left on the electrode, which means it has to be accounted for within the same time frame. Some successful techniques were previously discussed, of which the offset-regulation technique seems most promising, considering the continuous feedback used to adjust the charge.

If it can be assumed that the R_{on} is relatively well-known and the load impedance is accurately related to the source-to-load transfer of the output stage by some accuracy δ as in (2.29), then in the physiological bandwidth of vagus nerve stimulation, it can be assumed that:

$$|Z_\ell| \approx \frac{V_\ell}{I_\ell}, \tag{2.32}$$

$$\Rightarrow |Z_{ETI}| \approx \frac{V_\ell}{\alpha\delta I_s} - 2R_{on}. \tag{2.33}$$

When the remnant charge on the electrode causes an increase in load voltage V_ℓ, the resulting ETI appears to be increased, even though the other parameters in (2.33) can be assumed to be known. With that in mind, an initial measurement of the load voltage without remnant charge can be made ahead of normal stimulation, in a way that is more charge controlled. The measurement forms a benchmark which all subsequent load voltage measurements can compare to. If the load voltage then causes a deviation of the expected ETI by an unsafe amount, the input source current magnitude can be reduced by a known amount. Once at least one stimulation cycle is finished, as determined by the particular on-time $t_{on} = \frac{1}{\Delta f}$, a new measurement of the ETI can be taken. There has to be an amount of confidence in the fact that the remnant charge at the end of the on-time is properly balanced out, as lenient safety ranges will cause this kind of control to eventually fail.

Lastly, single pulsed temporal interference stimulation (spTIS) is a novel TIS technique that attempts to do away with the semi-continuous nature of conventional TIS, in favour of sending pulsed versions of the input waveforms [88]. This may cause the speed at which charge accumulates on the electrodes to drastically reduce, allowing for inter-pulse delays in which the charge can be balanced by pulse insertion.

2.4 Research aim

In the previous sections, the practical considerations of temporal interference-based neural stimulators have been discussed in detail. These included an analysis of the conventional modelling of electrophysiological properties of neurons under influence of TIS, and the design of a power-efficient temporal interference-based vagus nerve stimulator system. The research reported in the following chapters aims to:

1. Develop an accurate nonlinear model for the representation of neuron responses to temporal interference stimulation.
2. Test whether intermodulation products are accurately represented by the proposed model, and to see whether there is a way to define stimulation efficiency of various waveform shapes using the model.
3. Measure the power efficiency and accuracy of the proposed output stage to compare to conventional current-mode stimulation output stages.
4. Measure the proposed output stage response to fast transients in AC measurements and its behaviour when subjected to remnant charge on the electrodes at varying phases in the stimulation cycle.
5. Assess the performance of the proposed output stage in a crosstalk setup, focusing on spatial selectivity, energy efficiency, and charge accumulation during stimulation.

Chapter 3

Modelling nonlinear responses of neurons to high-frequency interfering electric fields in temporal interference stimulation

3.1 Method

Considering a nonlinear frequency mixing mechanism could be present in the neuron membrane, a mathematical model that generalizes the behaviour of the stimulation mechanism behind TIS is required to explain measured frequency components that emerge only when frequency mixing occurs. A block diagram of the proposed model is presented in Fig. 3.1.

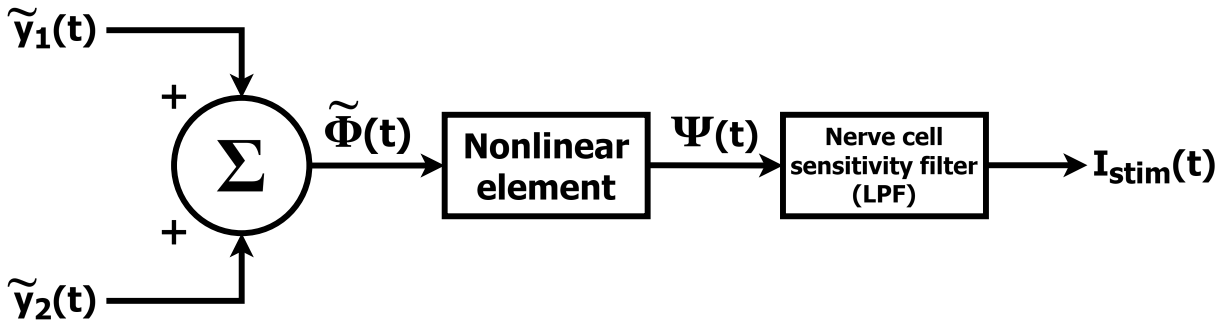

Figure 3.1: Block diagram of the newly proposed model for neuron responses to interfering electric fields, based on nonlinear distortion of the input waveforms $\widetilde{y}_1(t)$ and $\widetilde{y}_2(t)$. The summation of the two inputs $\widetilde{\Phi}(t)$ meets a nonlinear element within the neuron membrane that produces an output $\Psi(t)$, of which the frequency components can cause an action potential at sufficiently high magnitudes of I_{stim}.

The constituent electric field inputs, which are continuous harmonic, one-dimensional wave functions $\widetilde{y}_1(t)$ and $\widetilde{y}_2(t)$, sum up to form the superposition $\widetilde{\Phi}(t)$. This superposition of waveforms meets some nonlinear element that produces the frequency mixing spectral products, as otherwise frequency components with two, three or four times the difference frequency Δf could not have been measured in previous studies [79–83, 89]. The output of the nonlinear element, $\Psi(t)$ (which contains the frequency mixing products), is selectively filtered by the nerve cell's LPF-like sensitivity to certain frequency components. These preferential frequencies are theorized to be due to differences in ionic conductance of the in- and outward flow of ions around the membrane. The introduced electric field at the preferred frequency induces ionic current flow, resulting in a stimulation current $I_{stim}(t)$.

Additionally, it is assumed that the waveform $\widetilde{\Phi}(t)$ operates in the ideal operating point, or the quiescent operating point, of the input-output transfer. This is because the input waveforms, $\widetilde{y}_1(t)$ and $\widetilde{y}_2(t)$, are defined such that the phase difference $\Delta\phi$ is zero (there is no offset in time), and the average mean value of the waves Φ_0 is zero (there is no offset in the DC value of the input). In reality, the phase difference is of no importance, as the input frequencies have a slight difference of Δf. However, the offset introduced by the value of Φ_0 manifests itself as a remnant voltage on the electrode leads, which is especially relevant to the topic of charge balancing. Regardless, in the following we will assume these offsets are both zero, and the output is in the quiescent operating point, at the centre of the focal point of stimulation.

The input/output relationship of the nonlinear element can be approximated by a Taylor expansion about $t = 0$ as follows:

$$\Psi(t) = K_1\widetilde{\Phi}(t) + K_2\widetilde{\Phi}^2(t) + ... = \sum_{n=1}^{\infty} K_n\widetilde{\Phi}^n(t), \tag{3.1}$$

with the Taylor expansion coefficient of a specific order n given by:

$$K_n = \frac{1}{n!}\left|\left(\frac{d^n\Psi(t)}{dt^n}\right)\right|_{t=0}. \tag{3.2}$$

The superposition of the two inputs $\widetilde{y}_1(t)$ and $\widetilde{y}_2(t)$ is given by $\widetilde{\Phi}(t)$, which is inserted in the Taylor expansion of (3.1) to get:

$$\Psi(t) = \sum_{n=1}^{\infty} K_n\widetilde{\Phi}^n(t) = \sum_{n=1}^{\infty} K_n[\widetilde{y}_1(t) + \widetilde{y}_2(t)]^n. \tag{3.3}$$

This relation can be written as a binomial expansion of the two signals, expanded for every Taylor expansion order up to infinity:

$$\Psi(t) = \sum_{n=1}^{\infty} K_n[\widetilde{y}_1(t) + \widetilde{y}_2(t)]^n = \sum_{n=1}^{\infty} K_n \sum_{m=0}^{n} \binom{n}{m} (\widetilde{y}_1(t))^{n-m}(\widetilde{y}_2(t))^m. \tag{3.4}$$

The derived model in (3.4) represents the output waveform that can be created by a superposition of two one-dimensional, lossless electric waves, as produced by the nonlinear frequency mixing characteristic of the neuron membrane. As an example, the Taylor expansion up to the third order can be produced by replacing the infinite sum of the Taylor expansion by a sum from $n = 1$ to $k = 3$, using Pascal's triangle from the binomial theorem:

$$\Psi(t) = \sum_{n=1}^{k} K_n \sum_{m=0}^{n} \binom{n}{m} (\widetilde{y}_1(t))^{n-m}(\widetilde{y}_2(t))^m = K_1[\widetilde{y}_1(t) + \widetilde{y}_2(t)] + K_2[\widetilde{y}_1^2(t) + 2\widetilde{y}_1(t)\widetilde{y}_2(t) + \widetilde{y}_2^2(t)] +$$

$$K_3[\widetilde{y}_1^3(t) + 3\widetilde{y}_1^2(t)\widetilde{y}_2(t) + 3\widetilde{y}_1(t)\widetilde{y}_2^2(t) + \widetilde{y}_2^3(t)], \tag{3.5}$$

where, in the case we are using sinusoidal waves like in sinusoidal TIS, $\widetilde{y}_1(t) = A_1\cos(\omega_1 t)$, and $\widetilde{y}_2(t) = A_2\cos(\omega_2 t)$. The 1^{st} order term, $K_1[\widetilde{y}_1(t) + \widetilde{y}_2(t)]$, represents the simple superposition of the two inputs, and therefore produces frequency components at $\omega_1 = 2\pi f_1$ and $\omega_2 = 2\pi f_2$:

$$K_1[\widetilde{y}_1(t) + \widetilde{y}_2(t)] = K_1[A_1\cos(\omega_1 t) + A_2\cos(\omega_2 t)]. \tag{3.6}$$

The 2^{nd} order term is the main contributor to the frequency mixing characteristic:

$$\Rightarrow K_2[\widetilde{y}_1^2(t) + 2\widetilde{y}_1(t)\widetilde{y}_2(t) + \widetilde{y}_2^2(t)] =$$

$$K_2\left[\frac{1}{2}A_1^2[\cos(2\omega_1 t) + 1] + A_1A_2[\cos((\omega_1 - \omega_2)t) + \cos((\omega_1 + \omega_2)t)] + \frac{1}{2}A_2^2[\cos(2\omega_2 t) + 1]\right]. \tag{3.7}$$

The 2^{nd} order term produces frequency components $2\omega_1$ and $2\omega_2$, which are harmonics of the input frequencies, but this term also produces the difference $\Delta\omega = \omega_1 - \omega_2$ and sum $\Sigma\omega = \omega_1 + \omega_2$ frequencies. All 3^{rd} order components can be similarly worked out, which yields:

$$\Rightarrow K_3[\widetilde{y}_1^3(t) + 3\widetilde{y}_1^2(t)\widetilde{y}_2(t) + 3\widetilde{y}_1(t)\widetilde{y}_1^2(t) + \widetilde{y}_2^3(t)] =$$

$$K_3\left[A_1^3\cos^3(\omega_1 t) + 3A_1^2A_2\cos^2(\omega_1 t)\cos(\omega_2 t) + 3A_1A_2^2\cos(\omega_1 t)\cos^2(\omega_2 t) + A_2^3\cos^3(\omega_2 t)\right]. \tag{3.8}$$

Further derivation of the 3rd order term will result in frequency components at the harmonics ω_1, ω_2, $3\omega_1$, and $3\omega_2$, but also at different combinations of the input frequencies, namely $2\omega_1 \pm \omega_2$ and $2\omega_2 \pm \omega_1$. This process goes on for higher orders of the Taylor expansion, generating more and more frequency components as the order increases. From looking at the frequency components generated by each order, it can be observed that even order terms produce integer multiples of the difference frequency $\Delta\omega$, and both the odd and even order terms produce the integer harmonics of the sum frequency $\Sigma\omega$, along with frequency components centred around these harmonics like $3\omega_1 \pm 2\omega_2$.

3.2 Results

To test the relevance of the mathematical model, a MATLAB script was made to generate all Taylor expansion components up to a certain order k, as in (3.5). The magnitude spectrum for $f_1 = 2.01\,\text{kHz}$ and $f_2 = 2\,\text{kHz}$ are generated, in which the maximum magnitude is normalized to 1, as shown in Fig. 3.2. The amplitude is set to $A_1 = A_2 = 2\,\text{V}$ and it is assumed that $K_n = 1$ for all $n > 0$. In practice, K_n will never be 1 for every order of the Taylor expansion and this is therefore not a realistic assumption. Please see Sec. 3.3.1 for a further exploration of this assumption. In the following, for lack of proper K_n values, we will generate the resulting spectrum for illustrative purposes only. Additionally, the generated output waveform is shown in the first row of Fig. 3.3. Also shown in the figure, in the second row, is the output waveform $\Psi(t)$ with the 1st-order components of the output waveform removed. In the third row, a 1st-order Butterworth filtered version of the output waveform $\Psi(t)$, with corner frequency at $f_c = 200\,\text{Hz}$ is shown.

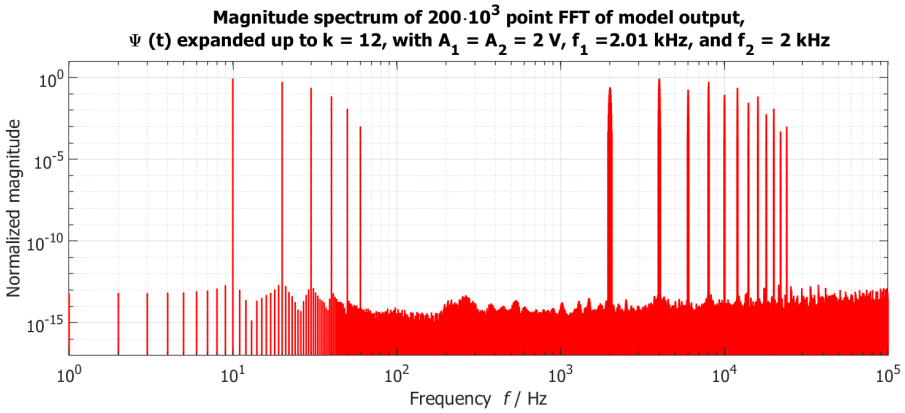

Figure 3.2: The 12th order generated magnitude spectrum for sinusoidal TIS with input frequencies $f_{1,2}$, normalized to the maximum. It is assumed that $K_n = 1$ for all Taylor expansion components.

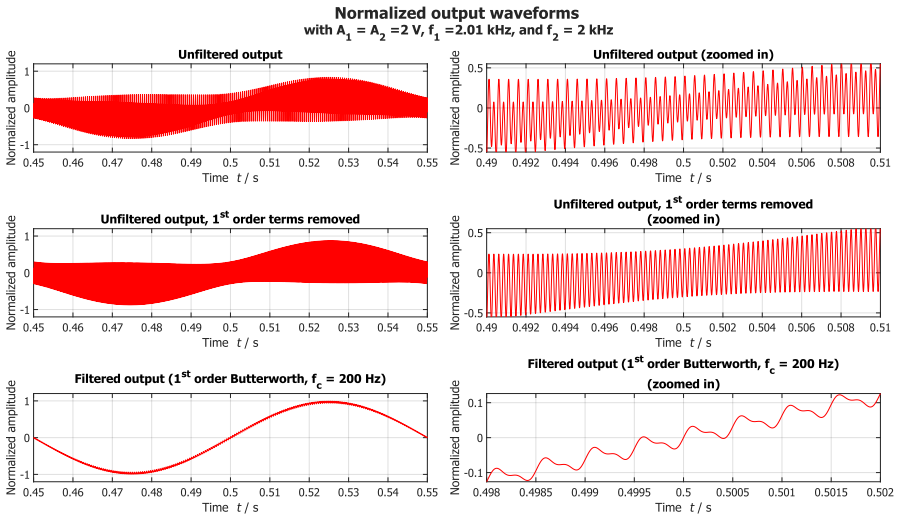

Figure 3.3: Normalized output waveform $\Psi(t)$ as generated by the proposed model for input waveform amplitudes $A_1 = A_2 = 2\,\text{V}$ and input frequencies $f_1 = 2.01\,\text{kHz}$ and $f_2 = 2\,\text{kHz}$.

3.2.1 Are measured nonlinear intermodulation products accurately represented by the proposed model?

Frequency inputs of [83] are replicated to create a direct comparison to the measured power-spectral density (PSD) of neuron responses to TIS. The PSDs for $f_1 = 5007\,\text{Hz}$ and $f_2 = 4997\,\text{Hz}$, $f_1 = 507\,\text{Hz}$ and $f_2 = 497\,\text{Hz}$, and $f_1 = 57\,\text{Hz}$ and $f_2 = 47\,\text{Hz}$ are generated, as shown in Fig. 3.4. The amplitude is set to $A_1 = A_2 = 750\,\text{mV}$ and it is again assumed that $K_n = 1$ for all $n > 0$. Fig. 3.4 shows the PSD results of the expansion up to order $k = 12$, overlaid on top of PSD measurement data from [83] with corresponding input frequencies. The results show that frequencies of intermodulation products created by the model accurately overlap with peaks in measured PSD data created by the neuron membrane frequency mixing mechanism (please see enlarged versions of the model output in Appendix A).

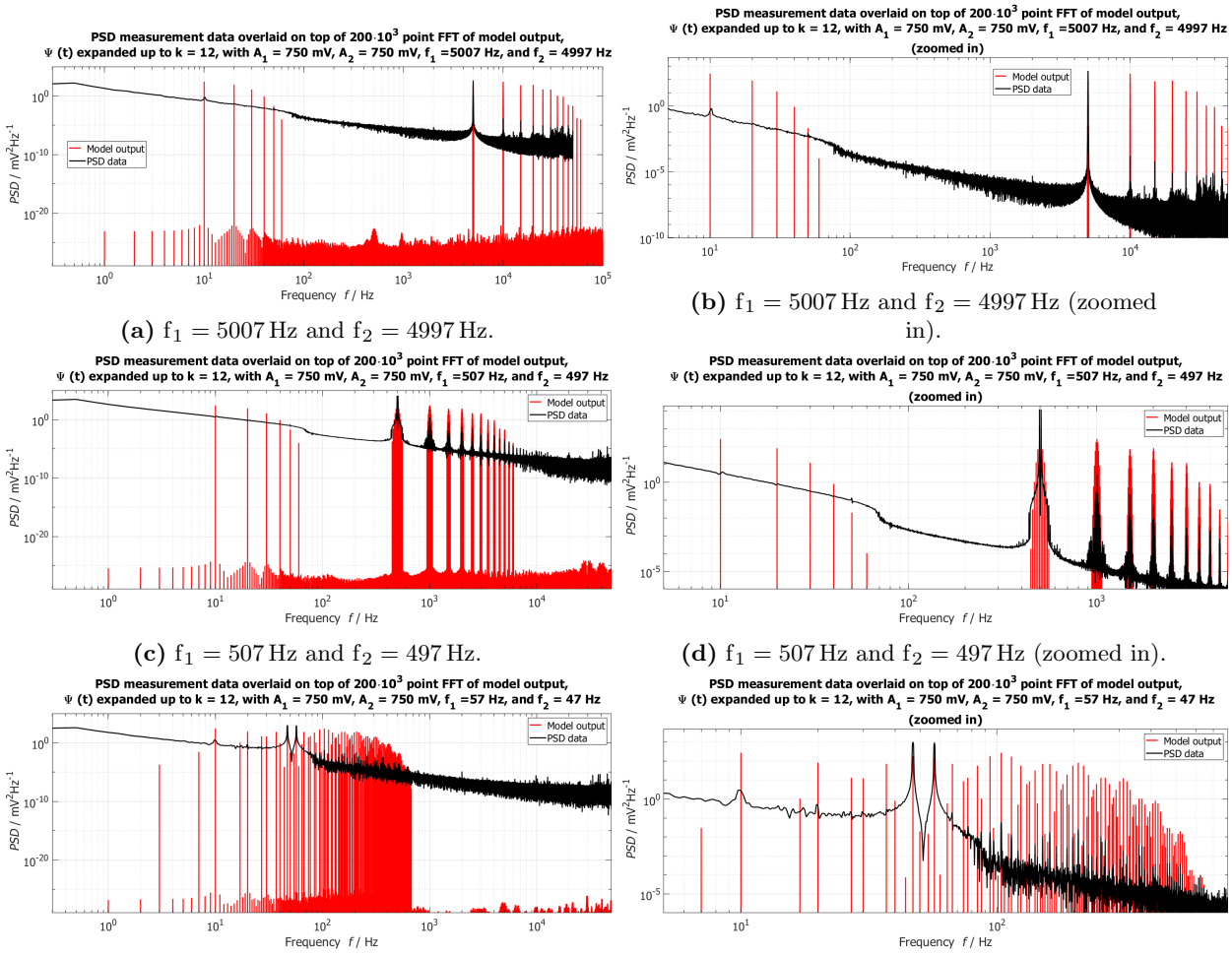

(a) $f_1 = 5007\,\text{Hz}$ and $f_2 = 4997\,\text{Hz}$.

(b) $f_1 = 5007\,\text{Hz}$ and $f_2 = 4997\,\text{Hz}$ (zoomed in).

(c) $f_1 = 507\,\text{Hz}$ and $f_2 = 497\,\text{Hz}$.

(d) $f_1 = 507\,\text{Hz}$ and $f_2 = 497\,\text{Hz}$ (zoomed in).

(e) $f_1 = 57\,\text{Hz}$ and $f_2 = 47\,\text{Hz}$.

(f) $f_1 = 57\,\text{Hz}$ and $f_2 = 47\,\text{Hz}$ (zoomed in).

Figure 3.4: The model PSD output with the nonlinear output waveform expanded up to the 12th order, overlaid on top of measured power spectral density data. Please see enlarged versions of these results in Appendix A. The low frequency intermodulation products at frequencies below 100 Hz are clearly visible, and high frequency intermodulation products accurately align with peaking events at similar frequencies as the measured PSD data.

3.2.2 Can the model predict the relevance of input waveform shape on power efficiency?

The shape of the waveform used for TIS has a large effect on the average power delivered to the neuron, but also the resulting spectral components from frequency mixing operations. By inserting various waveform shapes and frequencies into the proposed model, we can get a rough idea of the relative power distribution of frequency components and thus the relative energy efficiency of a waveform within some useful bandwidth defined by

the LPF-like behaviour of the neuron. This value can then be compared to the conventional sinusoidal inputs used in TIS. As an example, the normalized magnitude spectrum of a pair of zero-offset, periodic, rectangular waveforms is generated. The input frequencies are given by $f_1 = 2.01\,\text{kHz}$, and $f_2 = 2\,\text{kHz}$, assuming $K_n = 1$ for all Taylor expansion coefficients, like before in Fig. 3.2. The amplitude is the same as the sinusoidal waveforms, such that $A_1 = A_2 = 2\,\text{V}$. The spectrum is generated up to an order of $k = 12$, to generate all low frequency intermodulation products, at least up to 60 Hz. The result is shown in Fig. 3.5.

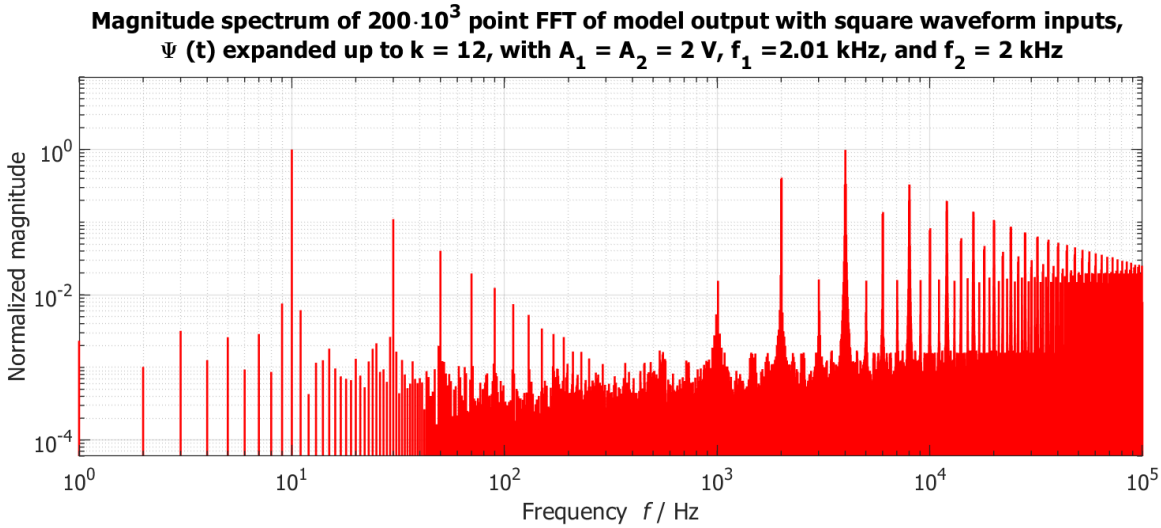

Figure 3.5: The 12th order generated magnitude spectrum for square waveform TIS with input frequencies $f_{1,2}$, normalized to the maximum. It is assumed that $K_n = 1$ for all Taylor expansion components.

The generated spectra show some clear differences. First of all, the baseline over the whole spectrum is about ten orders of magnitude higher than the spectrum in Fig. 3.2. Additionally, we can also conclude that the even-integer multiples of Δf get suppressed more than the odd-integer ones, in comparison to sinusoidal inputs. This should come as no surprise, as a perfect square wave contains only odd-integer harmonics. Additionally, we see a larger amount of high magnitude spectral components in the space between 10 Hz to 2 kHz than for the sinusoidal magnitude spectrum.

The only desired spectral components that are created by the frequency mixing mechanism in the neuron membrane are the components within the physiologically relevant bandwidth, specifically the bandwidth where vagus nerve cells are most sensitive, between DC and 50 Hz. All other components outside $BW_{VNS} = (0 \text{ to } 50)\text{Hz}$, which are components that are generated up to about $\frac{k}{2}\Sigma\omega$, do not beneficially add to the desired effect of stimulation. A relative efficiency for the sinusoidal input waveform can thus be defined in this rectangular window as:

$$\eta_x = \frac{\int_0^{BW_{VNS}} |\psi(\omega)| d\omega}{\int_0^{\frac{k}{2}\Sigma\omega} |\psi(\omega)| d\omega}, \text{ with } \Psi(t) \xrightarrow{\mathcal{F}} \psi(\omega). \tag{3.9}$$

The magnitude spectra are generated by a discrete FFT in MATLAB, which defines the magnitude of a data point at a resolution of 1 Hz. For the 12^{th} order model, and with $A_1 = A_2 = 2\,\text{V}$ the generated spectra resulted in an efficiency of $\eta_{sin} = 15\,\%$ for the sinusoidal input waveforms, and an efficiency of $\eta_{sqr} = 13\,\%$ for the square input waveforms.

3.3 Discussion

3.3.1 General considerations and model assumptions

In the resulting magnitude spectra of Fig. 3.4, the measured spectral components of neurons under influence of TIS in [83] accurately overlap with the predicted frequency components by the model. The main differences compared to the measured spectra is the lack of noise, a low-pass filter-like roll-off of –20 dB/dec at some very low cut-off frequency, and the scaling of individual Taylor expansion components K_n up to a relevant order k.

These scaling values can only be inferred from measurement; they directly reflect the nerve cell's preferential selection of certain frequency components for stimulation. As it is known that nonlinear distortion products exist on the spectrum, K_2 and all higher order scaling components, will need to have some nonzero value for which in general it will most likely hold that:

$$K_1 > K_2 > K_3 > ... > K_n. \tag{3.10}$$

Furthermore, the presented model is limited to using only two input waveforms, as that is conventional in TIS. A more general version of the model is versatile enough to predict the spectral components of any amount, shape or frequency of input waveform definition. Such a generalization is derived from (3.3) by replacing the sum of the two waveforms with the sum of an integer number of periodic and continuous input waveforms up to p:

$$\Psi(t) = \sum_{n=0}^{\infty} K_n \left[\widetilde{y}_1(t) + \widetilde{y}_2(t) + \cdots + \widetilde{y}_p(t)\right]^n = \sum_{n=0}^{\infty} K_n \left[\sum_{i=1}^{p} \widetilde{y}_i(t)\right]^n , \tag{3.11}$$

with

$$K_n = \frac{1}{n!} \left| \left(\frac{d^n \Psi(t)}{dt^n} \right) \right|_{t=0} . \tag{3.12}$$

Similar to before, the definition of $\widetilde{y}_i(t)$ can be entirely decided by the user to predict spectral components of the stimulation method. Various popular waveform shapes, like ramp-up or -down, triangular, exponential or rectangular, and various high or low frequencies can be directly put into the model to show the predicted outcome of stimulation.

However, this also addresses a limitation of the currently presented model: most *in-vivo* measurements of TIS use sinusoidal waveforms with only two unique electric fields, due either to preference, or happenstance availability. In [89] the effect of using pulse-width modulated (PWM) waveforms for TIS has been measured. This work at least provides credibility for the nonlinear electric field interactions happening within the neuron, but it is only a single instance of the use of a different waveform shape for TIS. Therefore, the presented results are only supported for the sinusoidal stimulation case with two electric field sources. A comprehensive testing of various other waveform shapes and frequencies is therefore desired to form a benchmark and test the generated results in comparison to various inputs.

An interesting observation from the presented results is the presence of a range of high order frequency components surrounding the root frequencies, which are visible in the results of Fig. 3.4c and in the measured results of earlier work [80, 83, 89] as spectral components that taper-off and surround the root frequencies $f_{1,2}$ and integer multiples of Σf. The influence of these components are very apparent at low frequencies (see Fig. 3.4f), as the higher order frequency mixing products start to move into the relevant stimulation bandwidth, below 200 Hz. It is therefore recommended to keep the root frequencies as far removed from the relevant bandwidth as possible, as its influence can directly affect the spatial selectivity of TIS, along with introducing unwanted spectral components at the focal point of stimulation.

This effect is visible due to the use of a fairly large 12^{th} order model. The choice of this order is not arbitrary, but if the input frequencies are sufficiently far removed from the relevant stimulation bandwidth, a minimally viable model up to second order would suffice, albeit very limited. Any lower order than second-order would be in opposition of the nonlinearity and frequency mixing products measured in earlier literature. Regardless, a higher order model will always provide more predictability and is therefore preferred.

3.3.2 The relevance of input waveform shape on spectral components and power distribution

The efficiency of both sinusoidal and square waveform inputs paint a fairly pessimistic picture of TIS; for input frequencies $f_1 = 2.01\,\text{kHz}$ and $f_2 = 2\,\text{kHz}$, with amplitudes $A_1 = A_2 = 2\,\text{V}$, the 12^{th} order model resulted in an efficiency of $\eta_{\text{sin}} = 15\,\%$ for the sinusoidal input waveforms, and an efficiency of $\eta_{\text{sqr}} = 13\,\%$ for the square input waveforms. However, for the case of sinusoidal inputs (as discussed in Sec. 3.1), the generated low frequency intermodulation products heavily depend on whether the Taylor expansion approximation is even or odd.

The efficiency results therefore also depend on the order at which it was simulated, but also on its input amplitudes, especially in the case where $A_{1,2} < 2\,\text{V}$. The efficiencies of various orders k of the Taylor expansion, and varying amplitudes of the input waveforms are shown in Fig. 3.6.

The efficiencies of sinusoidal inputs in Fig. 3.6a varies greatly depending on whether the chosen order is either even or odd, with the former producing better results. This is no surprise, as even orders of the Taylor expansion produce more low frequency intermodulation products around Δf that beneficially contribute to spectral components in the physiologically relevant bandwidth.

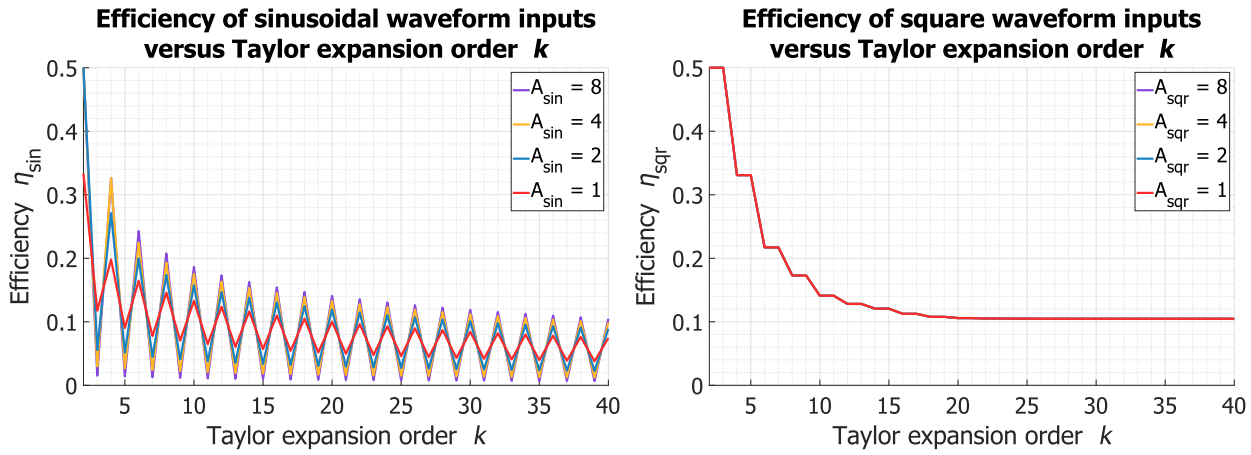

(a) Efficiencies for sinusoidal waveform inputs.

(b) Efficiencies for square waveform inputs (results overlap).

Figure 3.6: **(a)** The relative efficiency of sinusoidal input waveforms depends on both the Taylor expansion order, and the input waveform amplitudes. Odd orders of the Taylor expansion generally produce lower efficiencies in the case of sinusoidal inputs, as less intermodulation products are produced at frequencies in the bandwidth of interest, like Δf. **(b)** The relative efficiency of square input waveforms is insensitive to the Taylor expansion order being even or odd, or to the input amplitude. However, it is also similarly dependent on the value of the order.

The sinusoidal model is also dependent on input amplitude, as higher input amplitudes cause higher frequency intermodulation products to increase in magnitude inside the physiological bandwidth. In contrast, when the Taylor expansion order is odd, less beneficial components get added to the physiological bandwidth around Δf, reducing efficiency.

Regardless, both efficiencies show a similar efficiency trend, which tapers-off and reaches around 10 % efficiency for very high orders of the model. Assuming the voltage-gated ion channels in the neuron membrane influence the scaling factors K_n to reduce certain spectral components outside of the physiologically relevant bandwidth, these efficiencies could improve substantially. It is therefore desired to determine a relevant model order and related scaling factors for not only sinusoidal waveforms, but also various other waveform shapes to draw insightful conclusions regarding the relative efficiency of input waveforms.

Chapter 4

Simulations of the proposed power-efficient vagus nerve stimulator for temporal interference stimulation

4.1 Method

The proposed circuit architecture from Sect. 2.3.2 is implemented in Cadence Virtuoso for simulation. The function of the other digital- and power electronics-related system components in the total system architecture are idealized to focus on the analog analysis of the output stage. The circuit is implemented as shown in Fig. 4.1.

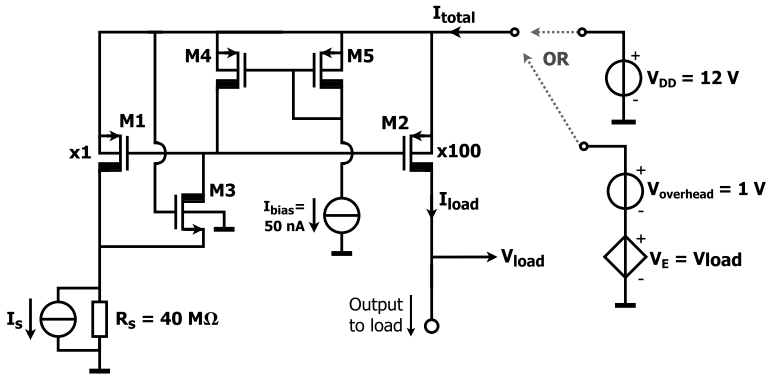

Figure 4.1: Output stage circuit as implemented in Cadence, with the supply either connected to an unregulated, constant voltage supply of 12 V, or to the idealized regulated supply.

The circuit design is made in a 12V (HV) 180nm CMOS TSMC technology, which requires two fingered devices as a minimum, for which the size ratio of the transistors is set at:

$$\frac{\mathrm{W}}{\mathrm{L}} = \frac{20\,\mu\mathrm{m}}{1\,\mu\mathrm{m}}, \tag{4.1}$$

for a single finger transistor width of $\mathrm{W_{fin}} = 10\,\mu\mathrm{m}$. These sizes are the same for all transistors in the following, unless explicitly mentioned otherwise. The required overhead voltage for the circuit is set to $\mathrm{V_{overhead}} = 1\,\mathrm{V}$. The used bias current is set at $\mathrm{I_{bias}} = 50\,\mathrm{nA}$. The input source current is imagined to be coming from a current-steering DAC, which can output in a full-scale range of (0 to 100)µA. The resolution of the I-DAC is assumed to be sufficiently high for the intended purpose. The source impedance is purely resistive, and has a value $\mathrm{R_s} = 40\,\mathrm{M\Omega}$, based on a required 3σ-accuracy of the load current. In other words, it is chosen such that the expected load current accuracy $\delta = 99.7\%$. To compare the performance of the proposed output stage to a conventional current mirror with an increased output resistance, a transistor-level design of the cascode current mirror is chosen as a benchmark. The design, that is implemented in the same 12V 180nm CMOS TSMC technology with the same $\frac{\mathrm{W}}{\mathrm{L}}$ size ratios, is shown in Fig. 4.2.

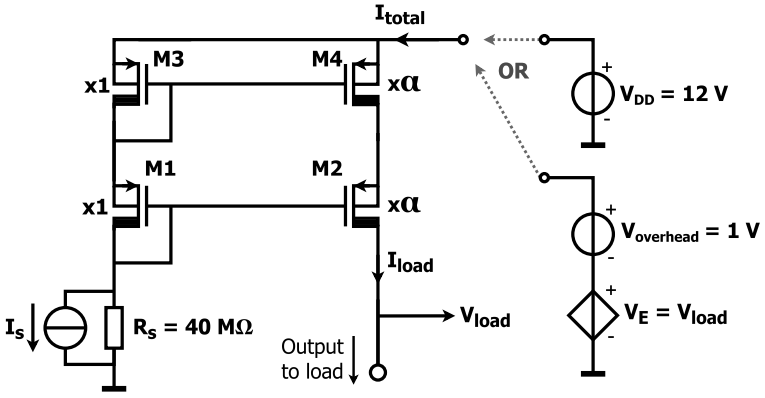

Figure 4.2: The cascode current mirror as implemented in Cadence, with the supply either connected to an unregulated, constant voltage supply of 12 V, or to the idealized regulated supply.

The cascode current mirror output transistors are sized up to a set multiplicity α. The performance of the cascode current mirror for an as-intended designed α-value of 100 is measured. In current mirrors intended for the purpose of current-mode stimulation, the α-value is often adjusted by trial-and-error to improve the performance. As such, the performance of the cascode current mirror, where the multiplicity is adjusted by trial-and-error to minimize error, is also measured. Additionally, the influence of using the proposed regulated supply on the cascode current mirror (both with and without an adjusted α-value) is measured, to provide a fair and comprehensive comparison.

4.1.1 Transient response test

The transient test features a custom transient pattern for the input source current, as shown in Fig. 4.3a. The load is purely resistive, and is defined by the estimation of the load impedance magnitude at relevant TIS frequencies; $R_{load} = 2R_{on} + |Z_{ETI}|$, where $R_{on} = 100\,\Omega$ and the electrode impedance $|Z_{ETI}|$ varies between a range of $0\,\Omega$ to $1\,k\Omega$. $|Z_{ETI}|$ is swept in steps of $50\,\Omega$, and a measurement of the total power spent P_{tot}, power absorbed by the electrode-tissue interface impedance P_{ETI}, total current I_{tot}, current trough the load I_ℓ, regulated supply output voltage V_{reg}, and load voltage V_ℓ is made at every step. The slew rate of the input current source is set at $1\,\mu A/\mu s$.

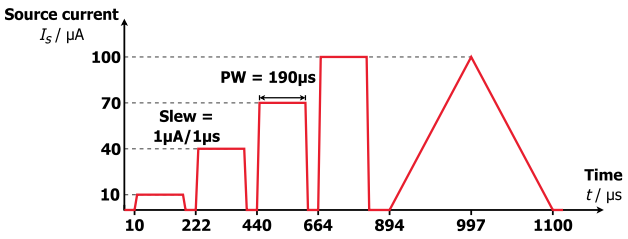

(a) Input waveform pattern.

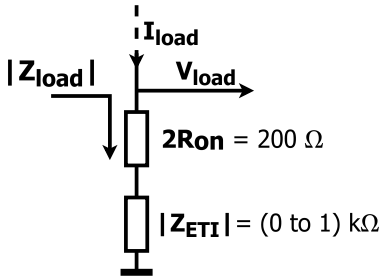

(b) Used load model in the transient test.

Figure 4.3: **(a)** The transient waveform, with indicated slew rate and pulse width PW. **(b)** The used load model is purely resistive, consisting of the on-resistance and estimated ETI impedance magnitude.

To fairly compare the output stages, variants of the cascode current mirror circuit are made, where it is either connected to a regulated supply or unregulated supply, or its multiplicity is manually adjusted (once) to match the required load current as best as possible over the whole range of impedances. All measured and calculated quantities of the transient tests, and their expressions are tabulated in Appendix B.

4.1.2 AC response and stimulation phases test

Bode plots of the magnitude and phase relationship of the output stage gain over multiple frequencies is measured for the linear ETI model. For the sake of convergence of the idealized regulated supply, the initial charge on the double-layer capacitance is assumed to be zero. The transient response to a typical square stimulation waveform is measured, to show the accumulation of charge at the end of a stimulation phase.

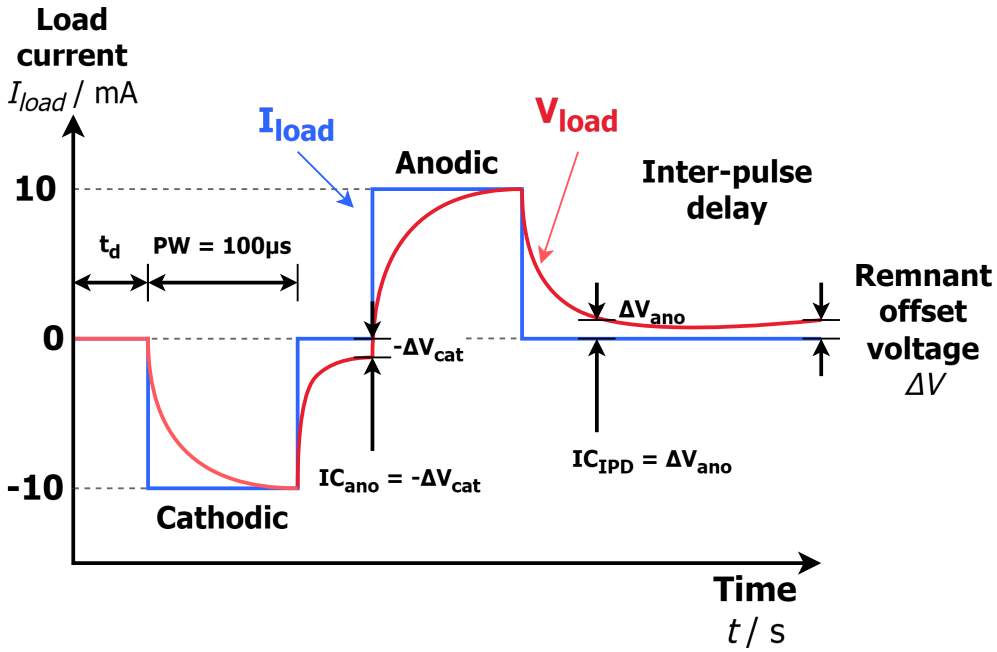

Figure 4.4: The phases of stimulation, with the separately simulated remnant offset voltage across the electrodes counted up at the beginning of the next phase as an initial condition.

The employed transient consists of a cathodic phase, into an anodic phase with small delay, into the Inter-Pulse Delay (IPD) period of the stimulation curve. The pulse-width and input current amplitude for both the cathodic and anodic phase are set at $t_{pulse} = 100\,\mu s$ and $I_s = 100\,\mu A$ respectively. The delay between the start of stimulation to the initial falling edge of the cathodic phase, and the delay between the rising edge of the cathodic phase and the rising edge of the anodic phase is set at $t_{delay} = 5\,\mu s$. The IPD is a phase where the input current amplitude is zero, which is held for an equivalent amount of time as one pulse width, as such, $t_{IPD} = 100\,\mu s$.

The remnant offset voltage at the end of a separately simulated cathodic phase is added to the beginning of a separately simulated anodic and IPD phase, and the remnant voltage at the end of the IPD phase is noted for a worst-case $R_{tis} = 1\,k\Omega$, and double-layer capacitance values of either $C_{dl} = 1\,\mu F$, $C_{dl} = 50\,\mu F$, or $C_{dl} = 100\,\mu F$.

The remnant voltage at the end of a phase, after the small t_{delay}, is used as an initial condition for the charge on the double-layer capacitance in the next phase, as shown in Fig. 4.4. The output stage then either sources current from the 'negative' side, as in the anodic phase, or not at all, as in the IPD phase.

4.1.3 Crosstalk test

Two output stages are used in separate channels with a H-bridge architecture, connected to each other via a network of ETI impedances to model crosstalk, as shown in Fig. 4.5. The reference current source outputs a rectified sinusoidal signal with an amplitude of $100\,\mu A$. The double-layer capacitance is set to a value of $C_{dl} = 50\,\mu F$, and is split between the sourcing and sinking side switches such that the total equivalent double-layer capacitance is the same (the series connection of two $2C_{dl}$ capacitors is equivalent to a single capacitor with value C_{dl}). Tissue impedance is modelled as purely resistive elements, where the distances between electrodes decides the value of the resistance. The maximum tissue resistance in the network has a value of $100\,k\Omega$, whereas the minimum tissue resistance in the network is set to $100\,\Omega$. The focal point of stimulation has a constant resistance of $100\,\Omega$.

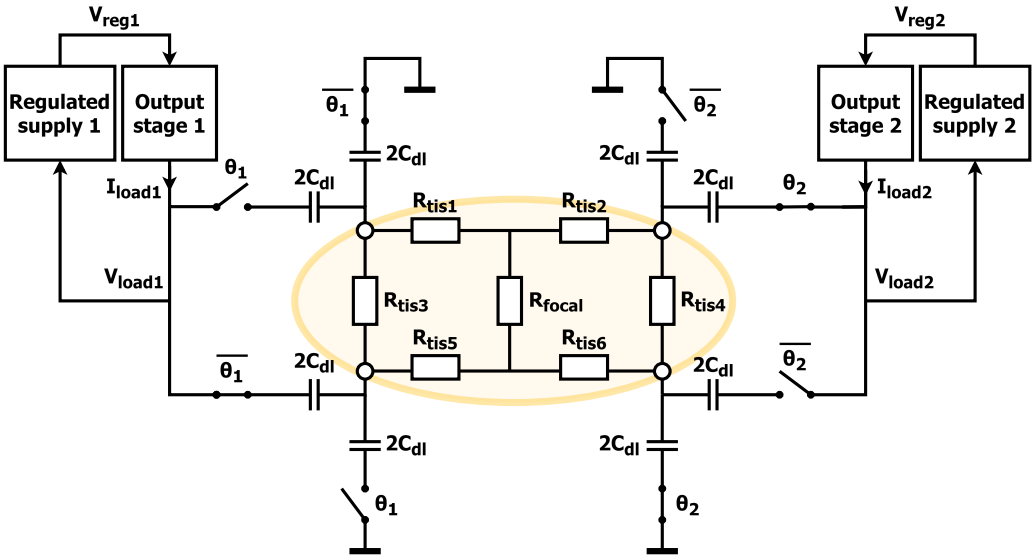

Figure 4.5: The impedance network to measure the effect of crosstalk.

The effects of stimulation without charge storage of the membrane, when the network of impedances is purely resistive, will also be recorded to compare the charge accumulation of tissue stimulation under influence of TIS. In this case, the double-layer capacitances of Fig. 4.5 are removed, and the H-bridge switches are directly shorted to the resistive network.

4.2 Results

4.2.1 How does the output stage perform in terms of power efficiency, current error and area?

A view of the plotted output results in Cadence is shown in Fig. 4.6. The plots show the result of a transient simulation run for the proposed output stage with regulated supply. To draw meaningful conclusions from these results, they will be individually analysed in the following sections (please see Appendix B for more details on the generated data and data processing featured in this report).

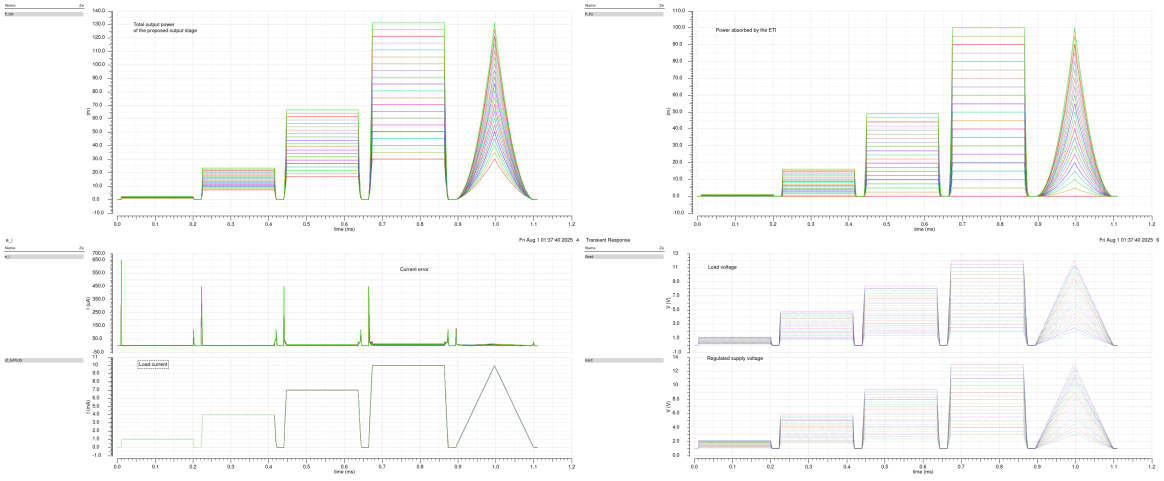

Figure 4.6: A view of the plotted outputs in a simulation of the proposed output stage with regulated supply.

Total average power, peak total power and stimulation efficiency

To assess the power-efficiency of the output stage variants, the average total power spent, peak total power spent, and the fraction of the average total power absorbed by the ETI versus ETI impedance magnitude is shown in Fig. 4.7.

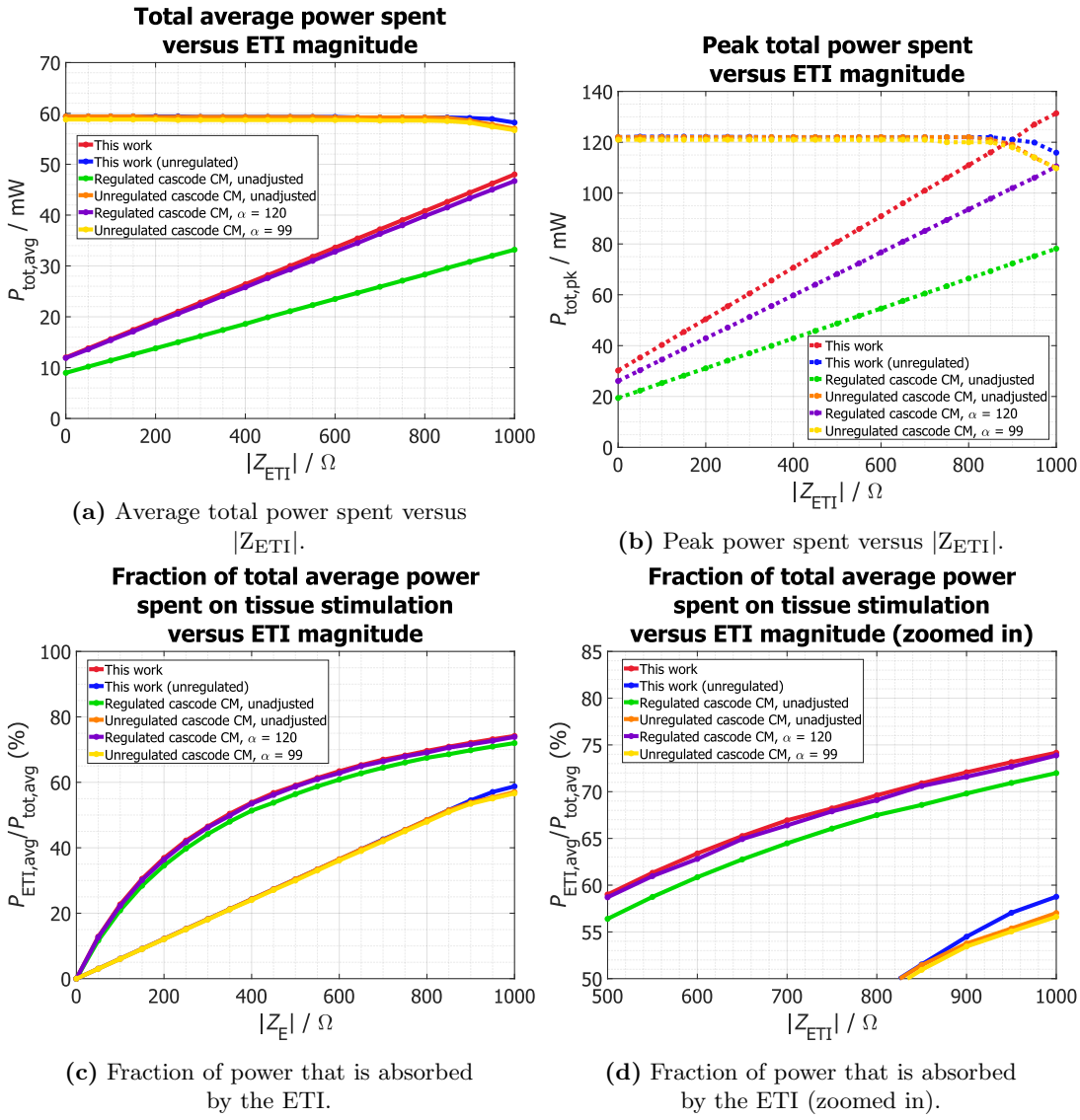

(a) Average total power spent versus $|Z_{ETI}|$.

(b) Peak power spent versus $|Z_{ETI}|$.

(c) Fraction of power that is absorbed by the ETI.

(d) Fraction of power that is absorbed by the ETI (zoomed in).

Figure 4.7: **(a)** & **(b)** Both the average total power spent and peak total power spent show that regulated supply variants scale their total power linearly based on demand, whereas the power consumption of unregulated supply variants stays fairly constant. **(c)** & **(d)** The fraction of the total power spent on the ETI is a measure of the efficiency of stimulation. The efficiency of regulated supply variants is significantly higher than unregulated variants, as only the strictly required amount of power is used for stimulation and operation of the output stage.

The presented results confirm earlier predicted observations as discussed in Sec. 1.3.2. The total power of output stages with a regulated supply changes linearly based on the demand, whereas output stages with an unregulated supply feature roughly constant high average power usage. The fraction of the power from the supply that ends up at the ETI is in essence a measure of the efficiency of stimulation, as:

$$\eta_{stim} = \frac{P_{ETI}}{P_{sup}}. \tag{4.2}$$

This efficiency can be found to be consistently much higher than the unregulated variants, and also confirms the expected behaviour and scaling of the total power and power efficiency in Fig. 1.18b of Sec. 1.3.2.

Average and peak load current error

To assess the accuracy of the output stage variants, the absolute average current error $|\epsilon_{\mathrm{i,avg}}|$ and absolute peak current error $|\epsilon_{\mathrm{i,pk}}|$ are shown in Fig. 4.8. The absolute current error is defined as the difference between the target current and the measured load current. As the average can paint a fairly distorted picture of the actual load current accuracy, the peak current error at every tested impedance magnitude is also shown.

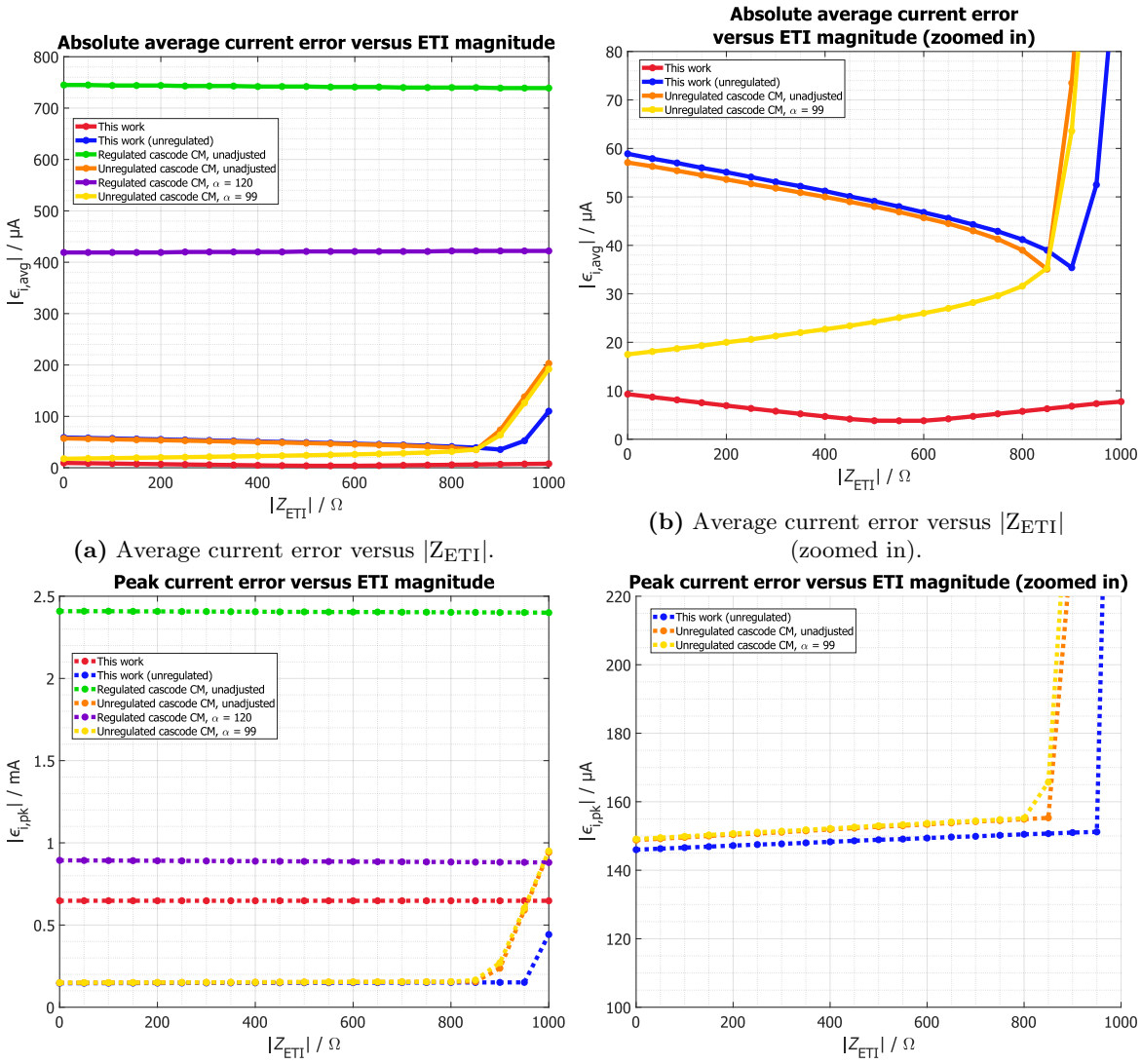

(a) Average current error versus $|\mathrm{Z_{ETI}}|$.

(b) Average current error versus $|\mathrm{Z_{ETI}}|$ (zoomed in).

(c) Peak current error versus $|\mathrm{Z_{ETI}}|$.

(d) Peak current error versus $|\mathrm{Z_{ETI}}|$.

Figure 4.8: **(a)** & **(b)** Average current error for unregulated output stage variants rises at higher impedance magnitudes due to small voltage drops on the output transistors, effectively reducing load current. **(c)** & **(d)** The peak current similarly is worse for regulated output stage variants. Peak current errors happen only between transitions between stimulation pulses.

The average current error for the proposed output stage architecture with regulated supply falls far below the predicted 30 µA bound set by the 3σ-accuracy requirement, only reaching a maximum of about 10 µA average current error. Regulated cascode architectures feature much worse accuracies than their unregulated counterparts, which stay fairly accurate until large ETI values are reached. Similarly, comparatively large peak current errors are shown for regulated output stage variants. These errors mostly happen at the rising edges of switching points between pulses (as shown Fig. 4.9), exacerbated by the high gain of the control required for setting the value of the regulated voltage supply.

Area taken up by transistors

The area taken up by only the transistor sizes A_t (not accounting routing of connections) for all output stage variants, and their respective area proportionalities, are recorded in Table 4.1.

	Active area A_t / µm^2	Area proportionality
This work, regulated, $\alpha = 100$	2080	α+4
This work, unregulated, $\alpha = 100$	2080	α+4
Cascode CM, regulated, $\alpha = 120$	4840	2α +2
Cascode CM, unregulated, $\alpha = 99$	4000	2α +2
Cascode CM, regulated, unadjusted	4040	2α +2
Cascode CM, unregulated, unadjusted	4040	2α +2

Table 4.1: An account of the area occupied by the output stage transistors.

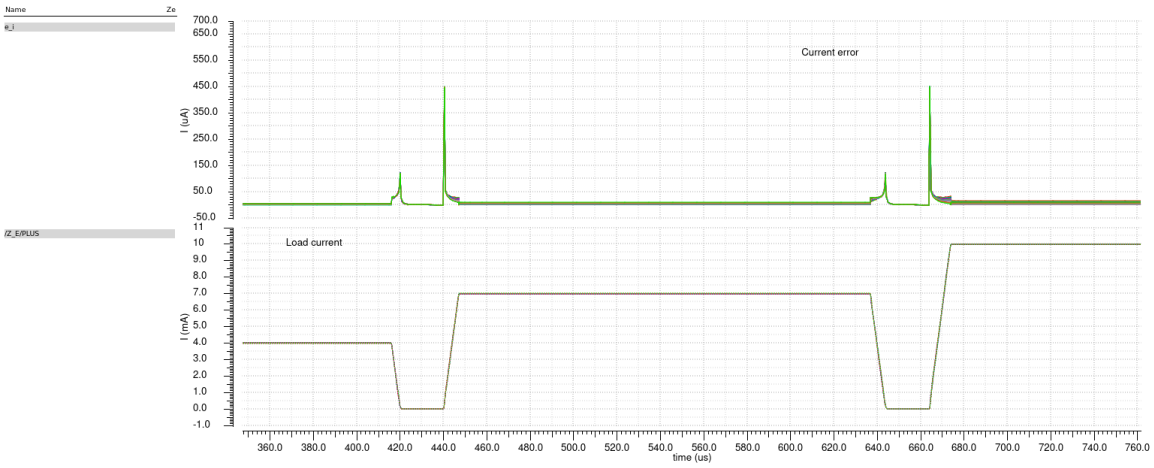

Figure 4.9: A view of the Cadence simulation output, with at the top a graph of absolute current error versus time, and at the bottom a graph of load current versus time. The current error for regulated supply variants shows spiking behaviour during transitions between pulses.

Weighing the performance metrics in a Figure of Merit

To weigh the significance of the presented results, a figure of merit (FOM) is defined as:

$$\mathrm{FOM} = \frac{\eta_{\mathrm{stim}}}{\mathrm{P_{tot,avg}}|\epsilon_{\mathrm{i,avg}}|\mathrm{P_{tot,pk}}|\epsilon_{\mathrm{i,pk}}|\mathrm{A_t}}, \tag{4.3}$$

where η_{stim} is the fraction of the total power spent on stimulation (in other words, the efficiency of stimulation), $\mathrm{P_{tot,avg}}$ is the total average power spent by the output stage circuit, $|\epsilon_{\mathrm{i,avg}}|$ is the average current error, $\mathrm{P_{tot,pk}}$ is the peak total power spent by the output stage circuit, $|\epsilon_{\mathrm{i,pk}}|$ is the peak current error, and $\mathrm{A_t}$ is the active area taken up by the transistor sizes alone.

The FOM is therefore a measure of the highest power efficiency, for the least power spent, having the least current error and occupying the least amount of area, for varying ETI magnitudes, as shown in Fig. 4.10. The suggested output stage with regulated supply of Sec. 2.3.2 consistently scores higher than all other output stages for the transient tests, closely followed by its unregulated variant and the unregulated cascode current mirror with adjusted multiplicity. Regulated versions of the cascode current mirror do not have very high values of the FOM, which could be caused by the set value of the overhead voltage that is too low for properly biased operation of the architecture. If increased, this would in turn increase accuracy of these stages. However, this would also mean that more power would be dissipated by the output current source overhead, resulting in an unappealing trade-off.

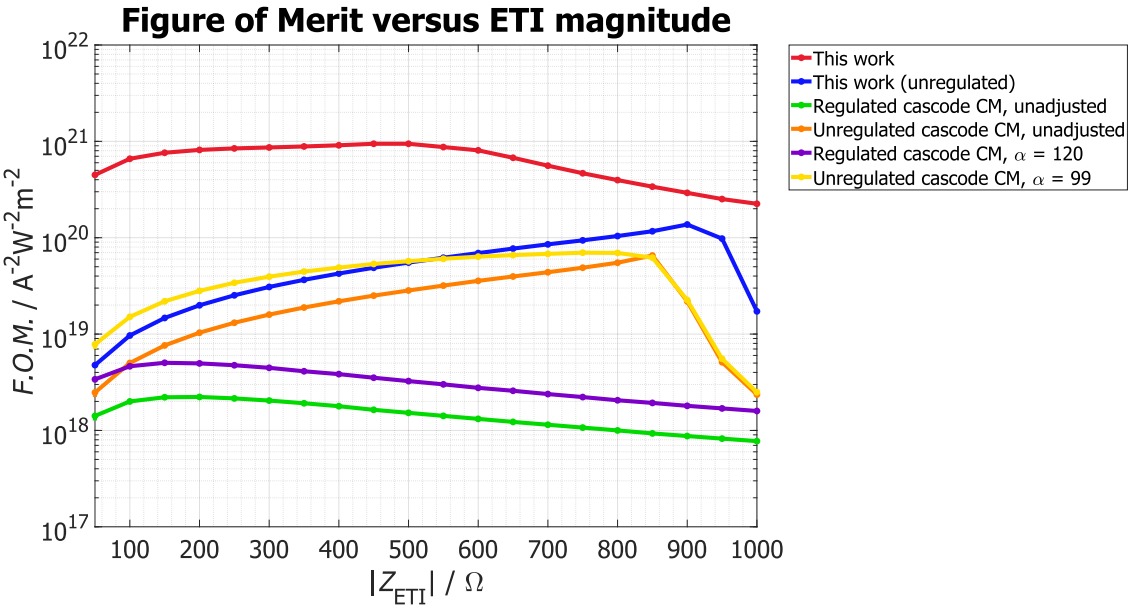

Figure 4.10: A logarithmic plot of the FOM versus ETI impedance magnitude.

4.2.2 Can the output stage handle fast transients and remnant charge in various phases of stimulation?

Bode plots of the magnitude and phase relationship

The Bode plots of the magnitude and phase relationship of the current gain for various input frequencies is shown in Fig. 4.11. After an initially low gain at low frequency, the gain stays constant up to a few tens of kHz, as expected. There is a pole at a very small frequency, around 8 mHz, which is introduced by the double-layer capacitance (possibly in combination with some high resistance around 420 kΩ). There is also a dominant pole at about 61 kHz, which is most likely introduced by the large multiplicity of output transistor M2, and causes a first-order roll-off. The gate-source capacitance $\mathrm{c_{gs}}$ of HV transistors is larger than their LV counterpart of similar size (due to differences in oxide thickness, for compliance and safety). Thus, the large multiplicity of the output transistor only adds to this equivalent capacitance at the output, which severely limits the bandwidth of the output. It can be assumed that the ETI resistance (beyond the pole created by the double-layer capacitance) is around 1.2 kΩ, which means the added capacitance of the output transistor can be estimated to be around $\mathrm{C_{out}} = 2\,\mathrm{nF}$.

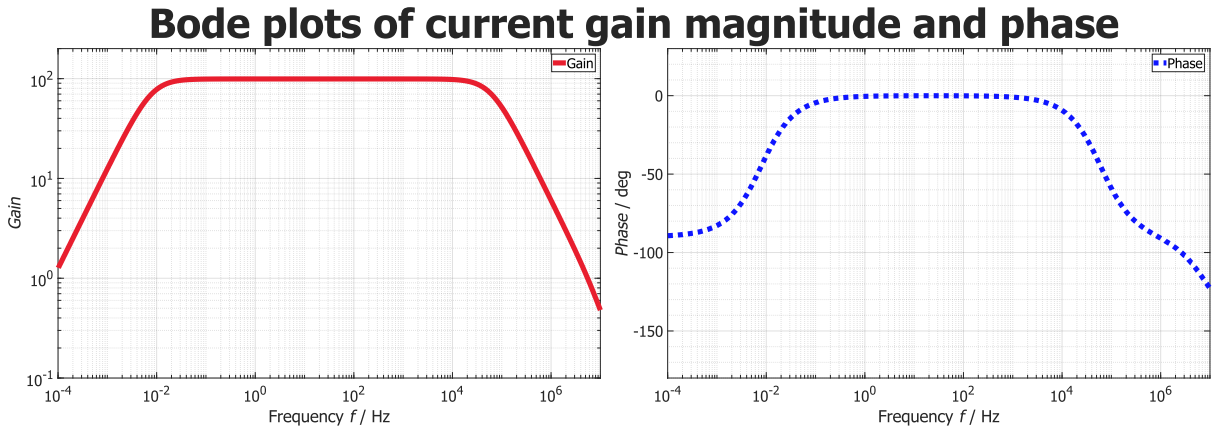

Figure 4.11: The AC simulation results.

Remnant charge during different phases of stimulation

The remnant voltage across the electrodes, as indicated by the voltage across the ETI at the end of the IPD ΔV, is shown in Fig. 4.12. Please see Appendix B for the full stimulation waveform measurement results.

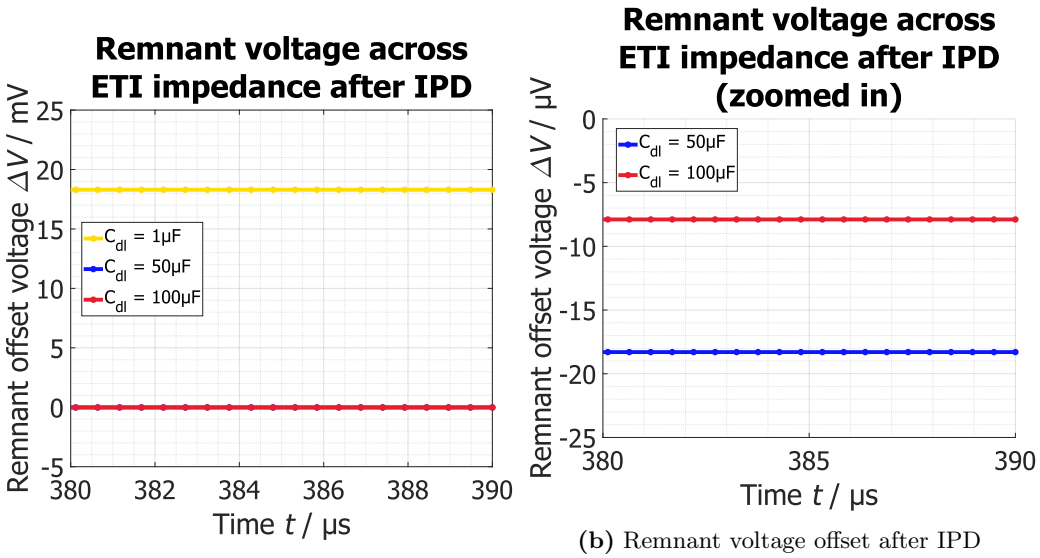

(a) Remnant voltage offset after IPD.

(b) Remnant voltage offset after IPD (zoomed in).

Figure 4.12: The remnant voltage across the electrodes, for high values of the double-layer capacitance, are relatively much lower than for the case where $C_{dl} = 1\,\mu F$, but the difference between a double-layer capacitance of 50 µF and 100 µF is negligibly small.

The results show that the output stage carries a remnant charge at the end of a stimulation waveform, varying in amount by the value of the double-layer capacitance. The proposed output stage, and other conventional output stages for that matter, are dependent on large values of the double-layer capacitance to reduce remnant offset voltage across the electrodes, if charge balancing methods are not applied. A charge-balancing method for TIS would steer the remnant accumulated charge within safe values, with a certain amount of accuracy.

4.2.3 Can the output stage produce the necessary output for temporal interference stimulation?

Spatial selectivity and energy efficiency of stimulation when output electrodes are close together

The resulting crosstalk currents and accumulated voltage on the electrodes in the situation where the channel electrodes are close together are shown in Fig. 4.13. The crosstalk impedance network is characterized by an $R_{focal} = 100\,\Omega$, $R_{tis_{1,2,5,6}} = 100\,\Omega$, $R_{tis_{3,4}} = 100\,k\Omega$, and $R_{on} = 100\,\Omega$, and the equivalent double-layer capacitance value is set at $C_{dl} = 50\,\mu F$. The frequencies of the rectified sinusoidal input currents are $f_1 = 2.01\,kHz$ and $f_2 = 2\,kHz$, with an amplitude of $100\,\mu A$.

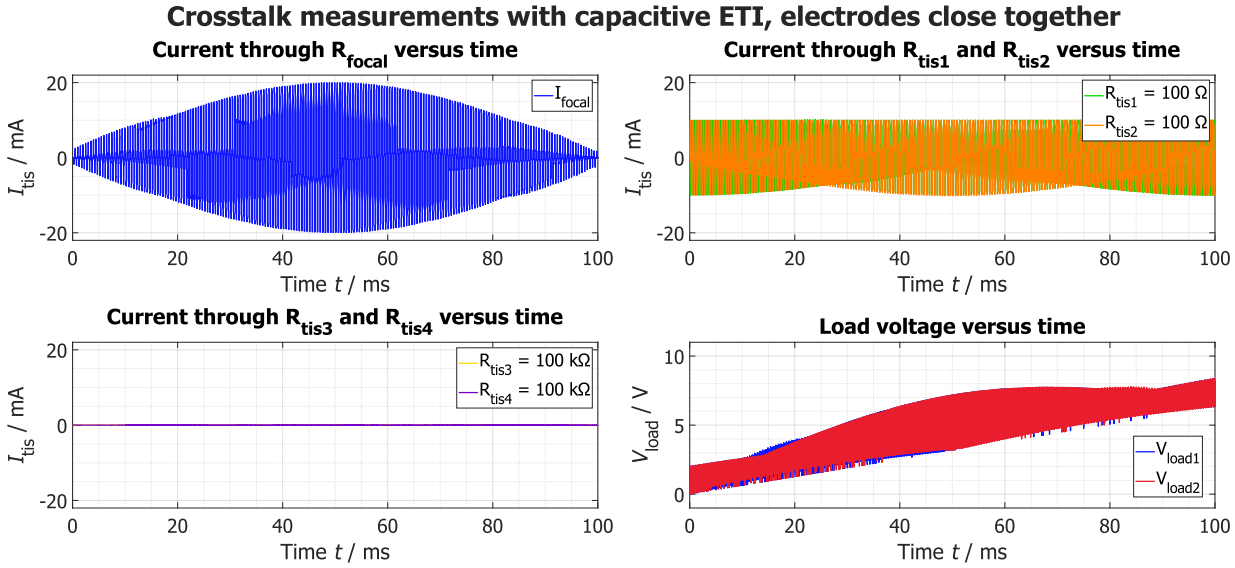

Figure 4.13: The results of the crosstalk setup, where output electrodes are close together, as illustrated in Fig. 4.14. The current through the focal point shows an amplitude modulation that is characteristic to TIS. The load voltage over this time period increases, due to charge storage in the neuron membrane, illustrating the need for charge balancing circuitry.

From the results it can be seen that the circuit is capable of generating the amplitude modulated waveform when the electrodes are close together, which is crucial for the operation of the circuit for TIS. However, the focal point of the stimulation is now severely stretched out over a larger section of the nerve as shown in Fig. 4.14, which reduces spatial selectivity.

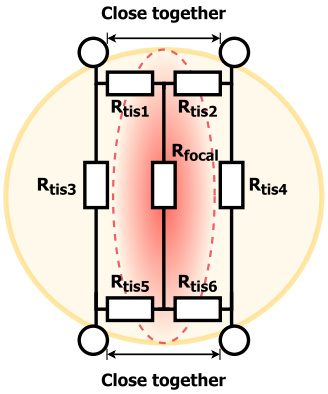

Figure 4.14: The electrodes are close together, which increases power efficiency. The output stimulates a large area of the nerve as a consequence, which reduces spatial selectivity.

The load voltages of each channel also show an accumulation of charge, as the charge is not actively balanced out in the presented output stage design. The crosstalk results in the case the network impedances are purely resistive, are shown in Fig. 4.15.

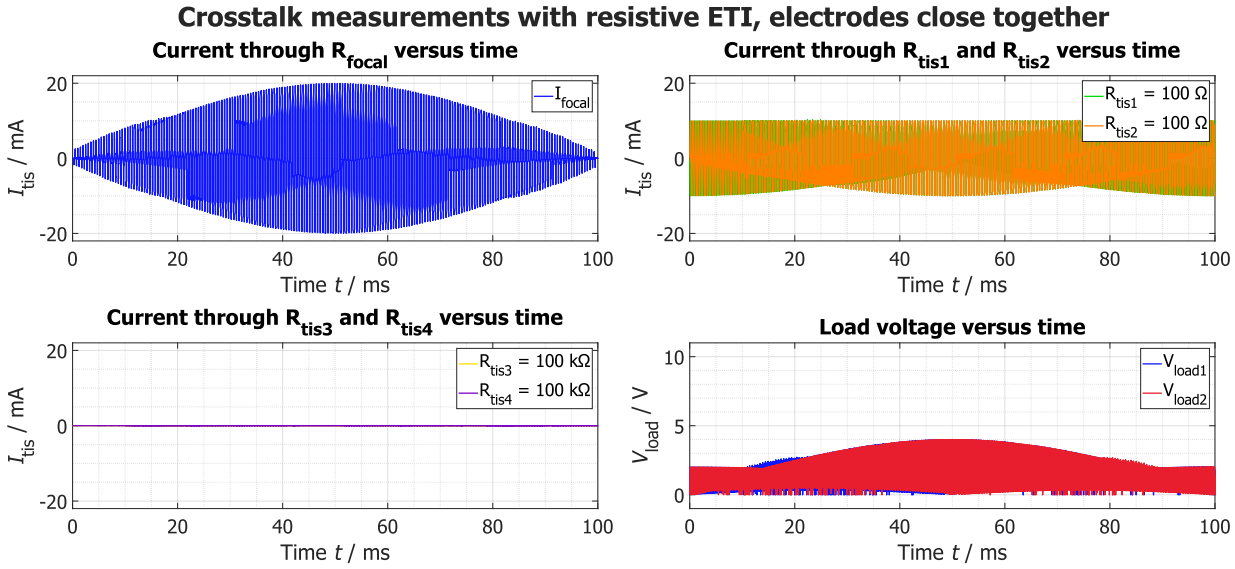

Figure 4.15: The results of the crosstalk setup when the output electrodes are close together, with only resistive elements in the impedance network. The ETI does not store charge in this case.

Spatial selectivity and energy efficiency of stimulation when output electrodes are far apart

The resulting crosstalk currents and accumulated voltage on the electrodes in the situation where the channel electrodes are far apart are shown in Fig. 4.16. The crosstalk impedance network and input parameters are similar to before, but now feature tissue resistance values between electrodes equal to $\mathrm{R}_{\mathrm{tis}_{1,2,5,6}} = 100\,\mathrm{k}\Omega$, and $\mathrm{R}_{\mathrm{tis}_{3,4}} = 100\,\Omega$, to model the different physical distances between the electrodes.

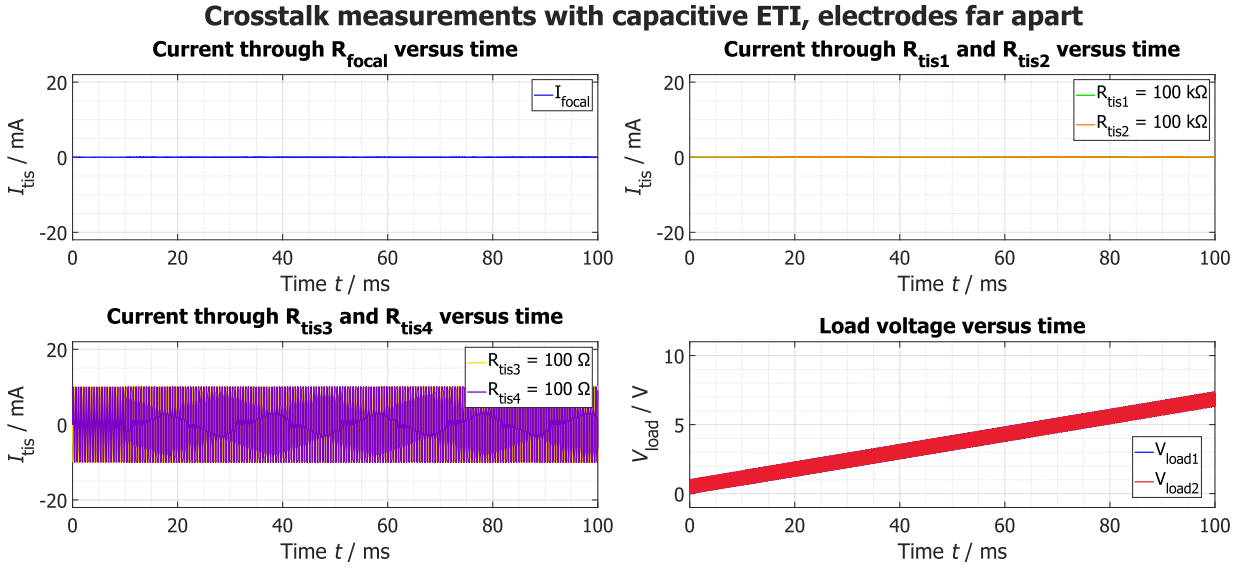

Figure 4.16: The results of the crosstalk setup, where output electrodes are far apart, as illustrated in Fig. 4.17. Despite the lack of an amplitude modulated waveform at the focal point, the output electrodes still build up a charge, as can be seen in the load voltage measurements.

From the results it can be seen that the circuit is not capable of generating a sufficiently amplitude modulated waveform at the intended focal point when the electrodes are far apart, which limits the power-efficiency and spatial selectivity, as neural cell stimulation sensitivity is highly dependent on the nonlinear frequency mixing components that are created by the amplitude modulated waveform at the focal point of stimulation.

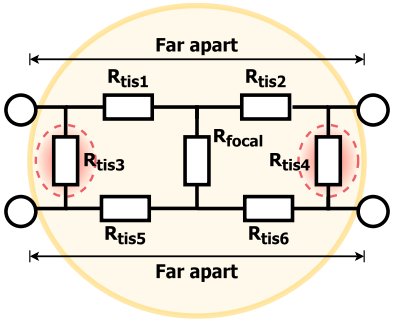

Figure 4.17: The electrodes are far apart, which decreases spatial selectivity and power efficiency by stimulating off-target neurons at the periphery of the nerve.

The load voltages show a similar build-up of charge as seen in the case when the electrodes are close together, for the same reasons as mentioned before. The crosstalk results, in the case the network impedances are purely resistive, are shown in Fig. 4.18.

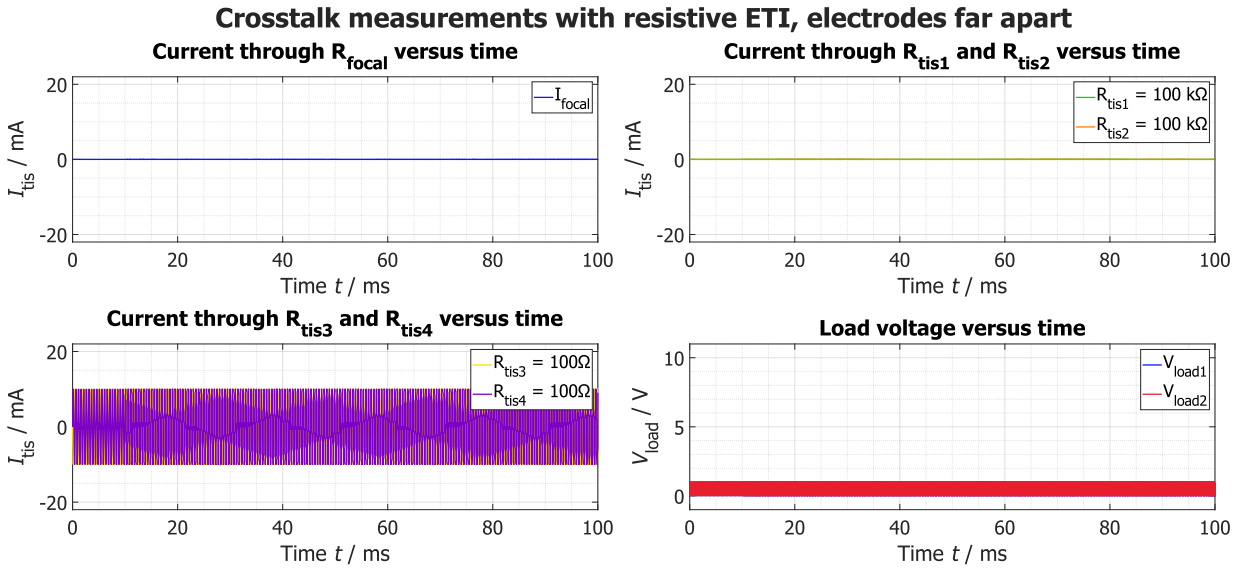

Figure 4.18: The results of the crosstalk setup when the output electrodes are far apart, with only resistive elements in the impedance network. The ETI does not store charge in this case.

4.3 Discussion

4.3.1 General considerations and simulation assumptions

The presented results assume some fairly broad system characteristics, which have profound effects on the performance of a given output stage. The chosen variables, like sizes of resistors, the value of the double-layer capacitance, and overhead voltage, have been kept constant to eliminate as many variables as possible for a fair comparison of the output stage variants. Regardless, some of the assumptions and their effects are listed and discussed in the following:

- **Size of source resistance and proper corrective negative feedback:** The required source impedance magnitude was estimated in Sec. 2.3.2 for a required accuracy δ of the load current, resulting in a large source resistance value of 40 MΩ. In corrective negative feedback design, a circuit would not have to deal with relying on source or load impedance magnitudes when the source-to-load transfer is unilateral. The accuracy of such an amplifier is then defined by the servo function of the asymptotic gain model (but only by approximation, as the direct source-to-load transfer influences the gain accuracy). The servo function is dependent on the loopgain, which in turn will need to be maximized for greater midband accuracy of the

amplifier. Maximizing loopgain further improves other performance aspects, like the signal-to-noise ratio and bandwidth of the amplifier output. When there is a source dependency, as in the presented current mirror output stage circuits, increasing loopgain ad infinitum will lead to an asymptotic gain as presented in (2.28). This means indirect feedback amplification, and the ideal accuracy of the source-to-load transfer, need to further be defined by an additional overall amplifier accuracy δ, based on the dependency of the source impedance. This is not ideal, and further circuit analysis has to be performed for the improvement of indirect feedback output stages, which may turn out to be in favour of direct feedback approaches if the added overhead associated with its current sensing element can be sufficiently reduced.

- **Sizes and multiplicity of transistors:** The selected sizes of output stage transistors are chosen in a rather arbitrary fashion, focusing on the initial analysis and response of neural stimulator output stages with a regulated supply. Especially in the case of HV CMOS technologies, overly large sizing is not desired. Large sizes result in enormous area consumption from isolation rings associated with HV technologies, further relating to reductions in bandwidth by the added output capacitance. Additionally, the multiplicity $\alpha = 100$ was arbitrarily chosen as a compromise for the fraction of the power spent on the source branch versus its increase in area. An ideal multiplicity, in the context of its associated dynamic effects and sizing of HV transistors, is yet to be determined.

- **Controller and biasing design:** The presented controller of the output stage is fairly minimal; only a single amplifier stage, featuring a three terminal CS device, is used to provide the necessary function of the controller when connected to the regulated supply. The controller E1 of Fig. 1.54 functions much like a conventional operational amplifier with a voltage output character, which could be implemented in a later iteration of the output stage design. Furthermore, the presented biasing scheme of the CS stage leaves a lot to be desired, as the implemented biasing source introduces a small offset at the input of the controller, which is counter to the intended outcome of biasing. Additionally, the biasing voltage V_{GS} of the MOSFET device is in essence set by the drain-source voltage of M1, and is as such (much) higher than it strictly needs to be. However, this does have the effect that the output current will always be maximized for a given regulated supply voltage, clipping the output to an accurate current gain value if source resistance is big. The resulting effect is much like 'normal' positive feedback, as presented in Sec. 1.3.3. If the output quantity is known to clip the set supply voltage, the presented design of positive feedback amplifiers might be preferred, but such a circuit will suffer from runaway amplification that is dependent on initial conditions if not checked by the regulated supply or other external circuitry.

- **Convergence issues:** In the presented design, the initial charge on the double-layer capacitance was assumed to be zero. This assumption is fairly unrealistic, as charges of electrodes will always require to 'settle' at an equilibrium when introduced to an electrolytic medium, but the assumption is not far off. Regardless, the ideal capacitance that is added to model the double-layer capacitance at the beginning of an initial operating point simulation is seen as an 'open' connection. This immediately causes a maximization of the regulated supply output, causing a dominant positive feedback loop that effectively locks the amplifier in a non-ideal state. In reality, there will be some faradaic impedance that allows for small frequency currents to be passed, albeit such that the load voltage is severely limited in this case. A solution to these issues in implementation, is the addition of either an initialization circuit, or a slow ramp-up of the required supply voltage by means of a soft-start circuit.

- **Process, threshold voltage and temperature variations:** The presented results are only validated in nominal process corners, at a temperature of 27 °C. Power consumption, intrinsic transistor capacitances, load current accuracy, transistor area, and other relevant performance metrics all depend on the matching of individual transistors and the effects of variations in process corners for various temperatures. This is especially relevant when considering the implementation of a device in the human body, which could feature core temperatures of up to 38 °C. The effects of process corners, matching offsets, and temperature should thus be comprehensively validated.

- **Potential improvements on the feedback for the regulated supply voltage:** The proposed feedback of the regulated supply continuously changes the regulated supply voltage to meet the demand. Another avenue for improvement of this feedback loop could be a change of the measured quantity, or a change of the continuous character of the presented supply regulation. For example, a periodic measurement of the ETI impedance can be taken in a calibration test phase before every stimulation cycle, which would determine a sufficiently high supply voltage for the measured impedance, and held for an extended amount of time. The regulated supply voltage can then operate at a much lower frequency than the used sampling frequency for matching the stimulation waveform. The design of such a system in the context of neuromodulation circuits has not been properly explored yet.

Chapter 5

Conclusion

This work has presented advancements in the design of temporal interference-based neural stimulators, particularly in the areas of electrophysiological modelling of neuron responses under influence of temporal interference stimulation, and the design of power-efficient neurostimulator systems.

The proposed model accurately predicts intermodulation products created by the nonlinear frequency mixing phenomena of neural responses under influence of TIS, validated by comparison to measurements of these intermodulation products in literature. The relevance of stimulation waveform shape was posited to be definable, to some degree, by the power distribution of the created spectral components, for which it was seen that the predicted relative efficiencies of sinusoidal and square input waveforms are highly dependent on model order. Both sinusoidal and square stimulation waveform inputs were shown to approach an approximate 10 % efficiency (for even orders of the Taylor expansion for sinusoidal inputs, and $K_n = 1$ for all expansion coefficients). It was also discussed there is a general need for the validation of the presented results for other stimulation waveform shapes, as the current literature on TIS rarely features stimulation waveforms other than sinusoidal ones. Additionally, determination of Taylor expansion scaling factors is required, to accurately match the experimental data.

Additionally, the performance of a proposed system architecture for power-efficient and spatially selective TIS-based vagus nerve stimulation was validated by comparison to conventional cascode current mirror output stage performance. It was shown that supply regulation, when directly referenced to electrode load voltage, yields substantial efficiency gains over constant supply variants. However, in combination with the regulated supply, the proposed output stage circuit design incurred a penalty such that the source-to-load transfer becomes highly dependent on the size of the source impedance. Regardless, the presented design was shown be able to perform the expected functions of a temporal-interference stimulator, and resulted in high load current accuracy, leaving small remnant offset voltage across the electrodes. Further discussion highlighted the importance of adding additional charge balancing circuitry, and some of the circuit design choices and assumptions made were critically analysed.

5.1 Contributions

This thesis presents the following original contributions to the field of temporal interference-based neurostimulator design:

- A physiologically accurate model for the representation of nonlinear neuron responses to temporally interfering electric field waveforms at kilohertz-range frequencies, validated by *ex-vivo* and *in-vivo* measurements of temporal interference stimulation from literature.
- An analysis and critical review of indirect feedback output stage compliance in context of energy-, and power-efficiency in neural stimulator circuits, and a proposed power supply regulation scheme that significantly increases power-efficiency as compared to stimulator circuits with constant supplies.
- A systematically designed and power-efficient vagus nerve stimulator output stage circuit, employing the presented supply regulation scheme, for spatially selective temporal interference-based vagus nerve stimulation.

5.2 Suggestions for future work

5.2.1 Suggestions related to the proposed electrophysiological model for TIS

Measurement of neural response to input waveforms other than sinusoidal waveforms

The model accuracy depends on the measured data already available in literature, which, in the relatively unexplored field of TIS-based neural stimulation, is mostly limited to the use of sinusoidal input waveforms. If the model would be generalized for more than just sinusoidal inputs, more data needs to be generated to validate results of different waveform shapes on the generated model output. A very common square waveform shape was discussed as an example in this work, but the presented conclusions hinge on the assumption that the model is generalizable to an extent that it also accurately represents other waveform shapes. Aside from output quantities and stimulation modes, this requires the complex design of experimental test setups for the measurement of biological tissue, which was not covered in the contents of this report.

Accurate determination of Taylor expansion coefficients

The Taylor expansion coefficients were assumed to be $K_n = 1$ for every order of the Taylor expansion, which is not a realistic assumption. To more accurately match the measurements in literature, the Taylor expansion coefficients of the posited general model in (3.11) need to be determined based on the input/output relationship of measured neural stimulation waveforms. This could be inferred from the neuron response by means of action potential measurement, but literature prefers the use of subthreshold responses to judge neural responses to TIS. As mentioned before, the mentioned coefficients directly represent the neuron's preferential treatment of certain frequency components for various Taylor expansion orders of the output waveform created by nonlinear frequency mixing operations in the neuron membrane. It is thus fairly important to determine these coefficients up to a relevant order for more meaningful comparison to power spectral densities in the following.

Transitioning into a spatially distributed model for the simulation of whole-nerve responses under influence of TIS

The presented model is essentially locked in an optimal position, at the focal point of interference. It was discussed that electric fields have a spatial component, which is very relevant to the topic of spatially selective neuromodulation. This property of the electric fields was largely put aside to focus on the effect of interference of the individual input waveforms in ideal situations. In literature it was found that the spatial distribution of the electric fields intermittently produced regions of modulated, unmodulated, or conduction blocking waveforms, which might arguably be a desired effect. However, the reported spatial dependence of the modulation depth, and its implications for the model output, have not been considered as of yet. An expansion into multiple spatial dimensions of the Taylor expansion is possible, but requires some fairly hefty mathematical operations that might best be handled by finite-element analysis methods of electric field distributions, or some other advanced methods of multi-dimensional nonlinear approximation.

Representation of nonlinear neuron responses to TIS in an equivalent lumped element electrical model

As an aside, related thesis work also attempted to provide a lumped element equivalent circuit model of nonlinear neuron responses to TIS. This equivalent circuit consisted of a single balanced frequency mixer. This model was largely ignored to focus on other aspects of the research, but in combination with the cable equations, and the related Hodgkin-Huxley conductance model, it may be able to provide a fairly relevant representation of the output waveforms as retrieved from the model output in Fig. 3.3.

5.2.2 Suggestions related to the proposed TIS stimulator system architecture

Determining diminishing returns with regard to spatial selectivity and amount of output electrodes

It was briefly mentioned that there is a trade-off between the amount of output electrodes for spatial selectivity and the size and complexity of the required output electrode selection logic to select every combination of output electrodes possible. Such an analysis might elucidate that a certain partitioning of the presented system is more or less beneficial than another, which should ideally provide an optimal solution in terms of circuit size and spatial selectivity.

Circuit design considerations

- **Addition of digital and power electronics circuitry:** The function of measurement circuitry, control logic, control of the external regulated power supply and determination of minimal overhead voltage are idealized, to focus on the analysis of analog circuitry used in the output stage. However, the implementation of these components will have profound effects on the output stage accuracy and power-efficiency. The system blocks in Fig. 2.9 have been addressed at surface level, and are left for future work that builds on the findings in this report.
- **Addition of charge balancing circuitry:** Throughout this report it became abundantly clear that neural stimulators build up a remnant offset voltage across the electrodes, due to (nonlinear) charge storage mechanisms in the electrode-tissue interface. Some successful approaches to the implementation of charge balancing have been suggested, where it was discussed that offset regulation techniques are best suited to the semi-continuous nature of TIS. Due in part to a lack of time, the addition of this charge balancing circuitry in the output stage design has been relegated to future research endeavours. Even so, the presented architecture does not hinder the addition of such a system on top of the proposed design.
- **Consider a paradigm shift to direct feedback output stages, regardless of added overhead:** The presented results also clearly illustrate the difficulty of designing viable indirect feedback output stages for neural stimulation, as even under ideal conditions with the addition of a nullor, the source-to-load transfer would be highly source or load dependent. If, in future work, it is shown that the introduced overhead can indeed be in the range of 1 V, the presented argumentation — that direct feedback adds additional overhead that needs to be minimized, but proper current sensing becomes difficult at small overhead voltages — falls flat. It is therefore highly likely that a direct negative feedback system will provide even better outcomes, regardless of current sensing devices in the output signal path.
- **Improvement of output stage design:** The points of discussion in Sec. 4.3.1 mention a large part of the shortcomings of the presented circuit design, which will need to be addressed in future research.

List of references

[1] B. Research, *Global number of pacemakers in 2016 and a forecast for 2023 (in million units)*, Accessed July, 2025, Jun. 2017. [Online]. Available: https://www.statista.com/statistics/800794/pacemakers-market-volume-in-units-worldwide/.

[2] P. Afra, B. Adamolekun, S. Aydemir, and G. D. R. Watson, "Evolution of the Vagus Nerve Stimulation (VNS) Therapy System Technology for Drug-Resistant Epilepsy," *Front. Med.Technol.*, vol. Volume 3 - 2021, 2021. DOI: 10.3389/fmedt.2021.696543.

[3] E. Ben-Menachem *et al.*, "Vagus nerve stimulation for treatment of partial seizures: 1. a controlled study of effect on seizures. First International Vagus Nerve Stimulation Study Group," *Epilepsia*, vol. 35, no. 3, pp. 616–26, 1994. DOI: 10.1111/j.1528-1157.1994.tb02482.x.

[4] T. R. C. H. Melbourne, *Vagus nerve stimulation*, Accessed July, 2025. [Online]. Available: https://www.rch.org.au/Vagus_nerve_stimulation.aspx.

[5] C. Xu *et al.*, "Long-term outcomes and prognosis factors of vagus nerve stimulation in patients with refractory epilepsy," *Acta Epileptol.*, vol. 4, no. 1, p. 38, 2022. DOI: 10.1186/s42494-022-00109-w. [Online]. Available: https://doi.org/10.1186/s42494-022-00109-w.

[6] D. H. Toffa, L. Touma, T. El Meskine, A. Bouthillier, and D. K. Nguyen, "Learnings from 30 years of reported efficacy and safety of vagus nerve stimulation (VNS) for epilepsy treatment: A critical review," *Seizure*, vol. 83, pp. 104–123, 2020. DOI: https://doi.org/10.1016/j.seizure.2020.09.027. [Online]. Available: https://www.sciencedirect.com/science/article/pii/S1059131120303095.

[7] E. N. Marieb and K. Hoehn, *Human Anatomy & Physiology, Global Edition*, 10th Global. Harlow, Essex, England: Pearson Education Limited, 2015, ISBN: 9781292096971.

[8] OpenStax, *OpenStax AnatPhys fig.12.2 - Overview of Nervous System - English labels*, at AnatomyTOOL.org by OpenStax, license: Creative Commons Attribution. Source: book 'Anatomy and Physiology'. [Online]. Available: https://openstax.org/details/books/anatomy-and-physiology.

[9] OpenStax, *OpenStax AnatPhys fig.13.21 - Nerve Structure - English labels*, at AnatomyTOOL.org by OpenStax and Regents of U-M Medical School, UMich MedSchool, license: Creative Commons Attribution. Source: book 'Anatomy and Physiology'. [Online]. Available: https://openstax.org/details/books/anatomy-and-physiology.

[10] H. Fischer, *Three Basic Types of Neuronal Arrangements*, Artwork by Holly Fischer, CC BY 3.0, via Wikimedia Commons. [Online]. Available: https://upload.wikimedia.org/wikipedia/commons/6/61/Three_Basic_Types_of_Neuronal_Arrangements.png.

[11] P. Barry and J. Lynch, "Ligand-gated channels," *IEEE Trans. Nanobiosci.*, vol. 4, no. 1, pp. 70–80, 2005. DOI: 10.1109/TNB.2004.842497.

[12] B. Alberts *et al.*, *Ion Channels and the Electrical Properties of Membranes*, Molecular Biology of the Cell, New York, 2002. [Online]. Available: https://www-ncbi-nlm-nih-gov.tudelft.idm.oclc.org/books/NBK26910/.

[13] P. Cesare, A. Moriondo, V. Vellani, and P. A. McNaughton, "Ion channels gated by heat," *Proc. Natl. Acad. Sci. U.S.A.*, vol. 96, no. 14, pp. 7658–63, 1999. DOI: 10.1073/pnas.96.14.7658.

[14] H. Terlau and W. Stühmer, "Structure and Function of Voltage-Gated Ion Channels," *Naturwissenschaften*, vol. 85, no. 9, pp. 437–444, 1998. DOI: 10.1007/s001140050527.

[15] J. Malmivuo and R. Plonsey, *Bioelectromagnetism: Principles and Applications of Bioelectric and Biomagnetic Fields*. Oxford University Press, Oct. 1995. DOI: 10.1093/acprof:oso/9780195058239.001.0001. [Online]. Available: https://doi.org/10.1093/acprof:oso/9780195058239.001.0001.

[16] H. Bostock, "The strength-duration relationship for excitation of myelinated nerve: Computed dependence on membrane parameters," *J. Physiol.*, vol. 341, no. 1, pp. 59–74, 1983. DOI: 10.1113/jphysiol.1983.sp014792.

[17] A. L. Hodgkin and A. F. Huxley, "A quantitative description of membrane current and its application to conduction and excitation in nerve," *J. Physiol.*, vol. 117, no. 4, pp. 500–44, Aug. 1952. DOI: 10.1113/jphysiol.1952.sp004764.

[18] R. E. McAllister, D. Noble, and R. W. Tsien, "Reconstruction of the electrical activity of cardiac Purkinje fibres," *J. Physiol.*, vol. 251, no. 1, pp. 1–59, 1975. DOI: 10.1113/jphysiol.1975.sp011080.

[19] F. J. Fry, H. W. Ades, and W. J. Fry, "Production of Reversible Changes in the Central Nervous System by Ultrasound," *Science*, vol. 127, no. 3289, pp. 83–84, 1958. DOI: 10.1126/science.127.3289.83.

[20] R. Beisteiner and A. M. Lozano, "Transcranial Ultrasound Innovations Ready for Broad Clinical Application," *Adv. Sci.*, vol. 7, no. 23, 2020. DOI: 10.1002/advs.202002026.

[21] M. E. Rice, "Ascorbate regulation and its neuroprotective role in the brain," *Trends Neurosci.*, vol. 23, no. 5, pp. 209–216, 2000. DOI: 10.1016/S0166-2236(99)01543-X.

[22] X. Xu, Y. Zuo, S. Chen, A. Hatami, and H. Gu, "Advancements in brain research: The in vivo/in vitro electrochemical detection of neurochemicals," *Biosensors*, vol. 14, no. 3, 2024, ISSN: 2079-6374. DOI: 10.3390/bios14030125.

[23] P. S. Kalanithi and J. M. Henderson, "Optogenetic neuromodulation," *Int. Rev. Neurobiol.*, vol. 107, pp. 185–205, 2012. DOI: 10.1016/b978-0-12-404706-8.00010-3.

[24] H. Shin *et al.*, "Transcranial optogenetic brain modulator for precise bimodal neuromodulation in multiple brain regions," *Nat. Commun.*, vol. 15, no. 1, 2024. DOI: 10.1038/s41467-024-54759-0.

[25] D. A. Robinson, "The electrical properties of metal microelectrodes," *Proc. IEEE*, vol. 56, no. 6, pp. 1065–1071, 1968. DOI: 10.1109/proc.1968.6458.

[26] W. Franks, I. Schenker, P. Schmutz, and A. Hierlemann, "Impedance characterization and modeling of electrodes for biomedical applications," *IEEE Trans. Biomed. Eng.*, vol. 52, no. 7, pp. 1295–1302, 2005. DOI: 10.1109/TBME.2005.847523.

[27] D. R. Merrill, "The Electrochemistry of Charge Injection at the Electrode/Tissue Interface," in *Implantable Neural Prostheses 2: Techniques and Engineering Approaches*, D. Zhou and E. Greenbaum, Eds. New York, NY: Springer New York, 2010, pp. 85–138. DOI: 10.1007/978-0-387-98120-8_4.

[28] Y. Liu, X. Zhou, J. Ma, Y. Ge, and X. Cao, "The diameters and number of nerve fibers in spinal nerve roots," *J. Spinal Cord Med.*, vol. 38, no. 4, pp. 532–537, 2014. DOI: 10.1179/1079026814z.000000000273.

[29] R. Ortiz, R. F. Westenberg, C. G. Langhammer, W. J. Knaus, N. C. Chen, and K. R. Eberlin, "Nerve Diameter in the Hand: A Cadaveric Study," *Plast. Reconstr. Surg. Glob. Open*, vol. 7, no. 3, e2155, 2019. DOI: 10.1097/gox.0000000000002155.

[30] W. M. Grill, "Modeling the effects of electric fields on nerve fibers: Influence of tissue electrical properties," *IEEE Trans. Biomed. Eng.*, vol. 46, no. 8, pp. 918–928, 1999. DOI: 10.1109/10.775401.

[31] M. D. Johnson *et al.*, "Neuromodulation for Brain Disorders: Challenges and Opportunities," *IEEE Trans. Biomed. Eng.*, vol. 60, no. 3, pp. 610–624, Mar. 2013. DOI: 10.1109/tbme.2013.2244890.

[32] J. de Kroon, M. IJzerman, J. Chae, G. Lankhorst, and G. Zilvold, "Relation between stimulation characteristics and clinical outcome in studies using electrical stimulation to improve motor control of the upper extremity in stroke," *J. Rehabil. Med.*, vol. 37, no. 2, pp. 65–74, Mar. 2005. DOI: 10.1080/16501970410024190.

[33] J. Lee, P. Werginz, T. Kameneva, M. Im, and S. I. Fried, "Membrane depolarization mediates both the inhibition of neural activity and cell-type-differences in response to high-frequency stimulation," *Commun. Biol.*, vol. 7, no. 1, p. 734, Jun. 2024. DOI: 10.1038/s42003-024-06359-3.

[34] C. Neudorfer *et al.*, "Kilohertz-frequency stimulation of the nervous system: A review of underlying mechanisms," *Brain Stimul.*, vol. 14, no. 3, pp. 513–530, Jun. 2021. DOI: 10.1016/j.brs.2021.03.008.

[35] X. F. Wei and W. M. Grill, "Impedance characteristics of deep brain stimulation electrodes in vitro and in vivo," *J. Neural Eng.*, vol. 6, no. 4, p. 046 008, 2009. DOI: 10.1088/1741-2560/6/4/046008.

[36] O. Tashani and M. Johnson, "Transcutaneous electrical nerve stimulation (tens). a possible aid for pain relief in developing countries?" *Libyan J. Med.*, vol. 4, no. 2, pp. 77–83, 2008. DOI: 10.4176/090119.

[37] P. Patel *et al.*, "Latest Advancements in Transcutaneous Electrical Nerve Stimulation (TENS) and Electronic Muscle Stimulation (EMS): Revisiting an Established Therapy with New Possibilities," *J. Pain Res.*, vol. Volume 18, pp. 137–153, 2025. DOI: 10.2147/jpr.S493162.

[38] K. M. Peters *et al.*, "Randomized Trial of Percutaneous Tibial Nerve Stimulation Versus Sham Efficacy in the Treatment of Overactive Bladder Syndrome: Results From the SUmiT Trial," *J. Urol.*, vol. 183, no. 4, pp. 1438–1443, 2010. DOI: 10.1016/j.juro.2009.12.036.

[39] C. L. Wells, "Chapter 43 - Cardiac pacemakers and defibrillators," in *A Comprehensive Guide to Geriatric Rehabilitation (Third Edition)*, T. L. Kauffman, R. Scott, J. O. Barr, and M. L. Moran, Eds., Third Edition, Oxford: Churchill Livingstone, 2014, pp. 298–303. DOI: https://doi.org/10.1016/B978-0-7020-4588-2.00043-7.

[40] P. Gutruf *et al.*, "Wireless, battery-free, fully implantable multimodal and multisite pacemakers for applications in small animal models," *Nat. Commun.*, vol. 10, no. 1, p. 5742, 2019. DOI: 10.1038/s41467-019-13637-w.

[41] L. Servier, *Cardiovascular system - Pacemaker – Smart-Servier*, CC BY-SA 3.0, via Wikimedia Commons. [Online]. Available: https://upload.wikimedia.org/wikipedia/commons/8/81/Cardiovascular_system_-_Pacemaker_--_Smart-Servier.png.

[42] Y. Yuan, L. Zheng, Z. Feng, and G. Yang, "Different effects of monophasic pulses and biphasic pulses applied by a bipolar stimulation electrode in the rat hippocampal CA1 region," *Biomed. Eng. Online*, vol. 20, no. 1, p. 25, 2021. DOI: 10.1186/s12938-021-00862-y.

[43] V. S. Mallela, V. Ilankumaran, and N. S. Rao, "Trends in cardiac pacemaker batteries," *Indian Pacing Electrophysiol. J.*, vol. 4, no. 4, pp. 201–12, 2004.

[44] M. Marquette, S. Budhdeo, V. Rajagopal, and M. Marinescu, "Cardiac device-associated lead infection: A diagnosis not to be missed," *Oxf. Med. Case Reports*, vol. 2015, no. 3, pp. 222–5, 2015. DOI: 10.1093/omcr/omv014.

[45] M. Döring, S. Richter, and G. Hindricks, "The Diagnosis and Treatment of Pacemaker-Associated Infection," *Dtsch. Arztebl. Int.*, vol. 115, no. 26, pp. 445–452, 2018. DOI: 10.3238/arztebl.2018.0445.

[46] F. Morady, "66 - Electrophysiologic Interventional Procedures and Surgery," in *Goldman's Cecil Medicine (Twenty Fourth Edition)*, L. Goldman and A. I. Schafer, Eds., Twenty Fourth Edition, Philadelphia: W.B. Saunders, 2012, pp. 369–373, ISBN: 978-1-4377-1604-7. DOI: https://doi.org/10.1016/B978-1-4377-1604-7.00066-X.

[47] G. L. Barbruni, P. M. Ros, D. Demarchi, S. Carrara, and D. Ghezzi, "Miniaturised Wireless Power Transfer Systems for Neurostimulation: A Review," *IEEE Trans. Biomed. Circuits Syst.*, vol. 14, no. 6, pp. 1160–1178, 2020. DOI: 10.1109/TBCAS.2020.3038599.

[48] C. Günter, J. Delbeke, and M. Ortiz-Catalan, "Safety of long-term electrical peripheral nerve stimulation: Review of the state of the art," *J. Neuroeng. Rehabil.*, vol. 16, no. 1, p. 13, 2019. DOI: 10.1186/s12984-018-0474-8.

[49] K. Sooksood, T. Stieglitz, and M. Ortmanns, "An experimental study on passive charge balancing," *Adv. in Radio Sci.*, vol. 7, pp. 197–200, 2009. DOI: 10.5194/ars-7-197-2009.

[50] K. Sooksood, T. Stieglitz, and M. Ortmanns, "An Active Approach for Charge Balancing in Functional Electrical Stimulation," *IEEE Trans. Biomed. Circuits Syst.*, vol. 4, no. 3, pp. 162–170, 2010. DOI: 10.1109/tbcas.2010.2040277.

[51] G. L. K. Moganti, V. N. Siva Praneeth, and S. R. K. Vanjari, "A Hbrid Bipolar Active Charge Balancing Technique with Adaptive Electrode Tissue Interface (ETI) Impedance Variations for Facial Paralysis Patients," *Sensors (Basel)*, vol. 22, no. 5, 2022. DOI: 10.3390/s22051756.

[52] J. M. Späth, K. K. Kouri, L. Holzapfel, R. Thewes, and V. Giagka, "Stand-Alone Broad Frequency Range Charge-Balancing System for Neural Stimulators," in *2023 IEEE Biomedical Circuits and Systems Conference (BioCAS)*, Toronto, ON, Canada, 2023, pp. 1–5. DOI: 10.1109/BioCAS58349.2023.10388758.

[53] M. Ortmanns, N. Unger, A. Rocke, M. Gehrke, and H. Tietdke, "A 0.1mm^2, Digitally Programmable Nerve Stimulation Pad Cell with High-Voltage Capability for a Retinal Implant," in *2006 IEEE International Solid State Circuits Conference - Digest of Technical Papers*, San Francisco, CA, USA, 2006, pp. 89–98. DOI: 10.1109/ISSCC.2006.1696037.

[54] W.-Y. Hsu and A. Schmid, "Compact, Energy-Efficient High-Frequency Switched Capacitor Neural Stimulator With Active Charge Balancing," *IEEE Trans. Biomed. Circuits Syst.*, vol. 11, no. 4, pp. 878–888, 2017. DOI: 10.1109/TBCAS.2017.2694144.

[55] A. Wongsarnpigoon, J. P. Woock, and W. M. Grill, "Efficiency Analysis of Waveform Shape for Electrical Excitation of Nerve Fibers," *IEEE Trans. Neural Syst. Rehabil. Eng.*, vol. 18, no. 3, pp. 319–328, 2010. DOI: 10.1109/tnsre.2010.2047610.

[56] T. J. Foutz and C. C. McIntyre, "Evaluation of novel stimulus waveforms for deep brain stimulation," *J. Neural Eng.*, vol. 7, no. 6, 2010. DOI: 10.1088/1741-2560/7/6/066008.

[57] M. Sahin and Y. Tie, "Non-rectangular waveforms for neural stimulation with practical electrodes," *J. Neural Eng.*, vol. 4, no. 3, pp. 227–233, 2007. DOI: 10.1088/1741-2560/4/3/008.

[58] A. Wongsarnpigoon and W. M. Grill, "Energy-efficient waveform shapes for neural stimulation revealed with a genetic algorithm," *J. Neural Eng.*, vol. 7, no. 4, p. 046 009, 2010. DOI: 10.1088/1741-2560/7/4/046009.

[59] F. Varkevisser, T. L. Costa, and W. A. Serdijn, "Energy efficiency of pulse shaping in electrical stimulation: The interdependence of biophysical effects and circuit design losses," *Biomed. Phys. Eng. Express*, vol. 8, no. 6, 2022. DOI: 10.1088/2057-1976/ac8c47.

[60] F. Varkevisser, T. L. Costa, and W. A. Serdijn, "Multichannel current-mode stimulator with channel-specific regulated power supply," in *2023 IEEE Biomedical Circuits and Systems Conference (BioCAS)*, Toronto, ON, Canada, 2023, pp. 1–5. DOI: 10.1109/BioCAS58349.2023.10388577.

[61] S. K. Arfin and R. Sarpeshkar, "An Energy-Efficient, Adiabatic Electrode Stimulator With Inductive Energy Recycling and Feedback Current Regulation," *IEEE Trans. Biomed. Circuits Syst.*, vol. 6, no. 1, pp. 1–14, 2012. DOI: 10.1109/tbcas.2011.2166072.

[62] K. Kolovou-Kouri, A. Rashidi, F. Varkevisser, W. A. Serdijn, and V. Giagka, "Energy Savings of Multi-Channel Neurostimulators with Non-Rectangular Current-Mode Stimuli Using Multiple Supply Rails," in *2022 44th Annual International Conference of the IEEE Engineering in Medicine & Biology Society (EMBC)*, Glasglow, Scotland, United Kingdom, 2022, pp. 3443–3446. DOI: 10.1109/EMBC48229.2022.9871145.

[63] E. Noorsal, K. Sooksood, H. Xu, R. Hornig, J. Becker, and M. Ortmanns, "A neural stimulator frontend with high-voltage compliance and programmable pulse shape for epiretinal implants," *IEEE J. Solid-State Circuits*, vol. 47, no. 1, pp. 244–256, 2012. DOI: 10.1109/jssc.2011.2164667.

[64] A. J. M. Montagne, *Structured Electronics Design: a conceptual approach to amplifier design*, 3rd ed. Delft, The Netherlands: TU Delft OPEN Publishing, Jul. 2023, ISBN: 9789463667128. DOI: 10.59490/t.2023.005.

[65] M. S. George *et al.*, "Vagus nerve stimulation: A new tool for brain research and therapy," *Biol. Psychiatry*, vol. 47, no. 4, pp. 287–295, Feb. 2000. DOI: 10.1016/s0006-3223(99)00308-x.

[66] A. Fitchett, S. Mastitskaya, and K. Aristovich, "Selective Neuromodulation of the Vagus Nerve," *Front. Neurosci.*, vol. 15, 2021. DOI: 10.3389/fnins.2021.685872.

[67] S. L. Thompson *et al.*, "A Review of Parameter Settings for Invasive and Non-invasive Vagus Nerve Stimulation (VNS) Applied in Neurological and Psychiatric Disorders," *Front. Neurosci.*, vol. 15, Jul. 2021. DOI: 10.3389/fnins.2021.709436.

[68] R. Câmara and C. J. Griessenauer, "Chapter 27 - Anatomy of the Vagus Nerve," in *Nerves and Nerve Injuries*. Academic Press, 2015, pp. 385–397, ISBN: 9780124103900. DOI: 10.1016/b978-0-12-410390-0.00028-7.

[69] D. T. T. Plachta, M. Gierthmuehlen, O. Cota, F. Boeser, and T. Stieglitz, "BaroLoop: Using a multichannel cuff electrode and selective stimulation to reduce blood pressure," in *Annu. Int. Conf. IEEE Eng. Med. Biol. Soc.*, Osaka, Japan, 2013, pp. 755–758. DOI: 10.1109/embc.2013.6609610.

[70] E. Ben-Menachem, "Vagus Nerve Stimulation, Side Effects, and Long-Term Safety," *J. Clin. Neurophysiol.*, vol. 18, no. 5, pp. 415–418, Sep. 2001. DOI: 10.1097/00004691-200109000-00005.

[71] D. T. T. Plachta *et al.*, "Blood pressure control with selective vagal nerve stimulation and minimal side effects," *J. Neural Eng.*, vol. 11, no. 3, May 2014. DOI: 10.1088/1741-2560/11/3/036011.

[72] P. Pečlin *et al.*, "Selective stimulation of the vagus nerve in a man," in *4th European Conference of the International Federation for Medical and Biological Engineering*, Antwerp, Belgium, 2009, pp. 1628–1631.

[73] N. Thompson, S. Mastitskaya, and D. Holder, "Avoiding off-target effects in electrical stimulation of the cervical vagus nerve: Neuroanatomical tracing techniques to study fascicular anatomy of the vagus nerve," *J. Neurosci. Methods*, vol. 325, Sep. 2019. DOI: 10.1016/j.jneumeth.2019.108325.

[74] K. Aristovich *et al.*, "Model-based geometrical optimisation and in vivo validation of a spatially selective multielectrode cuff array for vagus nerve neuromodulation," *J. Neurosci. Methods*, vol. 352, Mar. 2021. DOI: 10.1016/j.jneumeth.2021.109079.

[75] N. Grossman *et al.*, "Noninvasive Deep Brain Stimulation via Temporally Interfering Electric Fields," *Cell*, vol. 169, no. 6, 1029–1041.E16, Jun. 2017. DOI: 10.1016/j.cell.2017.05.024.

[76] J. Xu *et al.*, "Fascicle-Selective Bidirectional Peripheral Nerve Interface IC with 173dB FOM Noise-Shaping SAR ADCs and 1.38pJ/b Frequency-Multiplying Current-Ripple Radio Transmitter," in *2023 IEEE International Solid-State Circuits Conference (ISSCC)*, San Francisco, CA, USA, 2023, pp. 31–33. DOI: 10.1109/ISSCC42615.2023.10067626.

[77] A. Opančar, D. S. Rose, P. Ondráčková, J. Trajlinek, V. Đerek, and E. D. Głowacki, "There is no Biophysical Distinction between Temporal Interference Stimulation and Direct kHz Stimulation for Actuation of Peripheral Nerves," To be published, Mar. 2025. DOI: 10.1101/2024.09.06.611584. [Online]. Available: https://www.biorxiv.org/content/10.1101/2024.09.06.611584v2 (visited on 06/29/2025).

[78] R. B. Budde, M. T. Williams, and P. P. Irazoqui, "Temporal interference current stimulation in peripheral nerves is not driven by envelope extraction," *J. Neural Eng.*, vol. 20, no. 2, Apr. 2023. DOI: 10.1088/1741-2552/acc6f1.

[79] R. R. Llinás, "The intrinsic electrophysiological properties of mammalian neurons: Insights into central nervous system function," *Science*, vol. 242, no. 4886, pp. 1654–64, Dec. 1988. DOI: 10.1126/science.3059497.

[80] A. B. Neiman and D. F. Russell, "Two Distinct Types of Noisy Oscillators in Electroreceptors of Paddlefish," *J. Neurophysiol.*, vol. 92, no. 1, pp. 492–509, Jul. 2004. DOI: 10.1152/jn.00742.2003.

[81] K. F. Ahrens, H. Levine, H. Suhl, and D. Kleinfeld, "Spectral mixing of rhythmic neuronal signals in sensory cortex," *Proc. Natl. Acad. Sci. U.S.A.*, vol. 99, no. 23, pp. 15 176–15 181, Nov. 2002. DOI: 10.1073/pnas.222547199.

[82] D. Haufler and D. Paré, "Detection of Multiway Gamma Coordination Reveals How Frequency Mixing Shapes Neural Dynamics," *Neuron*, vol. 101, no. 4, 603–614.e6, Feb. 2019. DOI: 10.1016/j.neuron.2018.12.028.

[83] C. E. Luff *et al.*, "The neuron mixer and its impact on human brain dynamics," *Cell Rep.*, vol. 43, no. 6, Jun. 2024. DOI: 10.1016/j.celrep.2024.114274.

[84] H. Xin *et al.*, "A 10V Compliant 16-Channel Stimulator ASIC with sub-10nA Mismatch and Simultaneous ETI Sensing for Selective Vagus Nerve Stimulation," in *2024 IEEE Custom Integrated Circuits Conference (CICC)*, Denver, CO, USA, 2024, pp. 1–2. DOI: 10.1109/CICC60959.2024.10528986.

[85] S. R. Khan, S. K. Pavuluri, G. Cummins, and M. P. Y. Desmulliez, "Wireless Power Transfer Techniques for Implantable Medical Devices: A Review," *Sensors (Basel)*, vol. 20, no. 12, 2020. DOI: 10.3390/s20123487.

[86] B. L. Turner *et al.*, "Ultrasound-Powered Implants: A Critical Review of Piezoelectric Material Selection and Applications," *Adv. Healthc. Mater.*, vol. 10, no. 17, 2021. DOI: 10.1002/adhm.202100986.

[87] H. Rivandi, I. Ghosh, and T. L. Costa, "A High-Frequency Beamforming Channel for Ultrasound Stimulation and Ultrasonic Powering," in *2022 IEEE Biomedical Circuits and Systems Conference (BioCAS)*, Taipei, Taiwan, 2022, pp. 40–44. DOI: 10.1109/BioCAS54905.2022.9948550.

[88] A. Williamson *et al.*, "Enhanced temporal interference stimulation: Pulsed and multipolar techniques for improved deep brain modulation," *Brain Stimul.*, vol. 18, no. 1, pp. 220–221, 2025. DOI: 10.1016/j.brs.2024.12.022.

[89] C. E. Luff, P. Dzialecka, E. Acerbo, A. Williamson, and N. Grossman, "Pulse-width modulated temporal interference (PWM-TI) brain stimulation," *Brain Stimul.*, vol. 17, no. 1, pp. 92–103, 2024. DOI: 10.1016/j.brs.2023.12.010.

Nomenclature

Acronyms

AC	Alternating current
ADC	Analog-to-digital converter
AP	Action potential
ASIC	Application-specific integrated circuit
ATP	Adenosine triphosphate
BW	Bandwidth
CG	Common-gate
ChMS	Charge-mode stimulation
CMOS	Complementary metal-oxide semiconductor
CMS	Current-mode stimulation
CNS	Central nervous system
COPD	Chronic obstructive pulmonary disease
CPE	Constant phase element
CS	Common-source
DAC	Digital-to-analog converter
DBS	Deep brain stimulation
DC	Direct current
EMF	Electromotive force
ETI	Electrode-tissue interface or electrode-tissue interface impedance
FFT	Fast Fourier transform
FOM	Figure of merit
GHK	Goldmann-Hodgkin-Katz
HV	High-voltage
I-DAC	Current-steering digital-to-analog converter
IPD	Inter-pulse delay
LPF	Low-pass filter
LV	Low-voltage
MOSFET	Metal-oxide-semiconductor field-effect transistor

NMOS	N-channel metal-oxide-semiconductor	
PMOS	P-channel metal-oxide-semiconductor	
PNS	Peripheral nervous system	
PSD	Power spectral density	
PTNS	Percutaneous tibial nerve stimulation	
PW	Pulse width	
PWM	Pulse-width modulated	
spTIS	Single-pulsed temporal interference stimulation	
T-1	Transmission-1	
TENS	Transcutaneous electrical nerve stimulation	
TI	Temporal interference	
TIS	Temporal interference stimulation	
TSMC	Taiwan Semiconductor Manufacturing Company	
VCCS	Voltage-controlled current source	
VCVS	Voltage-controlled voltage source	
VMS	Voltage-mode stimulation	
VNS	Vagus nerve stimulation	

Greek Symbols

Λ	Length constant	m
Ψ	Taylor expansion approximation output waveform	V
ψ	Fourier transform of the Taylor approximation output waveform	V
α	Multiplicity	–
δ	Current gain accuracy	–
λ	Wavelength	m
ω	Angular frequency	rad/s
π	Ratio of a circle's circumference to its diameter	–
τ	Time constant	s/rad
ξ	Amount of valence electrons in the outer shell of a specific ionic species	–
φ	Constant phase element exponent	–
$\widetilde{\Phi}$	Superposition output waveform	V

Roman Symbols

e	Euler's number	
F	Faraday constant	C/mol
j	Imaginary number	
k	Taylor expansion order	
M#	Transistor number #	

p	Integer number of input waveforms	
R	Gas constant	$\mathrm{J/(mol \cdot K)}$
s	Complex frequency variable of the Laplace transform	rad/s
T	Absolute temperature	K
t	Time	s
y	Lossless, continuous harmonic, one-dimensional electric field wave function	V/m
Z	Electrical impedance (complex number)	Ω
x	Position in space	m

Subscripts

ϵ_i	Current error	A
ϵ_dyn	Power error by absorption of the dynamic supply	W
$\epsilon_\mathrm{i,avg}$	Average current error	A
$\epsilon_\mathrm{i,pk}$	Peak current error	A
$\epsilon_\mathrm{overhead}$	Power error by absorption of the overhead	W
η_dyn	Dynamic supply output stage efficiency	–
η_pw	Power-providing supply output stage efficiency	–
η_sin	Relative stimulation efficiency of a sinusoidal waveform shape	–
η_sqr	Relative stimulation efficiency of a square waveform shape	–
η_stim	Power-efficiency of neural stimulation	–
η_tot	Total output stage efficiency	–
ν_i	Intracellular potential	V
ν_o	Extracellular potential	V
ω_1	Electric field angular frequency for input waveform 1	rad/s
ω_2	Electric field angular frequency for input waveform 2	rad/s
ω_dl	Angular corner frequency of double-layer impedance	rad/s
ϕ_ref	Electric field reference phase	rad
τ_m	Membrane time constant	s/rad
θ_1	Frequency-defining control signal for channel 1	–
θ_2	Frequency-defining control signal for channel 2	–
$\widetilde{y}_1$	Lossless, continuous harmonic, one-dimensional electric field wave function at the quiescent operating point of input 1	V
$\widetilde{y}_2$	Lossless, continuous harmonic, one-dimensional electric field wave function at the quiescent operating point of input 2	V
$\widetilde{y}_\mathrm{p}$	Lossless, continuous harmonic, one-dimensional electric field wave function at the quiescent operating point of an integer number of input(s) p	V
A_i	Current gain factor	–
A_t	Total active area of output stage transistors	$\mathrm{m^2}$

A_v	Voltage gain factor	–
A_y	Transadmittance gain factor	–
A_z	Transimpedance gain factor	–
BW_{VNS}	Physiologically relevant bandwidth of vagus nerve stimulation methods	Hz
c_m	Specific membrane capacitance	F/m
c_{db}	Complementary metal-oxide semiconductor small-signal drain-bulk capacitance	F
$C_{dl,high}$	High double-layer capacitance value	F
$C_{dl,low}$	Low double-layer capacitance value	F
C_{dl}	Double-layer capacitance	F
c_{gd}	Complementary metal-oxide semiconductor small-signal gate-drain capacitance	F
c_{gs}	Complementary metal-oxide semiconductor small-signal gate-source capacitance	F
C_{out}	Output capacitance	F
$E_{0–7}$	Electrodes 0 to 7	–
f_1	Electric field frequency for input waveform 1	Hz
f_2	Electric field frequency for input waveform 2	Hz
f_c	Corner frequency	Hz
g_K	Specific potassium conductance	S/m^2
g_L	Specific leakage conductance	S/m^2
G_m	Total equivalent transconductance	S
g_m	Complementary metal-oxide semiconductor small-signal transconductance	S
g_{Na}	Specific sodium conductance	S/m^2
i_m	Specific membrane current	A/m^2
$I_{\ell,max}$	Maximum load current	A
I_ℓ	Load current	A
I_{bias}	Bias current	A
i_{c_m}	Specific membrane capacitance current	A/m^2
I_D	Drain current	A
I_{ext}	Specific external axial membrane current	A/m
I_G	Gate current	A
I_{int}	Specific internal axial membrane current	A/m
I_i	Two-port input current	A
i_K	Specific potassium membrane current	A/m^2
i_L	Specific leakage membrane current	A/m^2
i_{Na}	Specific sodium membrane current	A/m^2
I_o	Two-port output current	A
i_{r_m}	Specific membrane resistance current	A/m^2

I_{rh}	Rheobase current	A
$I_{s,min}$	Minimum required stimulation current	A
I_s	Source current	A
K_n	Taylor expansion coefficent of order n	V
P_K	Coefficient of permeability of a potassium ion	–
P_ℓ	Power absorbed by the load	W
P_{Cl}	Coefficient of permeability of a chlorine ion	–
P_{ETI}	Power absorbed by the electrode-tissue interface impedance	W
P_{Na}	Coefficient of permeability of a sodium ion	–
P_{reg}	Maximum available power of the regulated supply	W
P_{sup}	Maximum available power of the supply	W
P_s	Power absorbed by the source (branch)	W
P_{tis}	Power absorbed by nerve tissue	W
$P_{tot,avg}$	Average total power dissipated	W
$P_{tot,pk}$	Peak total power dissipated	W
P_{tot}	Total dissipated power	W
Q_{dl}	Debye double-layer capacitance	$F/(m^2 \cdot s)$
r_m	Specific membrane resistance	$\Omega \cdot m$
R_{ct}	Charge transfer resistance	Ω
r_{ext}	Specific external axial membrane current	Ω/m
R_F	Faradaic resistance	Ω
r_{int}	Specific internal axial membrane resistance	Ω/m
$R_{on,max}$	Maximum complementary metal-oxide semiconductor on-resistance	Ω
R_{on}	Complementary metal-oxide semiconductor on-resistance	Ω
R_o	Total equivalent output resistance	Ω
r_o	Complementary metal-oxide semiconductor small-signal output resistance	Ω
R_s	Source resistance	Ω
$R_{tis1–6}$	Tissue resistances 1 to 6	Ω
R_{tis}	Nerve tissue resistance	Ω
t_d	Delay time	s
t_{IPD}	Inter-pulse delay time	s
t_{on}	Stimultion on-time	s
t_{pulse}	Pulse time	s
V_d	Deviation from the resting potential	V
V_K	Nernst potential of potassium ions	V
V_m	Membrane potential	V

V_r	Resting membrane potential	V
$V_{\ell,max}$	Maximum load voltage	V
V_ℓ	Load voltage	V
V_{con}	Controller output voltage	V
V_{DS}	Drain-source voltage	V
V_{dyn}	Dynamic power supply voltage	V
V_{ETI}	Voltage across electrode-tissue interface	V
V_{GS}	Gate-source voltage	V
V_i	Two-port input voltage	V
$V_{overhead,min}$	Minimum overhead voltage	V
$V_{overhead}$	Overhead voltage	V
V_o	Two-port output voltage	V
V_{pw}	Power-providing supply voltage	V
$V_{reg,max}$	Maximum regulated supply voltage	V
V_{reg}	Regulated supply voltage	V
V_{sup}	Supply voltage	V
V_s	Source voltage	V
Z_s	Source impedance (complex)	Ω
Z_W	Warburg impedance (complex)	Ω
Z_ℓ	Load impedance (complex)	Ω
Z_{CPE}	Constant phase element impedance (complex)	Ω
Z_{ETI}	Electrode-tissue interface impedance (complex)	Ω
Z_i	Amplifier input impedance (complex)	Ω
Z_o	Amplifier output impedance (complex)	Ω
$Z_{tis1–6}$	Tissue impedances 1 to 6 (complex)	Ω
y_1	Lossless, continuous harmonic, one-dimensional electric field wave function of input 1	V/m
y_2	Lossless, continuous harmonic, one-dimensional electric field wave function of input 2	V/m

Other Symbols

$[Cl]_i$	Concentration of chlorine ions in the intracellular medium	mol/L
$[Cl]_o$	Concentration of chlorine ions in the extracellular medium	mol/L
$[K]_i$	Concentration of potassium ions in the intracellular medium	mol/L
$[K]_o$	Concentration of potassium ions in the extracellular medium	mol/L
$[Na]_i$	Concentration of sodium ions in the intracellular medium	mol/L
$[Na]_o$	Concentration of sodium ions in the extracellular medium	mol/L
$\Delta\omega$	Angular difference frequency	rad/s
Δf	Difference frequency	Hz

ΔV	Remnant offset voltage across electrodes	V
$\Sigma\omega$	Angular sum frequency	rad/s
Σf	Sum frequency	Hz
Cl^-	Chlorine ion	
K^+	Potassium ion	
Na^+	Sodium ion	

Appendix A

PSD measurement data overlaid on top of model outputs

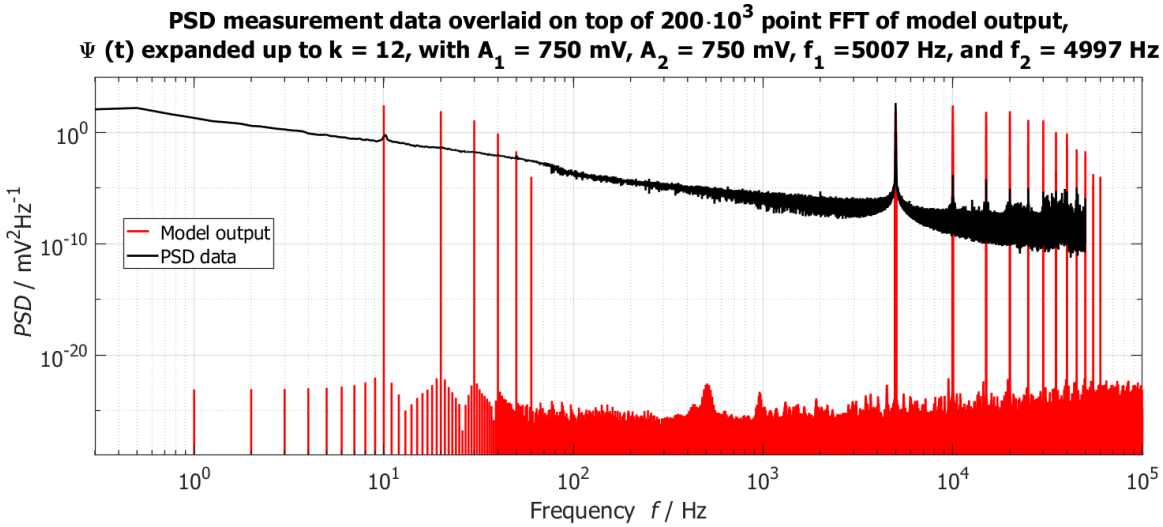

(a) Model output for $f_1 = 5007\,\text{Hz}$ and $f_2 = 4997\,\text{Hz}$.

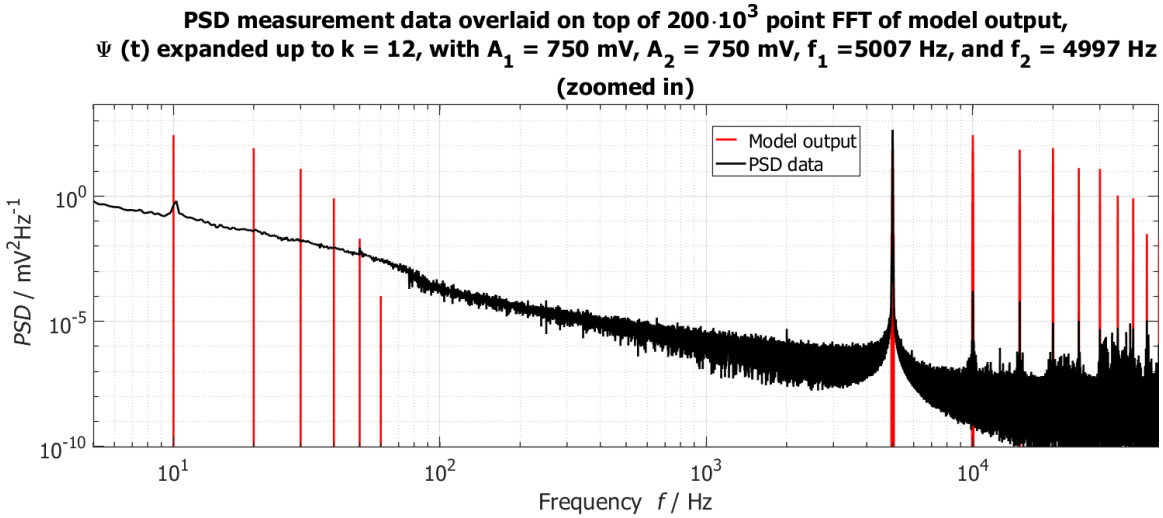

(b) Model output for $f_1 = 5007\,\text{Hz}$ and $f_2 = 4997\,\text{Hz}$ zoomed in.

Figure A.1: Model PSD output with the output waveform expanded up to the 12th order for $f_1 = 5007\,\text{Hz}$ and $f_2 = 4997\,\text{Hz}$, overlaid on top of measured power spectral density data with equal input frequencies.

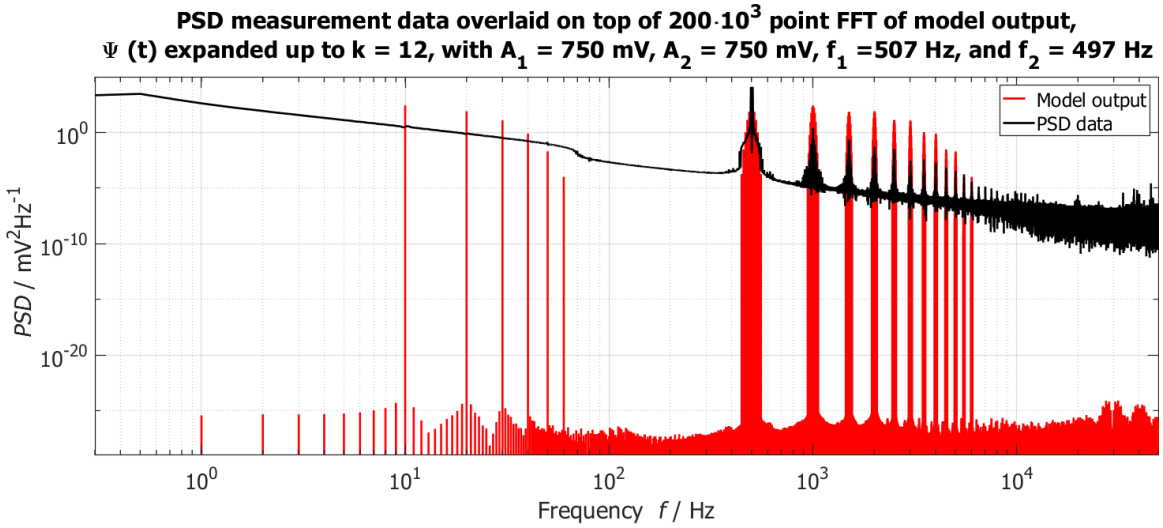

(a) Model output for $f_1 = 507\,\text{Hz}$ and $f_2 = 497\,\text{Hz}$.

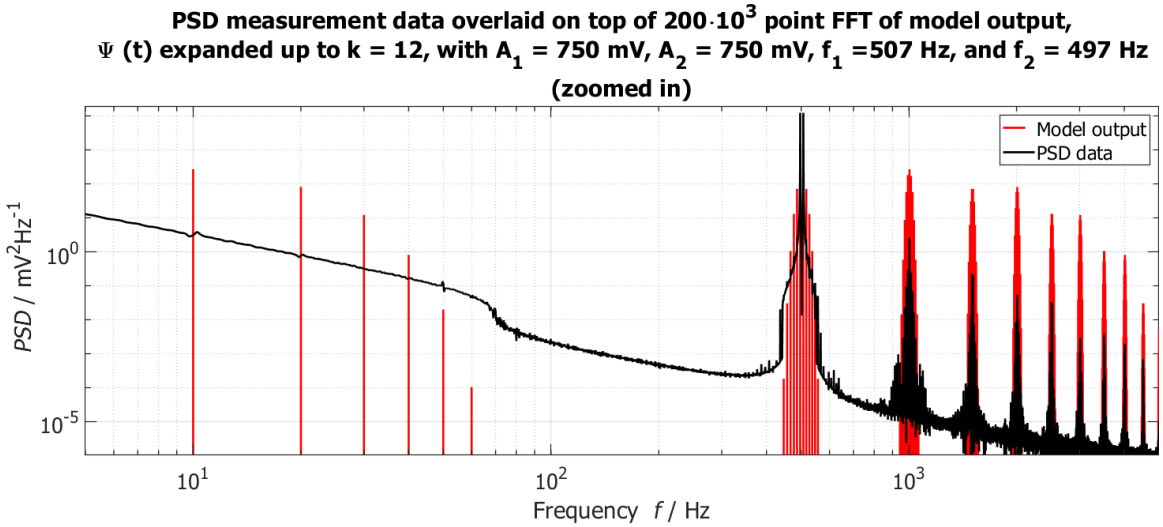

(b) Model output for $f_1 = 507\,\text{Hz}$ and $f_2 = 497\,\text{Hz}$ zoomed in.

Figure A.2: Model PSD output with the output waveform expanded up to the 12th order for $f_1 = 507\,\text{Hz}$ and $f_2 = 497\,\text{Hz}$, overlaid on top of measured power spectral density data with equal input frequencies.

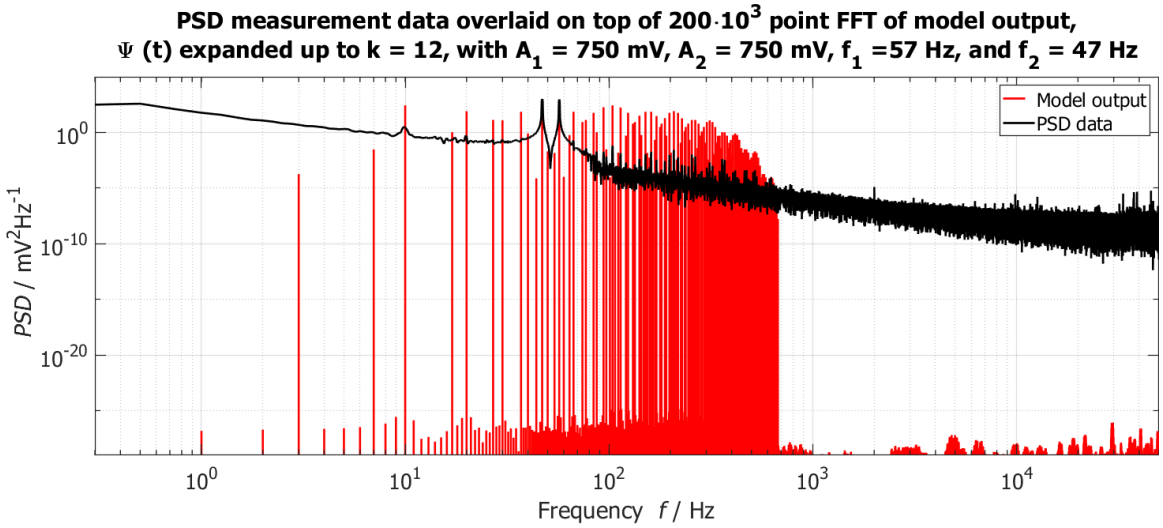

(a) Model output for $f_1 = 57\,\text{Hz}$ and $f_2 = 47\,\text{Hz}$.

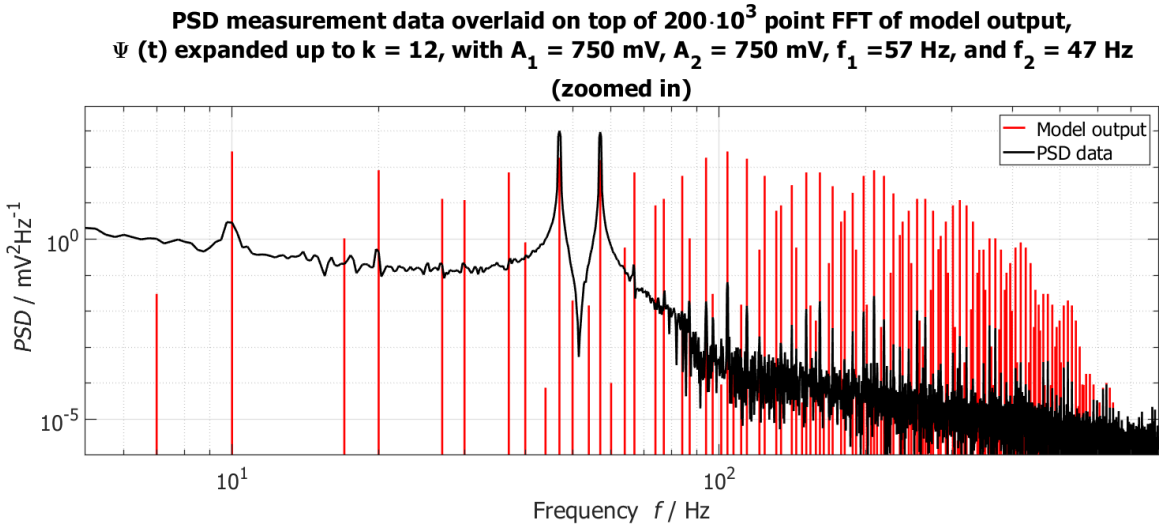

(b) Model output for $f_1 = 57\,\text{Hz}$ and $f_2 = 47\,\text{Hz}$ zoomed in.

Figure A.3: Model PSD output with the output waveform expanded up to the 12th order for $f_1 = 57\,\text{Hz}$ and $f_2 = 47\,\text{Hz}$, overlaid on top of measured power spectral density data with equal input frequencies.

Appendix B

Measured data and data processing of output stage simulations

The output stage simulation data comprises a large data set of measurements and derived quantities, which are exported from Cadence as CSV files. These files are then processed in MATLAB ver. R2024b to produce the plots shown in this report. All data are available upon request from the author, should a reader find it necessary.

Measured and calculated quantities for the transient tests

The measured and calculated quantities of the transient tests regarding the power and load current accuracy, are shown in table B.1.

Quantity	**Expression**	**Quantity**	**Expression**
Regulated supply output voltage	V_{reg}	Total power	$P_{tot} = V_{reg}I_{tot}$
Source voltage	V_s	Current error	$\epsilon_i = I_\ell - 100 \cdot I_s$
Load voltage	V_ℓ	Average ETI power	$P_{ETI,avg}$
ETI voltage	V_{ETI}	Average total power	$P_{tot,avg}$
Source current	I_s	Average current error	$\epsilon_{i,avg}$
Load current	I_ℓ	Peak ETI power	$P_{ETI,pk}$
Total current	$I_{tot} = I_{V_{reg}}$	Peak total power	$P_{tot,pk}$
ETI power	$P_{ETI} = V_{ETI}I_\ell$	Peak current error	$\epsilon_{i,pk}$

Table B.1: All measured and calculated quantities in the transient response test.

Load voltage waveforms for the determination of remnant offset voltage across electrodes

The measured output current and voltage across the electrodes in various phases of a conventional biphasic stimulation pulse are shown in Fig. B.1.

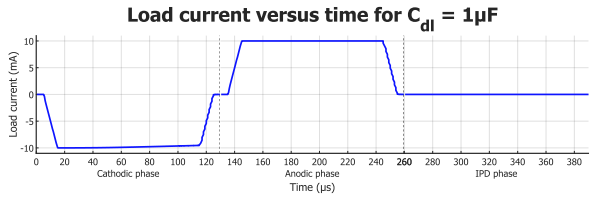

(a) Load current, $C_{dl} = 1\,\mu F$.

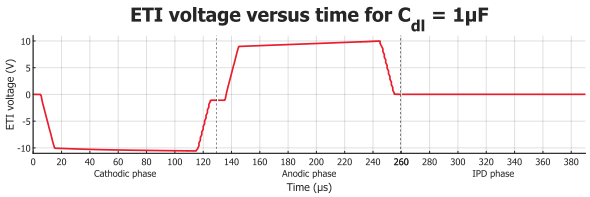

(b) ETI voltage, $C_{dl} = 1\,\mu F$.

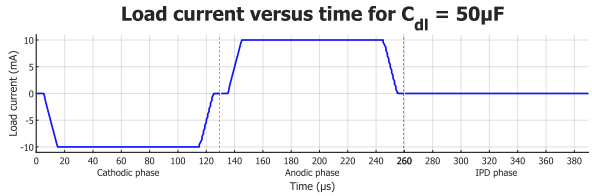

(c) Load current, $C_{dl} = 50\,\mu F$.

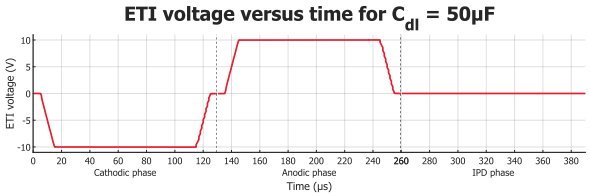

(d) ETI voltage, $C_{dl} = 50\,\mu F$.

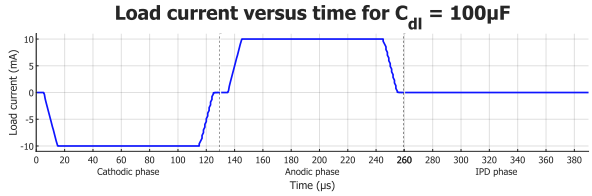

(e) Load current, $C_{dl} = 100\,\mu F$.

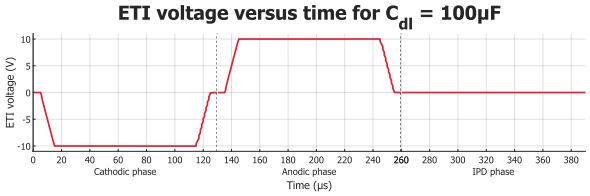

(f) ETI voltage, $C_{dl} = 100\,\mu F$.

Figure B.1: Waveforms of output quantities during varying phases of a stimulation pulse are shown. The used load impedance model features different values of the double-layer capacitance, to measure the dependence of remnant offset voltage on the charge storage capacity of the electrodes under influence of TIS.